

**NUMERICAL EVALUATION OF
CONCRETE MEMBERS USING
ULTRA HIGH PERFORMANCE
STRAIN HARDENING
CEMENTITIOUS COMPOSITES**

ZHANG Yongxing

NUMERICAL EVALUATION OF CONCRETE MEMBERS USING ULTRA HIGH PERFORMANCE STRAIN HARDENING CEMENTITIOUS COMPOSITES

By
ZHANG Yongxing

A Dissertation Submitted to Nagoya University
In Partial Fulfillment of the Requirements for
The Degree of Doctor of Engineering

Department of Civil Engineering
Graduate School of Engineering, Nagoya University
Nagoya, JAPAN

September, 2012

ACKNOWLEDGEMENTS

Foremost, I would like to express my deepest appreciation and gratitude to Prof. Hikaru NAKAMURA, my principal advisor, for his inestimable guidance, continuous support, patience and encouragement throughout my doctoral study in Nagoya University. He has also given me too much concern in my life and inspiration in science research. Surely, without his supports, this dissertation has never been completed. I would like to give my thanks to Assist. Prof. Naoshi UEDA who has always given me supporting in studying LECOM program. He has also given me inspiration in programming. Moreover, I am grateful to Assoc. Prof. Minoru Kunieda, who has given me invaluable comments, advices and discussion of my study on UHP-SHCC material. I also wish to express my sincere thanks to the other examination committee members. Also, I want to thank Mr. NAKASHIMA, who supported me in experiment with enthusiastic and patience.

I want to thank our families in China for their supports, understanding and encouragements to me during the time I stay in Japan. I am also grateful to the helps from the Japanese and Chinese friends in Japan during our stay here.

The author of this dissertation gratefully acknowledges that, the China Scholarship Council (CSC) provided me scholarship to pursue a doctoral degree in the field of Civil Engineering in Nagoya University. I also would like to thank my seniors, colleagues and friends in my laboratory as well as administrative staff and technicians of Nagoya University.

Last but not least, behind the accomplishment, I would like to express my deep thanks to my parents, for their love, trust, endless support, and hope on me during my studies in Japan. I want to extend my hearty appreciation to my dear wife for her endless love, patience, continuous encouragement and supports on me.

ABSTRACT

Ultra High Performance Strain Hardening Cementitious Composites (UHP-SHCC) is a newly developed construction material, has large advantages on large strain capacity as well as high compressive and tensile strength, which is useful for strengthening or repair concrete members. However, engineer tends to adopt traditional material for construction. One important obstacle is due to lacking numerical evaluation method. Therefore, analytical evaluation method is required for UHP-SHCC material in practical application. In this study, mechanical behavior of UHP-SHCC material is evaluated in material level and structural level.

UHP-SHCC material has large strain capacity and high tensile strength in uniaxial tensile behavior. However, the ductility is reduced when it is used for strengthening. This behavior is evaluated by zero-span tensile test. Moreover, a tri-linear curve model considering fracture energy is proposed to evaluate uniaxial tensile behavior of UHP-SHCC in material level. Then the zero-span tensile test is evaluated numerically using this proposed model with small mesh size.

UHP-SHCC is also a construction material, which can be used for structure. For construction material used for structure, shear behavior is very important. Therefore, shear behavior of UHP-SHCC members is clarified by experimental investigation. In the experiment, multiple fine cracks in middle span propagate along diagonal shear direction and play dominant role gradually, and all the specimens are failed in diagonal shear failure, which shows special fracture behavior. In order to understand the fracture behavior of UHP-SHCC member in shear failure clearly, the fracture surface of the UHP-SHCC member is investigated using laser displacement meter. Thereafter, numerical evaluation is conducted by the FEM analytical code based on concept of using lattice system about main lattice system, reinforcement lattice system and shear lattice system.

Especially, a shear stress transfer model is proposed to evaluate the shear behavior of UHP-SHCC members, considering roughness of crack surface depending on asperity height and shape of crack surface (θ), crack width depending on crack distribution, and fiber bridging contribution. This model is confirmed applicably for numerical evaluation of UHP-SHCC members in shear failure.

UHP-SHCC has obvious advantages for strengthening RC members, due to large strain capacity as well as high tensile and compressive strength. However, zero-span tensile behavior occurs when it is used for strengthening concrete members. In order to understand fracture process of RC member strengthened by UHP-SHCC, flexural

behavior of RC beam strengthened by UHP-SHCC is clarified by experimental investigation. Especially, the cracking opening performance of UHP-SHCC layer is investigated deeply. Thereafter, a new type of zero-span tensile model is proposed for UHP-SHCC used as a repair material for concrete substrate member with existing crack. This zero-span tensile model adopts a fictitious material of the same Young's modulus with concrete, and elastic stress-strain relationship without cracking is adopted to form artificial crack.

The numerical behavior of RC member strengthened by UHP-SHCC using this zero-span tensile model is investigated, such as load-displacement relationship and crack propagation behavior, which has a good agreement with experiment result, due to the proposed model considering the average behavior of multiple-fine cracks adjacent to existing crack in RC substrate beam. This model is confirmed applicably for numerical evaluation of UHP-SHCC used as a repair material for concrete substrate member with existing crack.

Using these proposed models, the strengthening effect of RC column strengthened by UHP-SHCC is evaluated numerically and reasonably.

Table of Content

Acknowledge

Abstract

Table of Content

List of Tables

List of Figures

Reference

1. Introduction	1
1.1 General Background	1
1.2 Purpose of This Study	3
1.3 Study Objective and Research Framework	4
1.4 Overview of the Thesis Content	5
2. Modeling of tensile behavior of UHP-SHCC material	7
2.1 Introduction	7
2.2 Tensile behavior of UHP-SHCC material	7
2.3 Modeling of tensile behavior of UHP-SHCC materials	12
2.4. Conclusion	18
3. Experimental investigation on shear behavior of UHP-SHCC beams	20
3.1. Introduction	20
3.2 Experimental Programs	20
3.3. Experimental result of UHP-SHCC beam in shear failure	23
3.4. Investigation on shape of fracture surface of UHP-SHCC beam failed in shear	30
3.5. Summary and conclusions	35
4. Analytical evaluation of shear failure of UHP-SHCC beams	37
4.1. Introduction	37
4.2. Analytical Method	38
4.3 Analytical model	44
4.4 Analytical simulation of Shear failure behavior of UHP-SHCC beam by shear transfer model for high strength concrete	45
4.5 Development of shear stress transfer model of UHP-SHCC	46
4.6 Conclusion	53

5. Experimental investigation on flexural behaviour of RC beam strengthened by UHP-SHCC	55
5.1. Introduction	55
5.2 Experimental Procedure	55
5.3. Experimental results of RC beams strengthened by UHP-SHCC	60
5.4 Conclusion	66
6. Numerical evaluation on flexural behavior of RC beams strengthened by UHP-SHCC	68
6.1 Introduction	68
6.2. Numerical simulation of tested beams strengthened by UHP-SHCC using uniaxial tensile model	68
6.3. Propose of zero-span tensile model	72
6.4. Numerical evaluation on flexural behavior of RC beam strengthened by UHP-SHCC using the proposed zero-span tensile model	79
6.5. Conclusion	83
7. Numerical evaluation on strengthening effect of RC column with UHP-SHCC material subjected to cyclic load	85
7.1 Introduction	85
7.2 Geometry for RC column strengthened by other materials	85
7.3 Application for repairing damaged RC column with UHP-SHCC	94
7.4. Conclusion	97
8. Conclusions	99

List of Tables

Table number and title	Page
Table 2.1. Mixture proportion of UHP-SHCC	7
Table 2.2. Stress and strain values in tri-linear model	16
Table 3.1. Details of specimens	21
Table 3.2. Mixture proportion of UHP-SHCC	22
Table 3.3. Shear strength of normal concrete and tested specimen	28
Table 3.4. Shear strength of UHPFRC and tested specimen	30
Table 4.1. Material property of UHP-SHCC	44
Table 5.1. Mixture proportion of concrete	56
Table 5.2. Mixture proportion of UHP-SHCC	56
Table 6.1. Stress and strain values of tri-linear curve model	68
Table 6.2. Stress and strain values of tri-linear curve model	73
Table 6.3. Stress and strain values of tri-linear curve model	79
Table 7.1. Tri-linear curve model from zero-span tensile behavior	89

List of Figures

Figure number and title	Page
Figure 1.1. Damaged concrete structures	1
Figure 1.2. Retrofitting concrete structures	2
Figure 1.3. Target of UHP-SHCC	3
Figure 1.4. Research framework	5
Figure 2.1. Setup for uniaxial tension test	8
Figure 2.2. Specimen in test	8
Figure 2.3. Stress-strain curves from uniaxial tensile test	9
Figure 2.4. Crack distribution of specimen from dumbbell tensile test	9
Figure 2.5. Concept of the zero-span tensile test	10
Figure 2.6. Geometry of zero-span tensile test	11
Figure 2.7. Stress-disp. curves obtained from tensile test	11
Figure 2.8. Crack pattern obtained from zero-span tensile test	12
Figure 2.9. Modeled uniaxial tensile behavior	12
Figure 2.10. Geometry for simulation of uniaxial tensile test	13
Figure 2.11. Simulated result of stress-strain relationship using the modeled curve	13
Figure 2.12. Concept of tri-linear curve model	14
Figure 2.13. Comparison of stress-strain for numerical simulation and test	15
Figure 2.14. Numerical model	15
Figure 2.15. Cases for simulation of zero-span tensile test	16
Figure 2.16. Comparison of stress-displacement curves	17
Figure 2.17. Change of longitudinal strain distribution	18
Figure 3.1. Geometry of tested specimens	21
Figure 3.2. Stress-strain curves form uniaxial tension test	22
Figure 3.3. Setup for UHP-SHCC beam test	23
Figure 3.4. Shear stress-displacement curves obtained from shear failure test	23
Figure 3.5. Crack distribution during test for case 2-100	24
Figure 3.6. Crack distribution during test for case 3-100	25
Figure 3.7. Crack distribution of the specimen at the end of test	26
Figure 3.8. Crack spacing of multiple fine cracks in the middle of shear span	26

Figure 3.9. Fracture surface of UHP-SHCC and normal concrete	31
Figure 3.10. Example of surface deformation measurement	31
Figure 3.11. Fracture surface of UHP-SHCC beam in shear failure	32
Figure 3.12 Roughness of fracture surface	33
Figure 3.13. Revised roughness of fracture surface	34
Figure 3.14. Assumed crack used to fit for crack shape of UHP-SHCC material	34
Figure 4.1. Diagram of lattice equivalent continuum model	37
Figure 4.2. Schematics of uni-axial stress-strain relationship	38
Figure 4.3. Modeling of cracked surface	39
Figure 4.4. Parameter of crack in constitutive model	40
Figure 4.5. Uniaxial stress-strain relationship in shear lattice	40
Figure 4.6. Assumption of the contact area	41
Figure 4.7. Stiffness Reducing Factor relating with crack width	41
Figure 4.8. Stress-strain relationship of rebar	42
Figure 4.9. Bond stress-slip relationship	43
Figure 4.10. Numerical model	43
Figure 4.11. Load-displacement curves	45
Figure 4.12. Relationship between crack width and strain	46
Figure 4.13. Effect of crack width by considering multiple cracking	47
Figure 4.14. Crack pattern	47
Figure 4.15. Outline of the fiber contribution on the crack surface	48
Figure 4.16. Fiber bridging stress-strain relationship	49
Figure 4.17. Effect of fiber contribution for shear stress transfer	50
Figure 4.18. Crack pattern and deformation ($a/d= 2.0$ case)	51
Figure 4.19. Crack pattern and deformation ($a/d= 3.0$ case)	51
Figure 4.20. Validation of proposed model for other specimens	53
Figure 5.1. Concept of the zero-span tensile test	54
Figure 5.2. Geometry of specimens	55
Figure 5.3. Stress versus strain from compression test	56
Figure 5.4. Results obtained from uniaxial tensile tests	57
Figure 5.5. Stress versus strain from compression test	58
Figure 5.6. Test setup of strengthened RC beam	58
Figure 5.7. Load-displacement curves obtained from test	60
Figure 5.8. Crack pattern of control beam at the end of experiment	60

Figure 5.9. Crack pattern for case U-10	61
Figure 5.10. Crack pattern for case U-30	63
Figure 5.11. Crack pattern for case U-50	64
Figure 6.1. Stress versus strain for UHP-SHCC from test and numerical model	68
Figure 6.2. Mesh size for numerical analysis	69
Figure 6.3. Comparison of load-displacement between test and numerical analysis	70
Figure 6.4. Longitudinal strain and deformation for U-10	71
Figure 6.5. Longitudinal strain and deformation for U-30	71
Figure 6.6. Geometry of fictitious zero-span tension model	73
Figure 6.7. Stress-displacement curves from fictitious zero-span tension model	74
Figure 6.8. Longitudinal strain distribution of Z-U-10	75
Figure 6.9. Longitudinal strain distribution of Z-U-30	76
Figure 6.10. Longitudinal strain distribution of Z-U-50	76
Figure 6.11. Longitudinal stresses versus displacement of zero-span tension model	78
Figure 6.12. Comparison of load-displacement curves for U-10, U-30 and U-50	80
Figure 6.13. Longitudinal strain and deformation for U-10	82
Figure 6.14. Longitudinal strain and deformation for U-30	82
Figure 6.15. Longitudinal strain and deformation for U-50	83
Figure 7.1. Geometry of RC column	86
Figure 7.2. Geometry of arrangement of reinforcements and mesh size	87
Figure 7.3. Stress-strain relationship for concrete under cyclic load	88
Figure 7.4. Stress-strain relationship of UHP-SHCC under cyclic load	89
Figure 7.5. Stress-strain relationship of steel plate under cyclic load	90
Figure 7.6. Load-displacement for case CNTR and CNTR-WEB	90
Figure 7.7. Strain distribution for case CNTR and CNTR-WEB	91
Figure 7.8. Load-disp. of strengthened RC column without web reinforcement	92
Figure 7.9. Strain distribution for case ST-6, UHP-30 and UHP-50	93
Figure 7.10. Comparisons of load-displacement relationship	94
Figure 7.11. Evaluation of damaged region by max. compressive averaged strain	95
Figure 7.12. Evaluation of damaged region by bond stress deteriorated area	95
Figure 7.13. Assumption of repairing part	96
Figure 7.14. Load-displacement relationship of repaired column	97
Figure 7.15. Deformation of repaired column after yielding	97

CHAPTER 1 INTRODUCTION

1.1 General Background

In the last decades, many concrete structures have damaged in operation. As a brittle material, concrete has weakness in resisting tensile forces, and damage concrete structures may occur due to various complex reasons. Figure 1.1 shows examples of damaged concrete structure from different type of reasons: Figure 1.1(a) shows the damaged concrete structure due to corrosion (research report of evaluation and performance monitoring of corrosion protection by fiber reinforced composite wrapping from University of Texas at Austin, 2001). The damage due to corrosion is most common for concrete structure in worldwide. In order to prevent the damage, the surface protection from salt and carbonation is required. In addition, repair and strengthening are also required for damaged structures when the cross sectional area of reinforcement is reduced due to corrosion. Figure 1.1(b) shows the damaged column due to earthquake. Concrete structures without enough reinforcements are easy to be damaged during earthquake, and they need to be repaired in short time.

(University of Texas at Austin, 2001)



(a) Concrete corrosion



(b) Damage due to earthquake

Figure 1.1 Damaged concrete structures

Moreover, repair or strengthening of aged concrete structure has become a big issue. Figure 1.2 shows some examples of strengthening concrete structures. Figure 1.2(a) shows a prestressed concrete slab by SFRC overlayer in order to increase the load bearing capacity of a concrete slab for satisfying the practical requirement (Barros and Sena-Cruz, 2001). Figure 1.2(b) shows the seismic retrofitting for concrete column with FRP jacket (Bousias et al., 2005). New earthquake design code, additional loads as well

as insufficient reinforcement in earlier design required seismic retrofitting of many concrete structures.

(Barros and Sena-Cruz, 2001)



(Bousias et al., 2005)



(a) Slab strengthened by SFRC over-layer (b) FRP jacket for seismic retrofitting

Figure 1.2 Retrofitting concrete structures

Based on the importance of repairing or strengthening for aged and damaged concrete structure, many different construction materials have been developed. However, many typical construction materials have obvious shortages, such as fiber reinforced polymer (FRP) material is strictly related to the bond and compatibility between the FRP materials and concrete (Buyukozturk, 2004), Epoxy mortar or epoxy-bonded concrete sometimes is delaminated due to expansion of epoxy caused by solar radiation (Guide to concrete repair from United States Department of the Interior Bureau of Reclamation Technical Service Center., 2006). Fiber reinforced concrete (FRC) is still quasi-brittle (Li and Wu, 1992), even if often used as repairing and rehabilitation works (ACI, 544.1R-82). Polymer cement mortars (PCM) has some limitations about cost (Fowler, 1999).

In recent years, in order to overcome the various shortages of material developed for repairing or retrofitting, High performance cementitious materials are developed for repairing or retrofitting, which can be called as High performance Fiber Reinforced Cementitious Composites (HPFRCC) (JCI-DFRCC committee, 2003). HPFRCC are normally adopted due to some advantages, such as strain-hardening behaviour. One typical type of HPFRCC is strain hardening cementitious composites (SHCC) with higher ductility, which is an attractive material for surface repairing and strengthening. The typical type of SHCC is engineered cementitious composites (ECC) (Li, 1993, 1998, 2003; Kanda and Li, 1998). ECC can exhibit tensile strain capacity more than 1 or

2%. However, the durability of ECC may be decreased due to the low performance of matrix (Naaman, 2003). Besides, the compressive strength of ECC is limited. Another typical HPFRCC is Ultra High Performance Fiber Reinforced Concretes (UHPFRC), which exhibits strain-hardening under uniaxial tension and very high strength. However, it also has a limitation of strain capacity.

In order to improve the performance of ordinary HPFRCC, a new type of HPFRCC material, called as High Performance Strain Hardening Cementitious Composites (UHP-SHCC), is developed by Prof. Kunieda et al. (Kunieda et al., 2008), with special objective of high tensile and compressive strength, large strain capacity, high workability, easy processing using conventional equipment, and lower fiber volume fraction. Figure 1.3 shows the target of UHP-SHCC (Kunieda et al., 2010), which has relatively higher hardening strain compared with ordinary UHPFRC, and relatively higher stress than ordinary SHCC.

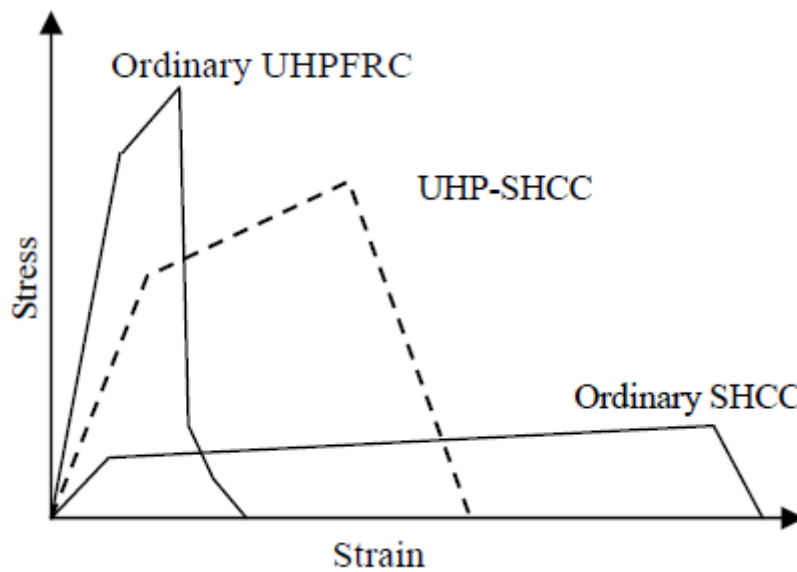


Figure 1.3 Target of UHP-SHCC

Regarding UHPFRC, it has extremely low water to binder ratio lower than 0.2 generally, and it also has a high percentage of steel fibers, so it shows higher strength. Regarding SHCC, it has higher water to binder ratio of the matrix, similar to an ordinary cement mortar, and polyvinylalcohol (PVA) fiber or high strength polyethylene (PE) fiber are usually used, so it shows larger strain capacity. However, UHP-SHCC has a dense matrix with lower water to binder ration between 0.18 and 0.22, which is smaller than SHCC, but larger than UHPFRC. Moreover, PE fibers are adopted in UHP-SHCC.

Due to the large advantages such as hardening strain as well as high tensile and compressive strength, UHP-SHCC is suitable for repairing damaged concrete structures or strengthening the aged concrete structures in operation, it can have a bright future.

1.2 Purpose of This Study

Although having the excellent properties, High Performance Fiber Reinforced Cementitious Composites (HPFRCC) is not widely adopted in construction until now. Civil engineers seem to lack the necessary innovative spirit to apply this new type of materials in repair or strengthening concrete structures. They tend to adopt traditional material for repair or strengthening damaged or aged concrete structures such as steel plates. On the other hand, one of the primary obstacles preventing the widespread use of HPFRCC is the lack of enough investigation on fracture behavior of this material, especially lacking reliable numerical models for this class of materials (Triub, 2011).

Until now, there are seldom numerical researches on fracture behavior of HPFRCC. Paepegem and Degrieck proposes a coupled approach of two commonly used approaches of the residual stiffness and the residual strength approach to model fatigue damage of fiber reinforced composites (2002). Kunieda et al. evaluates the tensile fracture process of SHCC by means of three-dimensional meso-scale analysis (2011). Trub proposes a material model for the numerical simulation of HPFRCC in macro level, considering the three phases of HPFRCC material property: up to cracking strength, HPFRCC is modeled by means of a linear elastic law; the sequent hardening phase is described using a rotating smeared-crack model and upon reaching tensile strength, the phase of softening of the material and strain localization considers as a single discrete crack (Trub, 2011).

As mentioned above, UHP-SHCC is one type of HPFRCC with special target, which is useful for repairing or strengthening the damaged or aged concrete structures. In order to widely use of UHP-SHCC, the investigation on fracture behavior of UHP-SHCC is very important, especially on the reliable numerical evaluation method of this material.

In this study, numerical evaluation method on UHP-SHCC is proposed systemically, and numerical evaluation on fracture behavior of UHP-SHCC is conducted, compared with experimental result.

1.3 Study Objective and Research Framework

1.3.1 Study objective

The aim of this study is to investigate the fracture behaviour of UHP-SHCC by means of experiment and numerical method. Based on the experimental investigation of mechanical performance of UHP-SHCC materials, the reliable numerical model on fracture behaviour of UHP-SHCC materials is proposed in this study. These models are

confirmed based on the Comparison between experimental and numerical analysis.

1.3.2 Research framework

Figure 1.4 shows the framework of this research. In this study, the tri-linear curve model considering fracture energy on tensile behavior of UHP-SHCC material is proposed in material level. In structural level, flexural behavior of RC beam strengthened by UHP-SHCC and shear behavior of UHP-SHCC beam are considered. In the flexural behavior of RC beam strengthened by UHP-SHCC, the experiment on this behavior is investigated, and a new type of zero-span tensile model is proposed considering a fictitious elastic material for numerical analysis of the flexural behavior of RC beam strengthened by UHP-SHCC, then numerical evaluation on this flexural behavior is conducted. In shear behavior of UHP-SHCC beam, the shear constitutive model of UHP-SHCC is proposed considering the feature of crack surface and fiber bridging effect, and then the shear failure behavior is numerically evaluated. Based on these models, the strengthened effect of RC column is evaluated.

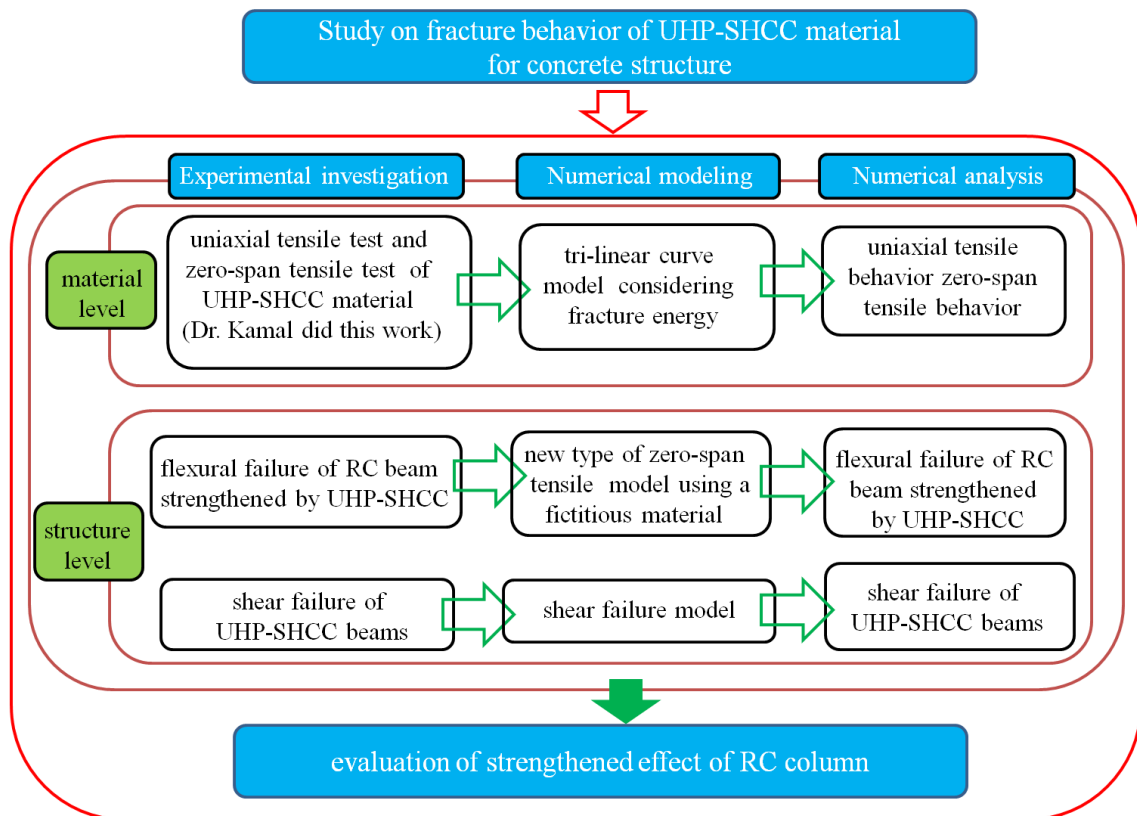


Figure 1.4 Research framework

1.4 Overview of the Thesis Content

This part briefly introduces contents of the next chapters of the dissertation.

Chapter 1 is the introduction of the dissertation including background and purpose of the study, study objectives and the framework of the study.

Chapter 2 presents a tri-linear curve model considering fracture energy for uniaxial tensile behavior of UHP-SHCC, and zero-span tensile behavior of UHP-SHCC is simulated using this model, based on the experimental result from Dr. Kamal.

Chapter 3 presents investigation on load versus displacement, crack processes and cracking pattern of UHP-SHCC beam in shear failure by means of experiment, and the shape of fracture surface of the tested UHPS-SHCC beam is also investigated.

Chapter 4 presents numerical model on shear stress transfer for shear behavior of UHP-SHCC members, considering roughness of crack surface depending on asperity height and shape of crack surface (θ), crack width depending on crack distribution, and fiber bridging contribution. This model is confirmed applicably for numerical evaluation of UHP-SHCC members in shear failure.

Chapter 5 presents experimental investigations on flexural failure behavior of RC member strengthened by UHP-SHCC layer with different thicknesses. In the experiment, load versus displacement, crack processes and cracking pattern of the specimens are investigated. Especially, the cracking opening performance of UHP-SHCC layer with different thicknesses is investigated deeply, which is used as a strengthened material for RC substrate members.

Chapter 6 presents a new type of zero-span tensile model using a fictitious elastic material, and the numerical behavior of RC member strengthened by UHP-SHCC in flexural failure is investigated using this zero-span tensile model. In the numerical result of RC member strengthened by UHP-SHCC in flexural failure, load versus displacement, crack processes and cracking pattern of numerical results are investigated, especially focusing on the crack opening performance of UHP-SHCC layer with different thicknesses.

Chapter 7 presents the numerical evaluation of strengthened effect of RC column with stirrup and without stirrup cases, using the proposed zero-span tensile model and shear failure model. The strengthened effect is also compared with the strengthening effect of steel plate. Moreover, the numerical result for strengthened damaged concrete structures due to earthquake is shown

Chapter 8 includes summary and conclusion derived from this study.

CHAPTER 2

MODELING OF TENSILE BEHAVIOR OF UHP-SHCC MATERIAL

2.1 Introduction

UHP-SHCC has been expected to apply to structural application, due to its ultra high performance for retrofitting, such as high tensile strength as well as large strain capacity for tensile behavior. Therefore, the tensile behavior of UHP-SHCC material is required to understand clearly. In this chapter, the tensile behavior of UHP-SHCC materials on uniaxial tensile behavior and zero-span tensile behavior (localized behavior due to multiple fine cracks concentrated and adjacent to existing crack in damaged structure) is described based on the uniaxial and zero-span tensile test carried out by Kamal et al. (Kamal et al., 2008), and the material modeling is proposed considering fracture energy. The effectiveness of this tri-linear curve model is also verified by the uniaxial and zero-span tensile test.

2.2 Tensile behavior of UHP-SHCC material

2.2.1 Uniaxial tensile behavior

2.2.1.1 Test setup and material

In the uniaxial tensile test, UHP-SHCC with fiber content of 1.5% as volume fraction is prepared. Table 2.1 shows the mix proportions of this UHP-SHCC material (Kamal et al., 2008).

Table 2.1 Mixture proportion of UHP-SHCC

Water/Binder (%)	Unit content (unit: kg/m ³)						
	Water	Binder	Silica fume	Fine sand	PE fiber	Super-plasticizer	Air reducing agent
18	263.7	1338.6	334.7	167.3	14.6	33.5	7.4

Note: binder means cement + silica fume

Uniaxial tensile test is conducted by Kamal et al. (Kamal, 2008; Kamal et al., 2008), in order to investigate the tensile behavior of UHP-SHCC material. Figure 2.1 shows the setup of uniaxial tensile test for UHP-SHCC specimen. In the setup, a Pi-type displacement transducer is glued on each of the two surfaces of the specimen to measuring the opening displacement. Gauge length of the transducer is 100mm and the sensitivity of each transducer is 1/2000 mm. The capacity of the transducers was equal to ± 5 mm. The load is measured by load-cell having the capacity of 50 kN. In uniaxial tensile test, the specimen has dumbbell shape, with the tested cross section of 13x30mm, as shown in Figure 2.2. The uniaxial tensile test is implemented on the MTS system.



Figure 2.1 Setup for uniaxial tension test (Kamal, 2008)

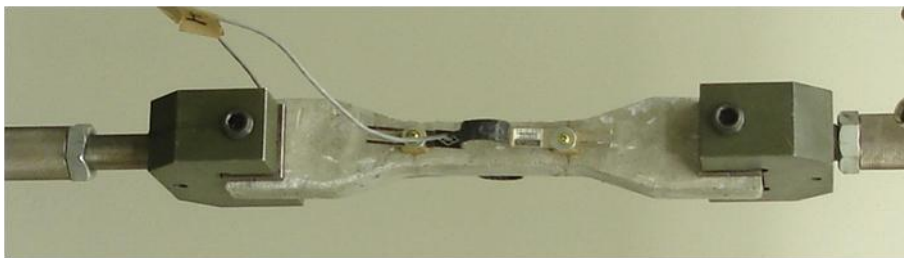


Figure 2.2 Specimen in test (Kamal, 2008)

2.2.1.2 Result for uniaxial tensile test

Figure 2.3 shows the stress-strain relationship obtained from uniaxial tensile test after 14 days. All the specimens exhibit not only significant strain hardening behavior but also scatter of ultimate strain. After the occurrence of initial cracks when its stress reaches initial tension strength at point A, the load continues to increase until the stress achieves ultimate tensile stress at Point B and C for each specimen. The maximum ultimate tensile strength can reach 11.6N/mm^2 , and the corresponding strain was 3.37%. The averaged hardening strain was 2.8%, and the averaged ultimate tensile strength is 10N/mm^2 .

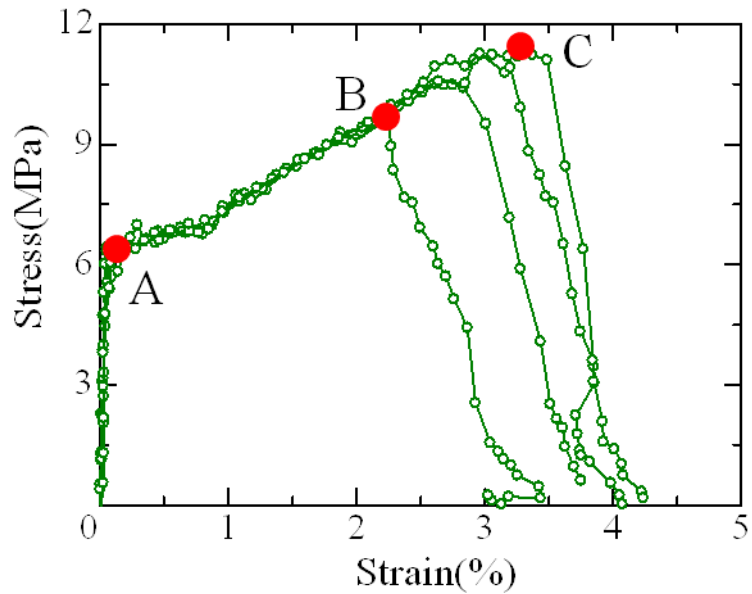


Figure 2.3 Stress-strain curves from uniaxial tensile test (Kamal, 2008)

Figure 2.4 shows the crack distribution obtained after uniaxial tensile test. It can be clearly seen the distribution of multiple fine cracks in the tested specimen. The average crack spacing is about 2.5mm of this specimen, which is dependent on fiber content and strength of cement matrix. The multiple fine cracks follow strain hardening behavior with bridging effect of fiber after cracking at Point A. Finally, one of multiple fine cracks localized at Point B in Figure 2.3 and then load decreases with slip of fiber.



Figure 2.4 Crack distribution of specimen from dumbbell tensile test (Kamal, 2008)

2.2.2 Zero-span tensile behavior

2.2.2.1 Concept of zero-span tensile test

When UHP-SHCC used as repairing or retrofitting materials for damaged concrete structure with existing crack, the multiple fine cracks are concentrated adjacent to the existing crack in damaged concrete structure, which means the tensile behavior of UHP-SHCC material is localized in a ranged area. This behavior can be called as zero-span tensile behavior. Zero-span tensile behavior has been investigated by mans of

zero-span tensile test, which has been carried out by Kamal et al. (Kamal et al., 2008).

Zero-span tensile test is a method with special boundary conditions to evaluate zero-span tensile behavior, which is used to reflect those of surface repair applications (Kamal et al., 2008; Kamal, 2008). The main concept is to conduct the tensile test on a very short span to evaluate the resistance against localized fracture of the surface repair material, as illustrated in Figure 2.5. This test can evaluate the crack opening performance of UHP-SHCC on substrate with crack.

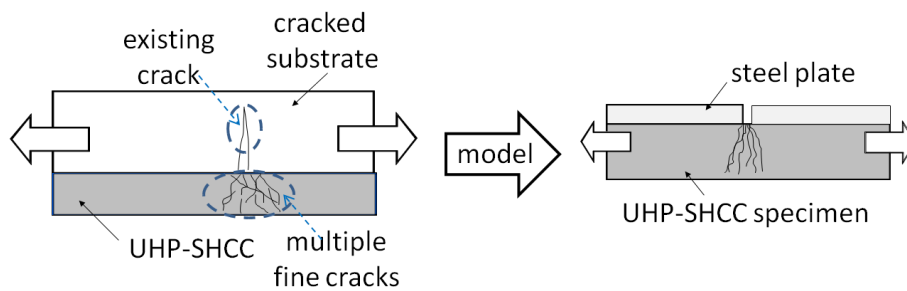


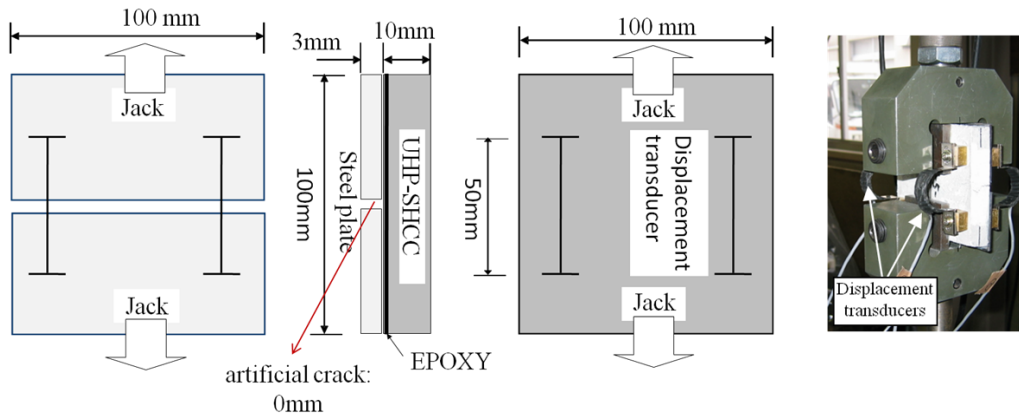
Figure 2.5 Concept of the zero-span tensile test

2.2.2.2 Geometry of zero-span tensile test

Figure 2.6(a) shows the geometry for zero-span tensile test, referenced from Kamal et al. (Kamal et al. 2008). The size of the specimen is 100x100mm with thickness of 10mm. Steel plates with thickness of 3mm are glued on the UHP-SHCC specimen by epoxy adhesive. The artificial crack formed by the gap between the steel plates should reflect the crack width of the cracked substrate. In this zero-span tensile test, the most severe condition where an artificial crack width of 0mm is prepared to reflect the crack in the substrate and to induce localized fracture.

Figure 2.6(b) shows the setup for zero-span tensile test with fixed boundary condition. In zero-span tensile test, four Pi-type displacement transducers are adopted to measure the opening displacement at the artificial crack. Two transducers are fixed on the specimen side and the other two transducers are fixed on the steel plate side. The measurement length of the transducers is 50mm and the sensitivity of each transducer is about 1/2000mm. The loading rate is about 0.2mm/min, and the loading is terminated when the displacement is over 2mm, which is equal to the capacity of the transducers. The load is measured by load-cell having the capacity of 50kN. All tests are carried out during the age of 14 days.

The specimens for zero-span tensile test have the same material properties with specimens for uniaxial tensile test in section 2.2.1.



(a) Geometry of zero-span tensile test

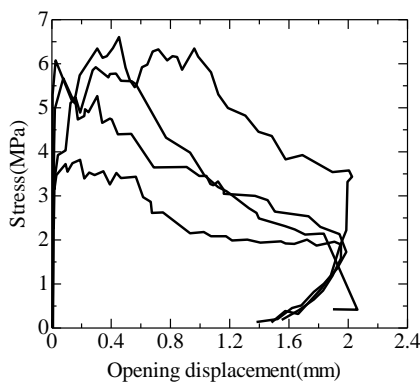
(b) test setup

Figure 2.6 Geometry of zero-span tensile test (referenced from Kamal et al., 2008)

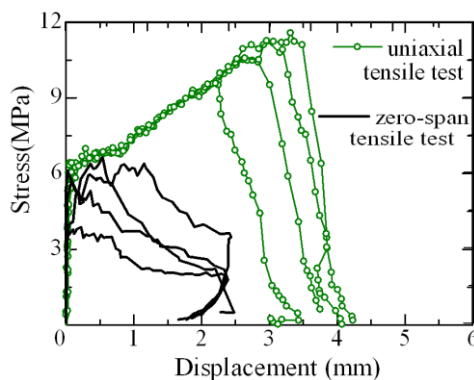
2.2.2.3 Experimental result for zero-span tensile test

Figure 2.7 shows the stress-displacement curves obtained from zero-span tensile test and Comparison of stress versus displacement from zero-span tensile test and uniaxial tensile test (Kamal et al., 2008). The zero-span tensile behaviors exhibit different behavior from the uniaxial tensile behavior. That is, the tensile strength and the crack opening displacement correspond to tensile strength decrease from those of uniaxial tensile behavior. This difference of tensile behavior is caused by the difference of crack distribution of UHP-SHCC layer, in which crack distribution is concentrated adjacent to an existing crack in substrate. Figure 2.8 shows the crack pattern of zero-span tensile test. The multiple fine cracks are concentrated and ranged in the area of adjacent to existing artificial crack, the width of this ranged area is 9mm by measurement.

Therefore, the tensile behavior of UHP-SHCC used for repairing or retrofitting concrete structure with existing crack, is different from the uniaxial tensile behavior of UHP-SHCC material.



(a) zero-span tensile test



(b) zero-span tensile test and uniaxial tensile test

Figure 2.7 Stress-disp. curves obtained from tensile test (Kamal et al., 2008)

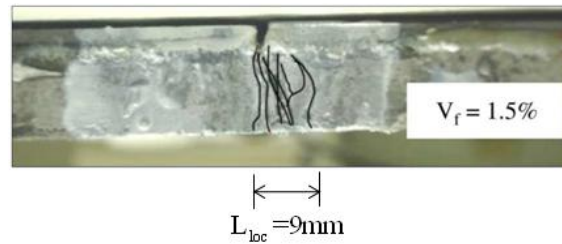


Figure 2.8 Crack pattern obtained from zero-span tensile test (Kamal et al., 2008)

2.3 Modeling of tensile behavior of UHP-SHCC materials

In order to apply the tensile behavior of UHP-SHCC material to concrete structure, it needs to be evaluated numerically. In this section, the numerical model of tensile behavior of UHP-SHCC material is proposed, and the applicability of this numerical model is verified.

2.3.1 Numerical modeling of uniaxial tensile behavior for UHP-SHCC materials

2.3.1.1 Simulation using stress-strain relationship obtained from test

The uniaxial tensile stress-strain relationship obtained from experiment can be abstracted as tri-linear curve with initial cracking point and maximum loading point, which can reflect the mechanism of the interaction between matrix and PE fibers (initial cracking point with matrix cracking, maximum loading point with slip of fibers).

Figure 2.9 shows the modeled uniaxial tensile behavior with lower limit and upper limit of ultimate tensile strength based on stress-strain curves obtained from dumbbell-shaped test.

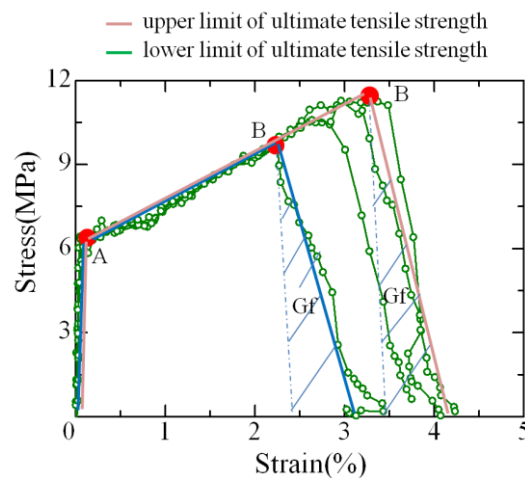


Figure 2.9 Modeled uniaxial tensile behavior

Numerical simulation is conducted by using the mentioned tri-linear curve above. Figure 2.10 shows the geometry for simulation of uniaxial tensile test with the mesh size of 10mm and 20mm respectively.

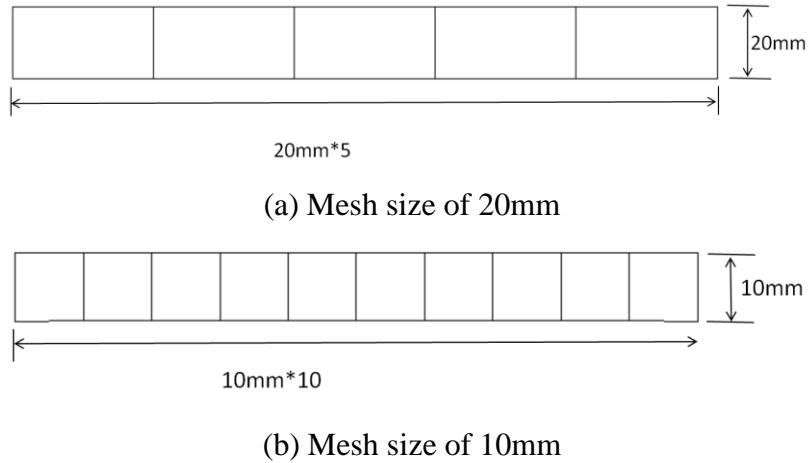


Figure 2.10 Geometry for simulation of uniaxial tensile test

Figure 2.11 shows the result of stress-strain curves obtained from numerical simulation with different mesh size of 10mm and 20mm, using the lower and upper limit of scatter model shown in Figure 2.10. It can be illustrated that the simulated result is not coincided with the test result, the results show sudden drop after maximum stress. That is the well-known problem of result depending on mesh size of elements (Bazant, 2002).

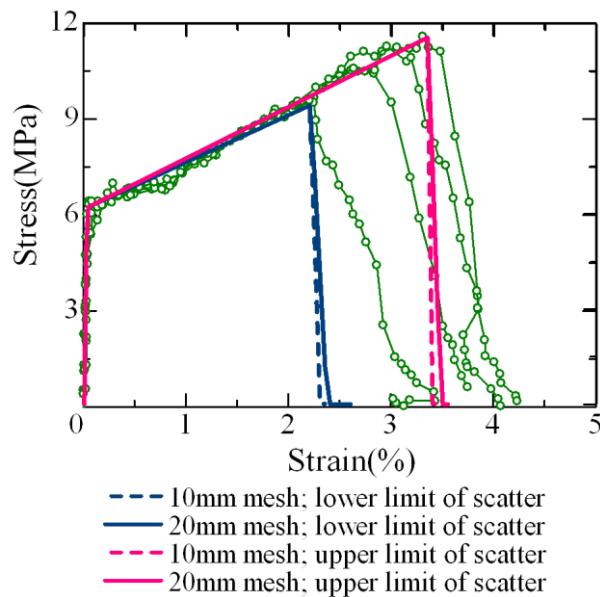


Figure 2.11 Simulated result of stress-strain relationship using the modeled curve

2.3.1.2 Tri-linear curve model considering fracture energy

In order to solve the problem mentioned above, the tri-linear curve model considering fracture energy is proposed for the stress-strain relationship of UHP-SHCC under uniaxial tension herein. Fracture energy G_f is defined by the area of softening part of stress-displacement relationship as shown in Figure 2.12(a), δ means the displacement obtained from uniaxial tensile test (mm). Figure 2.12(b) shows the stress-strain relationship used in analysis. Point A is corresponding to the point where initial crack occurs in uniaxial tensile test, and Point B is corresponding to the point achieves ultimate tensile strength in uniaxial tensile test. The strain of point C is represented by Eq.(2.1) considering the fracture energy in localized element. By considering the fracture energy (Bazant, 2002), a unique load-displacement relationship could be obtained independent on element size.

$$\varepsilon_C = \varepsilon_B + \frac{2G_f}{\sigma_B \cdot L_{elm}} \quad (2.1)$$

Where ε_B : Strain at peak stress
 σ_B : peak stress (N/mm²)
 L_{elm} : Element size (mm)
 ε_C : Strain at stress of 0.
 G_f : fracture energy (N/mm).

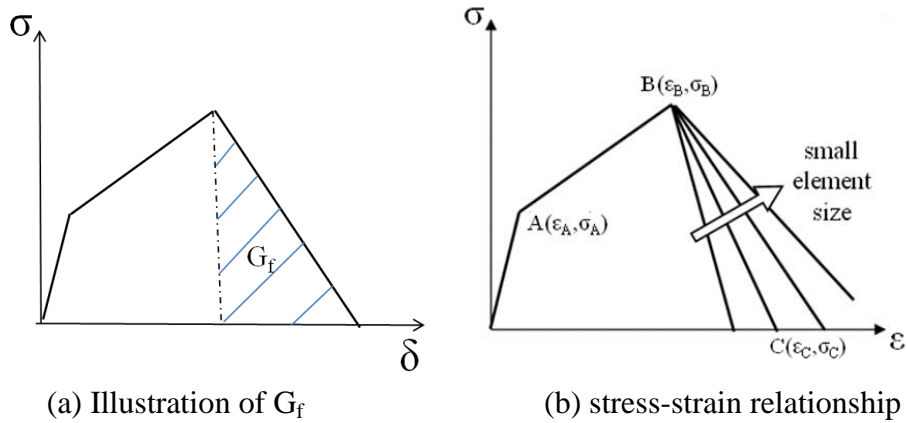


Figure 2.12 Concept of tri-linear curve model

2.3.1.3 Confirmation of the proposed tri-linear curve model

In order to clarify the validation of the tri-linear curve model considering fracture energy, numerical simulation is conducted herein. Figure 2.13 shows the stress-strain relationship obtained from numerical simulation and test. It can be confirmed that there is no element dependency, and analytical result is identical well with the dumbbell

tensile test result. Therefore, this proposed tri-linear model can be adopted for numerical analysis for UHP-SHCC.

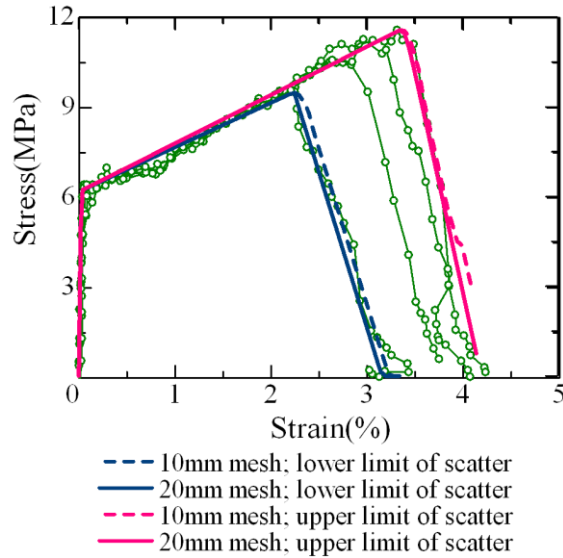


Figure 2.13 Comparison of stress-strain for numerical simulation and test

2.3.2 Numerical Modeling of zero-span tensile behavior for UHP-SHCC materials

2.3.2.1 Numerical model for zero-span tensile test

The zero-span tensile tests as shown in Figure 2.6 are simulated. Figure 2.14 shows the numerical model. The artificial crack width between steel plates is assumed as 1.0mm as small value. Then the element size is set as 1.0mmx1.0mm, which is smaller than crack space. All the nodes of left end are fixed at longitudinal direction, and all the nodes of right end are applied load at longitudinal direction. The same nodes are used for the interface between steel plate and UHP-SHCC, due to the assumption of perfect bond between steel plate and UHP-SHCC from original concept of zero-span tensile test, using epoxy and rough surface of steel plate.

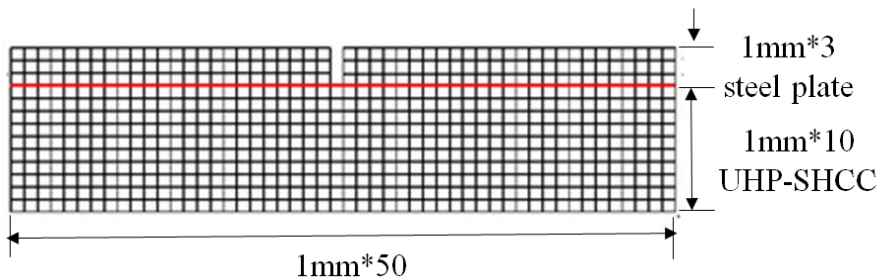


Figure 2.14 Numerical model

The relationship in compression is assumed as linear elastic having the same Young's modulus with the tensile behavior. The shear stress transfer of cracked surface is assumed as negligibly small value. For the stress-strain relationship in tension, two patterns are applied for each specimen as shown in Figure 2.15. They are modeled by the cases with upper limit and lower limit of the tensile strength, which have different tensile strength and same softening slope. For both cases, the softening branches are modeled by the function of element size as mentioned above, considering fracture energy. The values of point A, B, C in tri-linear model for each case are summarized in Table 2.2.

. **Table2.2** Stress and strain values in tri-linear model

case	Point A		Point B		Point C	
	stress	strain	stress	strain	stress	strain
lower limit of ultimate tensile strength	6.16	0.0002	9.73	0.022	0	0.63
upper limit of ultimate tensile strength	6.16	0.0002	11.7	0.0329	0	0.77

Note: the units of stress is N/mm^2

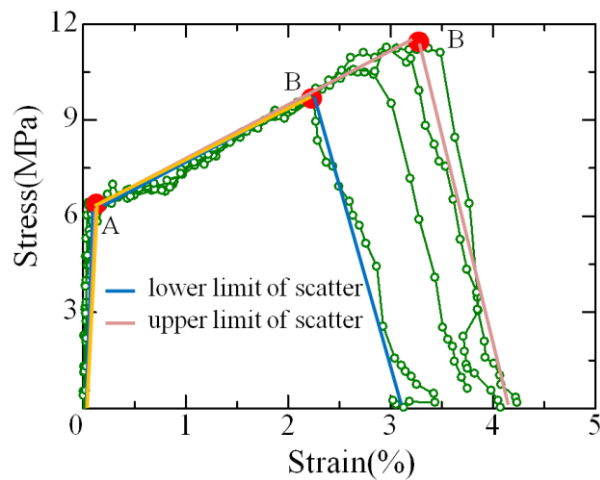


Figure 2.15 Cases for simulation of zero-span tensile test

2.3.2.2 Numerical result for zero-span tensile test

Figure 2.16 shows the comparison of stress-displacement relationship between zero-span tensile test and numerical results. In the cases of lower limit and upper limit of ultimate tensile strength, the zero-span tensile behavior exhibits the different tensile strength and similar post peak behavior, which is similar with material properties behavior. The case of lower limit of ultimate strength simulates the zero-span tensile behavior better than the case of upper limit of scatter for ultimate strength. This may

imply that the zero-span tensile behavior is occupied by the weaker behavior of materials.

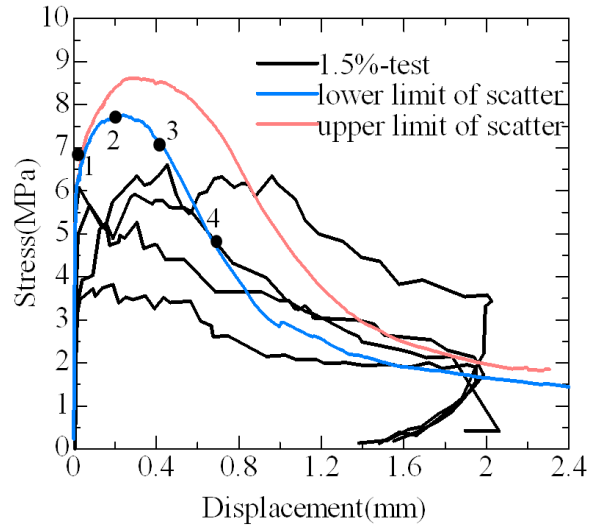
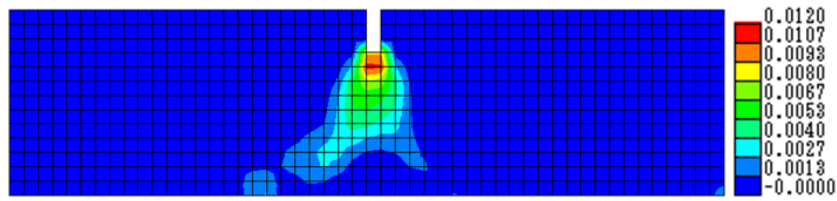


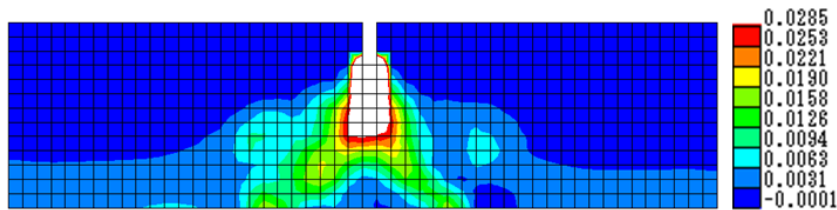
Figure 2.16 Comparison of stress-displacement curves

Figure 2.17 shows longitudinal strain distribution at point 1 to 4 marked in Figure 2.16. The white part in Figure 2.17 is larger strain area. It can be understood that cracks propagate from the artificial crack part due to stress concentration and strain distribute through the depth of cross section. Therefore, tensile strength of zero-span tensile test became smaller value than that of uniaxial tensile test. Then, the strain distribution spread from the artificial crack part. This behavior is similar with crack pattern observed in the tests as shown in Figure 2.8. After peak load, strain localize to downside from artificial crack part with the similar distributed area. The distributed areas are almost the same with the cracking area of test specimen.

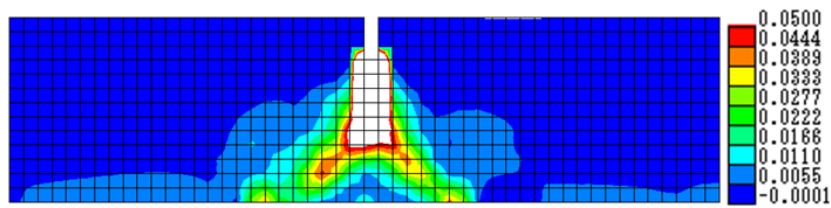
It is understood that the zero-span tensile behavior such as stress-displacement relationship and strain distribution behavior can simulate numerically using small mesh size and applying the uniaxial tensile behavior considering fracture energy.



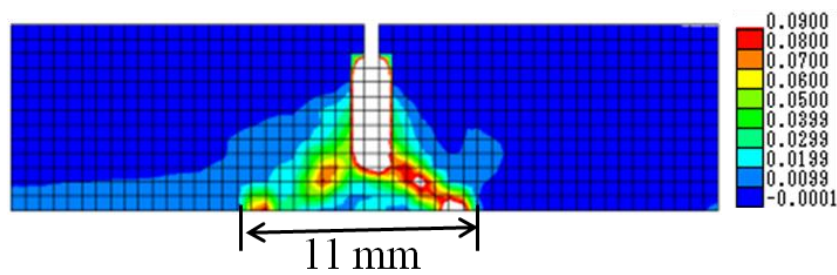
(a) Longitudinal strain at point 1



(b) Longitudinal strain at point 2



(c) Longitudinal strain at point 3



(d) Longitudinal strain at point 4

Figure 2.17 Change of longitudinal strain distribution

2.4. Conclusion

Tensile behavior of uniaxial tensile behavior and zero-span tensile behavior for UHP-SHCC material is described based on experiment carried out by Kamal. The tri-linear curve model considering fracture energy for uniaxial tensile behavior of UHP-SHCC is proposed. The tensile behavior is simulated by using the proposed

model.

(1) The material modeling of tri-linear curve model for UHP-SHCC is proposed considering fracture energy. This model can be applied to tensile behavior, and the effectiveness of this model is verified by the uniaxial tensile behavior. Based on the comparison between experimental and numerical results of uniaxial tensile behavior, the analytical result is identical well with the uniaxial tensile test result without element dependency.

(2) The behavior of zero-span tensile test is investigated by numerical analysis. Zero-span tensile behavior can be solved using small mesh size. In zero-span tensile behavior, cracks propagate from the artificial crack part due to stress concentration and strains distribute through the depth of cross section.

(3) The simulation results considering the scatter of ultimate tensile strength of UHP-SHCC show similar behavior when lower limit stress-strain relationship is applied. This means that the zero-span tensile behavior may be occupied by the weaker behavior of materials.

CHAPTER 3

EXPERIMENTAL INVESTIGATION ON SHEAR BEHAVIOR OF UHP-SHCC BEAMS

3.1. Introduction

The applicability of UHP-SHCC used as repair material has been confirmed, such as the method of surface protection, increasing the thickness of slab, rapid restoration of damage concrete structures (Kunieda, 2012). However, the research on the applicability of UHP-SHCC used as a construction material has not been studied enough, due to UHP-SHCC is a new material with special material properties of large strain capacity as well as high tensile and compressive strength (Kunieda et al., 2008). On the other hand, UHP-SHCC is not studied yet as one type of the cementitious composite material, and the other cementitious composite material such as ECC has been studied (Li, 1993, 1998, 2003; Kanda and Li, 1998), and also has been used as construction material (Li, 2003).

In this chapter, the shear behaviour of UHP-SHCC beams is clarified by experimental investigation. Four specimens of $a/d=2$ and 3 are tested by three point loading method, then experimental result of load versus displacement, crack processes and cracking pattern are investigated. Moreover, the shape of fracture surface of these UHP-SHCC beams is also surveyed due to the different shear behaviour of UHP-SHCC beams, compared with normal concrete beams.

3.2 Experimental Programs

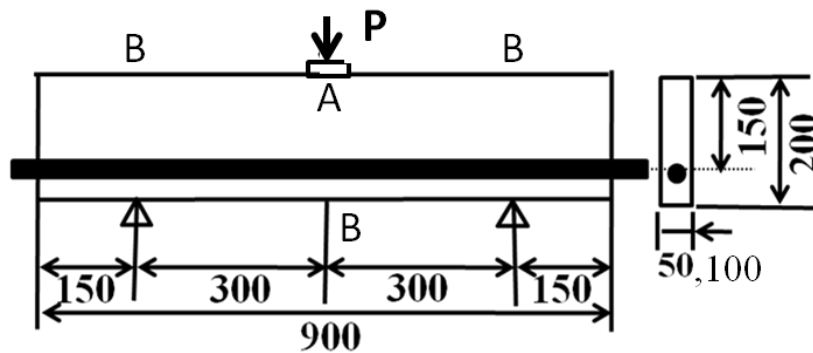
3.2.1 Geometry of UHP-SHCC beams

Four specimens of $a/d=2$ and 3 are prepared for experiment, which will be expected to be failed in diagonal shear. Figure 3.1 shows the geometry of the four specimens. The effective depths of all the members are 150mm. Two of the four specimens have the shear spans lengths with 300mm and the left two specimens have the shear span length with 450mm. High tensile strength deformed bar with diameter of 25mm (Young's modulus is 200GPa and yield strength is 1050N/mm²) is arranged as longitudinal bar. The differences between the two specimens with the same a/d are the longitudinal reinforcement ratio and the width.

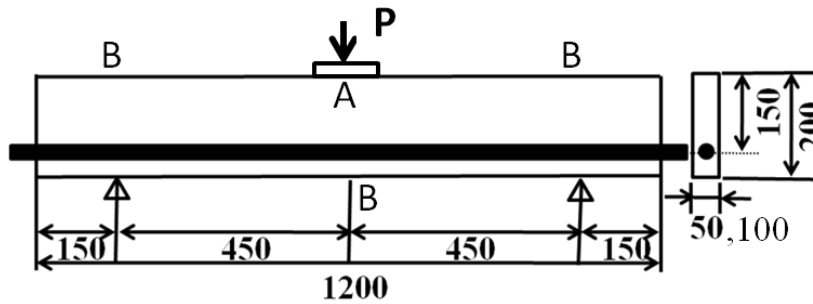
Table 3.1 Details of specimens

Specimen	a/d	effective height (mm)	Width (mm)	reinforcement ratio (%)
2-50	2	150	50	3.37
2-100		150	100	1.69
3-50	3	150	50	3.37
3-100		150	100	1.69

Note: the reinforcement is deformed bar with high tensile strength of 1050N/mm²



(a) Specimen a for a/d=2



(b) Specimen b for a/d=3

Figure 3.1 Geometry of tested specimens (unit: mm)

3.2.2 Material

Table 3.2 shows the mix proportions of UHP-SHCC material. Water to binder ratio (W/B) is 0.22. Low heat Portland cement (density: 3.14g/cm³) is used, and 15% of the cement content is substituted for a silica fume (density: 2.2g/cm³). The quartz sand (less than 0.5mm in diameter, density: 2.68g/cm³) is used as the fine aggregate. High strength polyethylene (PE) fiber is chosen for UHP-SHCC and the fiber volume in the mix is

1.5%. The diameter and length of the PE fibers are 0.012mm and 6mm, respectively. Superplasticizer is used to enhance the workability of the matrixes.

Table 3.2 Mixture proportion of UHP-SHCC

Water/Binder (%)	Unit content (unit: kg/m ³)							
	Water	Cement	Silica fume	Fine sand	PE fiber	Expansion agent	Super-plasticizer	Air reducing agent
22	338.5	1267.9	230.8	153.9	14.6	40.0	15.4	0.06

Note: binder means cement + silica fume

Figure 3.2 shows the stress-strain relationship obtained from uniaxial tensile tests of dumbbell specimens (tested cross section: 13x30mm) for UHP-SHCC material, and the strains are obtained from the elongation rate in measurement length of 100 mm. It can be seen not only strain hardening behavior but also scatter of hardening strain. The lower limit and upper limit hardening strain are 0.85% and 2.0%, and the ultimate tensile strengths corresponding to them are 5.3N/mm² and 6.7N/mm² respectively. For compressive properties, 3 cylindrical specimens having the size of $\phi 50 \times 100$ mm are tested at the age of 28days. The compressive strength and Young's modulus of UHP-SHCC are 91N/mm² and 29GPa.

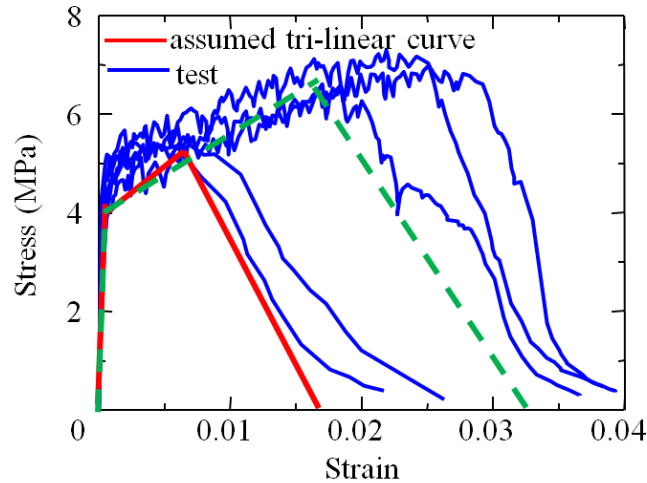


Figure 3.2 Stress-strain curves form uniaxial tension test

3.2.3 Setup of the experiment

At the age of 28days after casting of specimens, all UHP-SHCC beams are loaded under three-point loading setup, as shown in Figure 3.3. In the experiment,

displacements at loading points and middle point, and load are measured by displacement transducers and load-cell, which are marked as Point B and A in Figure 3.1. The loading test is terminated when sudden drop in the load is observed.

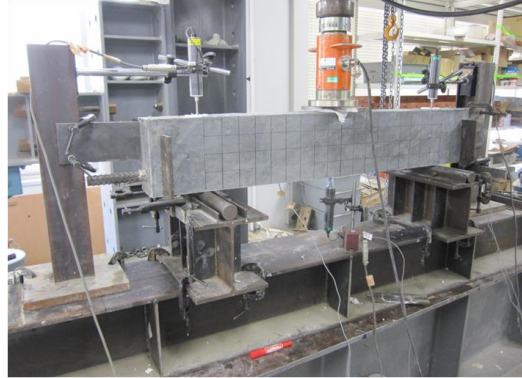


Figure 3.3 Setup for UHP-SHCC beam test

3.3. Experimental result of UHP-SHCC beam in shear failure

3.3.1 Load-displacement relationship

Figure 3.4 shows the shear stress-displacement relationship of four specimens with $a/d=2$ and $a/d=3$ obtained from shear failure test. Shear stress is defined by the shear force dividing the effective area of section as effective height multiplying width.

The maximum shear stress of four cases with the name of 2-50, 2-100, 3-50 and 3-100 (listed in Table 3.1) are 11.6 N/mm², 9.8 N/mm², 8.3 N/mm² and 7.0 N/mm² respectively, which means specimens with a/d of 2 have larger load carrying capacities than those of specimens with a/d of 3.

The relationship show linear curve until near the maximum shear strength and sudden failure occur. This behavior may be due to the smooth crack surface of UHP-SHCC, which will be discussed later.

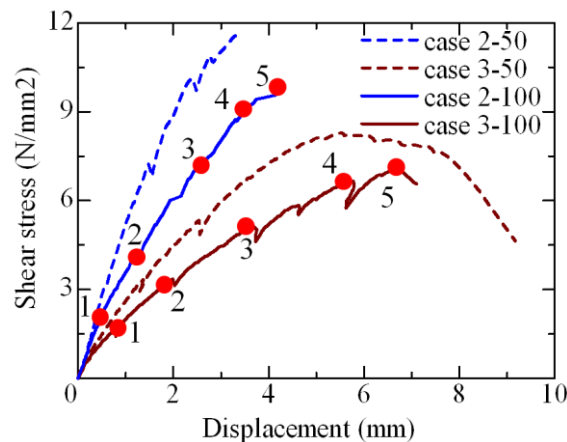


Figure 3.4 Shear stress-displacement curves obtained from shear failure test

3.3.2 Crack propagation of the UHP-SHCC beams

Figure 3.5 shows the propagation of crack pattern for case 2-100 with $a/d=2$ and width of 100mm, corresponding to the position of Point 1 to 5 marked at Figure 3.3. At point 1 (lower load level with shear stress of 2N/mm^2), flexural multi-fine cracks occur firstly. At point 2 (load level with shear stress of 4N/mm^2), some multi-fine cracks occur in the middle of shear span independent on flexural cracks. At point 3 and 4 (load level with shear stress of 7.3N/mm^2 and 9.3N/mm^2), the multiple fine cracks increase gradually, which means the multiple fine cracks increases with the increasing of load level, and multiple fine cracks in shear direction play dominant role. At Point 5 (peak load with shear stress of 9.8N/mm^2), it obviously exhibits the localization among multiple fine cracks, it implies the load dropped suddenly due to the localization of multiple fine cracks. The angle between multiple fine cracks along diagonal shear direction and axial direction is about 33.5° , as shown in Figure 3.5(d).

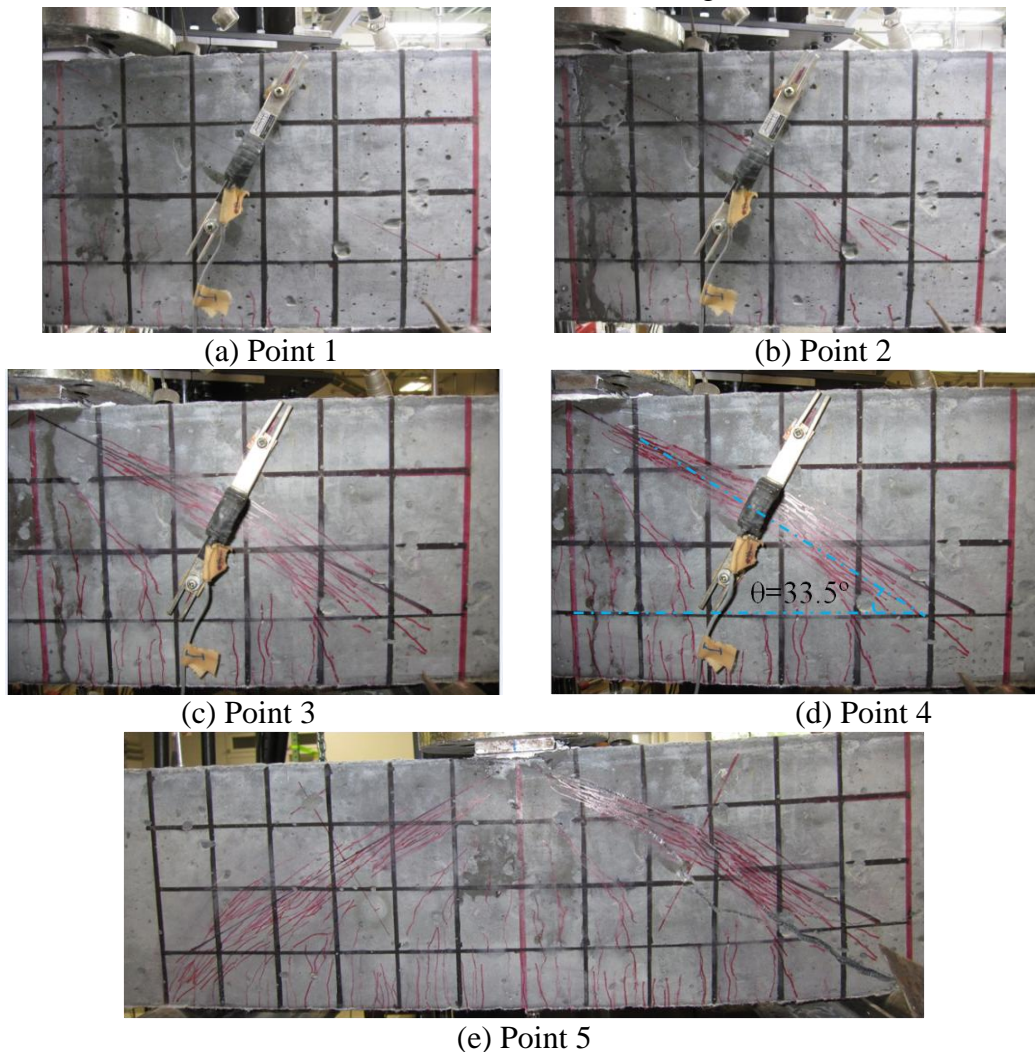


Figure 3.5 Crack distribution during test for case 2-100

Figure 3.6 shows the propagation of crack pattern of specimen 3-100 with $a/d=3$ and width of 100mm, corresponding to the position of Point 1 to 5 marked at Figure 3.3. From Figure 3.6, it can be easily seen this specimen shows similar crack propagation behavior with that of specimen 2-100 with $a/d=2$ and width of 100mm (shown in Figure 3.5). For case 3-100, flexural multi-fine cracks occur firstly at point 1 (lower load level with shear stress of 1.7N/mm^2), then multiple fine cracks occur in the middle of shear span, and the number of multiple fine cracks increases with the increasing of load level with shear stress from 3.3N/mm^2 to 6.7N/mm^2 (point 2 to 4), and multiple fine cracks in shear direction play dominant role. Thereafter, one of the multiple fine cracks localizes until peak load with the shear stress of 7.0N/mm^2 (point 5), then the specimen fractured in shear failure. The angle between multiple fine cracks along diagonal shear direction and axial direction is about 28° , as shown in Figure 3.6(d).

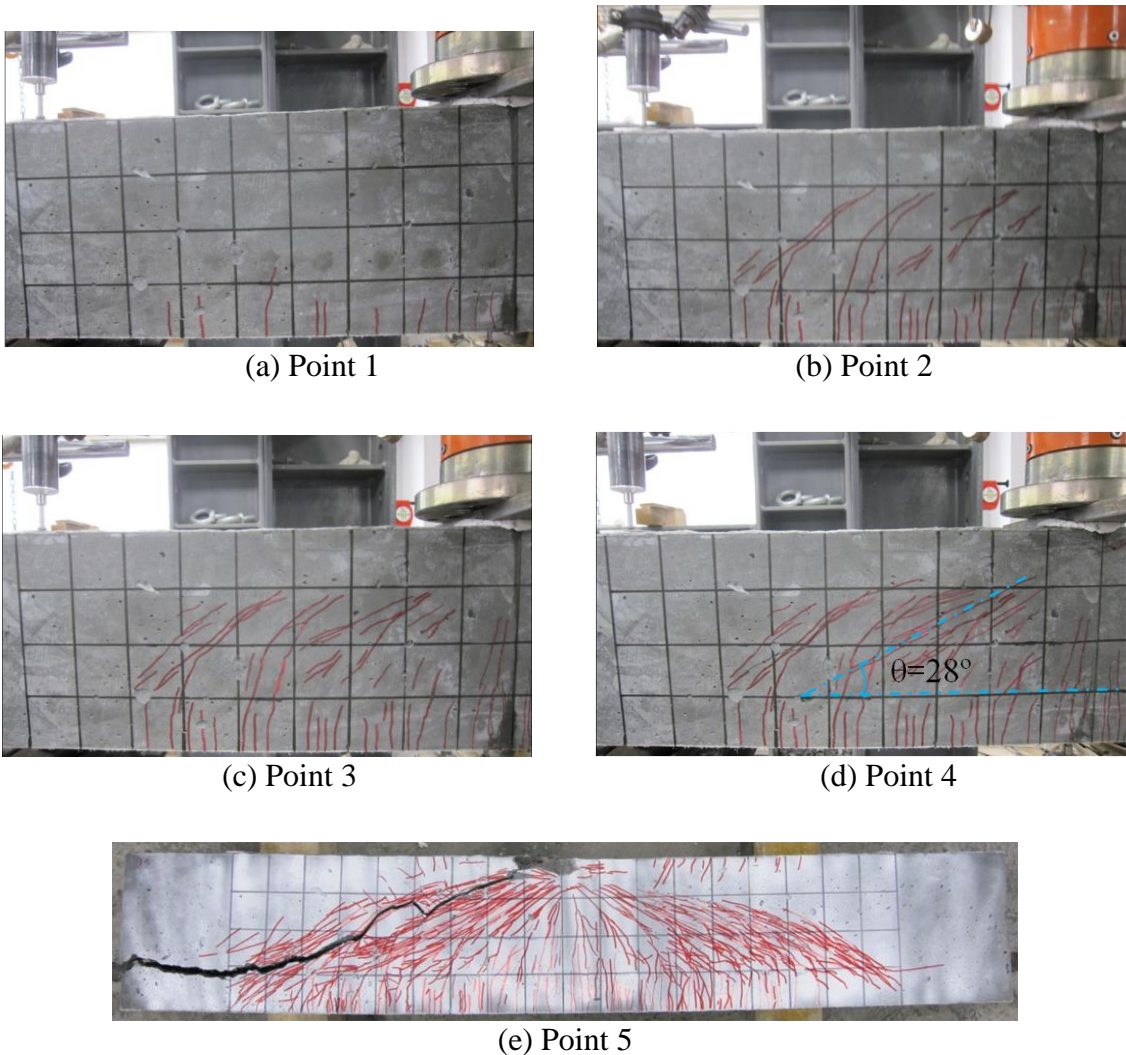
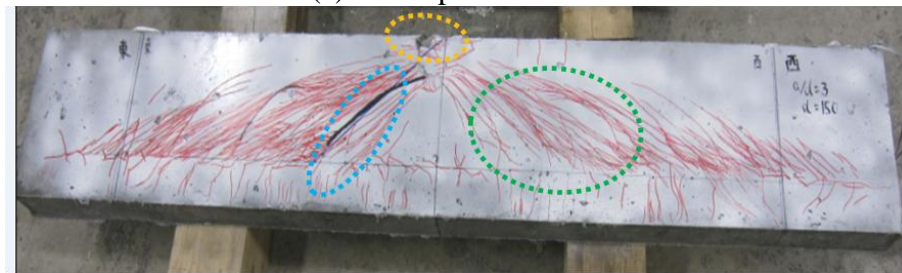


Figure 3.6 Crack distribution during test for case 3-100

Figure 3.7 shows the crack pattern at the end of experiment for case 2-50 and case 3-50. Compared with the crack pattern at the end of test for case 2-100 and 3-100 as shown in Figure 3.5(e) and 3.6(e), it can be confirmed that all the specimens are failure in diagonal shear, and show similar crack distribution pattern. For all the specimens, there are many multiple fine cracks in diagonal shear directions (marked as green line), and some multiple fine cracks localize in diagonal shear direction in each specimen (marked as blue line), and collapse near loading plate (marked as yellow line) are also observed. This behavior is different from normal concrete beam.



(a) Crack pattern for case 2-50



(b) Crack pattern for case 3-50

Figure 3.7 Crack distribution of the specimen at the end of test

Figure 3.8 shows the measurement of crack spacing of one specimen between multiple fine cracks in the middle shear span. Based on this measurement, the crack spacing between multiple fine cracks are investigated, and the crack spacing between multiple fine cracks is about 3mm.

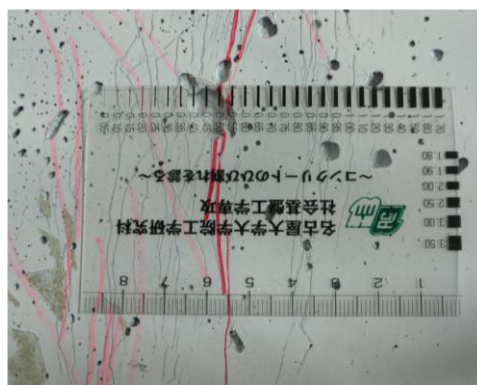


Figure 3.8 Crack spacing of multiple fine cracks in the middle of shear span

3.3.3 Applicability of shear strength evaluation equations

3.3.3.1 Applicability of equation for normal concrete

Supposing the material of normal concrete under the same geometry of tested specimens, also assuming this normal concrete has the same compressive strength with UHP-SHCC as 91N/mm^2 , then the shear force (V) can be obtained, based on the evaluation equations for diagonal shear force (V_c) and shear compression force (V_u) proposed by Niwa (Niwa,1986)

$$V_c = 0.2 * f_c^{1/3} (100 * P_t)^{1/3} * \left(\frac{1000}{d}\right)^{1/4} * \left(0.75 + 1.4 * \frac{d}{a}\right) * b * d \quad (3.1)$$

$$V_u = \frac{0.244 * f_c^{2/3} * \{1 + (100P_t)^{1/2}\} * \left(1 + 3.33 * \frac{r}{d}\right)}{1 + \left(\frac{a}{d}\right)^2} * b * d \quad (3.2)$$

Where f_c : compression strength (N/mm^2)
 P_t : longitudinal tension reinforcement ratio
 b : width (mm)
 d : effective height (mm)
 a : length of shear span (mm)
 r : plate width (mm)

According to the shear force V_c for diagonal shear failure and shear force V_u for shear compression failure, shear strength τ_c and τ_u can be obtained respectively, defined as shear force dividing section area, then the shear strength (τ_s) can be obtained.

Table 3.3 shows the τ_c , τ_u and τ_s for normal concrete as well as shear strength (τ_{test}). Based on table 3.3, the shear strength obtained from experiment are much larger than those for normal concrete cases. All of the normal concrete cases are expected by shear compression failure even if having the same compressive strength with UHP-SHCC as 91 N/mm^2 . However, all the specimens of UHP-SHCC beams are failed in diagonal shear observed from experiment. It can be confirmed that shear behavior of UHP-SHCC beams is different from that of normal concrete beams.

Table 3.3 Shear strength of normal concrete and tested specimen

case	τ_c (N/mm ²)	τ_u (N/mm ²)	τ_s (N/mm ²)	τ_{test} (N/mm ²)
a/d=2 b=100	3.1	5.9	5.9	9.8
a/d=2 b=50	4.0	7.5	7.5	11.6
a/d=3 b=100	2.64	3.0	3.0	7.0
a/d=3 b=50	3.32	3.7	3.7	8.3

3.3.3.2 Applicability of equation for UHPFRC

Supposing the material of ultra high performance fiber reinforced concrete (UHPFRC) under the same geometry of tested specimens, then the designed shear strength can be obtained based on eq.(3.3) to eq.(3.12) (JSCE, Recommendations for design and construction of ultra high performance fiber reinforced cement composites with multiple fine cracks (UHPFRCC), 2004).

$$V_{yd} = V_{rpcd} + V_{fd} + V_{ped} \quad (3.3)$$

$$V_{ped} = P \sin \alpha_p / \gamma_b \quad (3.4)$$

α_p : angle of longitudinal prestressing to the member axis

P_{ed} : effective tensile force in longitudinal prestressing steel

γ_b : 1.1 in general

V_{ped} : component of effective tensile force in longitudinal prestressing steel parallel to the shear force

$$\beta_a = 0.7 + 1.67/(a/d)^{1.1} \quad (3.5)$$

$$\beta_d = \sqrt[4.5]{1000/d} \quad (3.6)$$

$$\beta_p = \sqrt[5]{(100 * p_t)/6} \quad (3.7)$$

$$\beta_{pc} = \sqrt[3.5]{1/(\tan(\beta_{up}))} \quad (3.8)$$

$$\beta_{up} = \frac{1}{2} \tan^{-1} \left(\frac{2\tau}{\sigma'_{xu} - \sigma'_{yu}} \right) \quad (3.9)$$

$$V_{fd} = (f_{vd} / \tan \beta_u) * b_w * z / \gamma_b \quad (3.10)$$

V_{fd} : design shear capacity of reinforcing fiber

f_{vd} : design tensile yield strength of UHPFRC (N/mm²)

a : shear span length (mm)

d : effective depth

P_t : reinforcement ratio

γ_b : 1.3 in general

b_w : width of member (mm)

σ'_{xu} , σ'_{yu} : average compressive stress in axial direction and direction perpendicular to axial direction

$$\beta_u = \frac{1}{2} \tan^{-1} \left(\frac{2\tau}{\sigma'_{xu} - \sigma'_{yu}} \right) - \beta_0 \quad (3.11)$$

$$V_{rpcd} = 0.18 \sqrt{f'_{cd}} * \beta_a * \beta_d * \beta_p * \beta_{pc} * b_w * d / \gamma_b \quad (3.12)$$

f'_{cd} : design compression strength of UHPFRC (N/mm²)

V_{rpcd} : design shear capacity of a linear member excluding the strength exerted by reinforcing fiber.

Table 3.4 shows the shear strength of the four geometries evaluated by the equation for UHPFRC, compared with the shear strength (τ_{test}) of UHP-SHCC obtained from experiment. Shear strength is defined by shear forces (V_{yd}) dividing section area. The compression strength is assumed as 91N/mm², and the tensile strength of 6.7N/mm² is assumed to this UHPFRCC. The β_u is assumed as 40° and 30°. $\beta_u=40^\circ$ is recommended value in the specification, and $\beta_u=30^\circ$ is appropriate angle observed from test, shown in Figure 3.5 and 3.6.

Based on Table 3.4, the shear strength calculated from evaluation equation with $\beta_u=30^\circ$ is larger than that with $\beta_u=40^\circ$, also larger than shear strength from test. Under the condition of $a/d=2$, the difference of shear strength between the evaluation equation with $\beta_u=40^\circ$ and experiment are small, about 6%. However, under the condition of $a/d=3$, the shear strength of tested specimens are reduced more than 18%, compared with evaluation equation with $\beta_u=40^\circ$.

Table 3.4 Shear strength of UHPFRC and tested specimen

case	Shear strength (N/mm ²)		
	τ_{yd}		τ_{test}
	$\beta_u=40^0$	$\beta_u=30^0$	
a/d=2 b=100	10.4	13.5	9.8
a/d=2 b=50	10.9	14.1	11.6
a/d=3 b=100	9.7	12.9	7.0
a/d=3 b=50	10.2	13.3	8.3

3.4. Investigation on fracture surface of UHP-SHCC beam failed in shear

As discussed above, the shear behavior of UHP-SHCC beams is quite different from that of normal concrete beams. Hence, the deep investigation is required. The crack surface can be expressed by asperity height and angle for crack surface physically (Tanabe, 2004), which is described later.

As well-known, the crack surface has much effect for shear stress transfer. For example, if crack width larger than the asperity height for normal concrete (usually half of aggregate size), there is no shear stress transfer between cracks for normal concrete. Especially, UHP-SHCC is a new material with special material properties of hardening strain as well as high tensile and compressive strength. Therefore, investigation on shape of fracture surface of UHP-SHCC is very important, which can be contributed to understand shear stress transfer behavior for UHP-SHCC beams. Therefore, investigation on shape of fracture surface of UHP-SHCC beams failed in shear is conducted.

3.4.1 Surveying on fracture surface of UHP-SHCC beam in shear failure

3.4.1.1 Fracture surface of UHP-SHCC beam in shear failure

Figure 3.9 shows fracture surface of UHP-SHCC beam in shear failure and fracture surface of normal concrete (Chupanit and Roesler, 2008). It can be seen the area near loading point for UHP-SHCC beam is collapsed (marked as yellow line area in Figure 3.7), and most of other area is very smooth (marked as blue line area in Figure 3.7). However, the fracture surface for normal concrete is quite rough (Tanabe, 2004). Hence, the fracture surface of UHP-SHCC beam is different from that of normal concrete. In order to understand shear failure of UHP-SHCC deeply, the fracture surface of failed UHP-SHCC beam is surveyed.

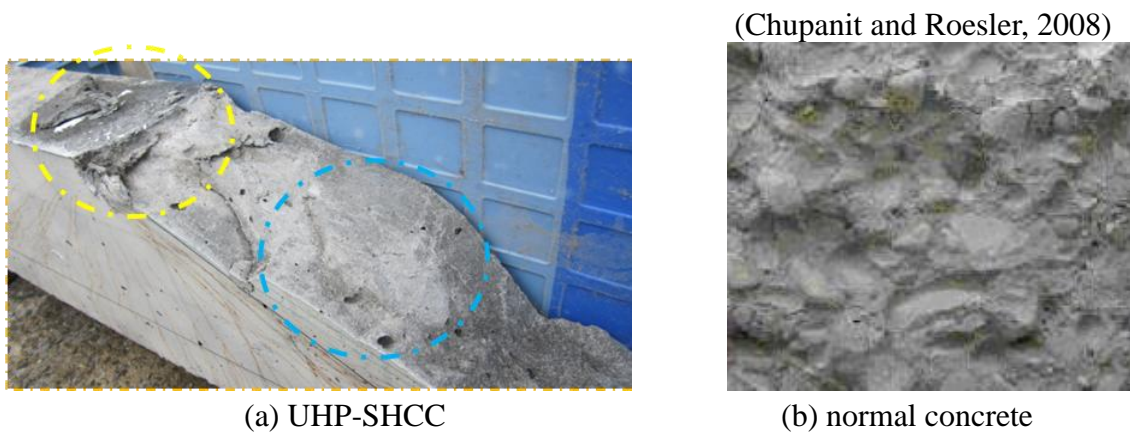


Figure3.9 Fracture surface of UHP-SHCC and normal concrete

3.4.1.2 Surveying method for investigating fracture surface

In this investigation on fracture surface of UHP-SHCC beam in shear failure, the method using laser displacement meter is adopted. This laser displacement meter has an accuracy of $1\mu\text{m}$. Figure 3.10 shows an example of arrangement of measurement using laser displacement meter (KHOA, 2012), this example is using laser displacement meter for measuring the surface deformation with the specimen size of $150*150$, the two dotted red line marked in Figure 3.10 is the measured direction.



Figure3.10 Example of surface deformation measurement

3.4.2 Sample and procedures for investigating fracture surface

Figure 3.11 shows one sample for investigating fracture surface, and the sketch for measuring the roughness. The sample for investigation is obtained from one of the tested specimens, including part of the fracture surface. The position of this sample is near the loading point, especially the coarse area of this sample as marked in Figure 3.11, and the loading direction in experiment has been marked in Figure 3.11. The

length of this sample in longitudinal direction is 125mm, and the measured length is 123mm, due to the starting position for measurement has the distance of 2mm from the side, which has been marked as green line in Figure 3.11. The surface area of this sample is measured along the six dotted red line (marked in Figure 3.11) using laser displacement meter. In the process of measuring roughness of this sample, 6 series of the roughness (line 1 to line 6) along the 6 dotted red lines is obtained.

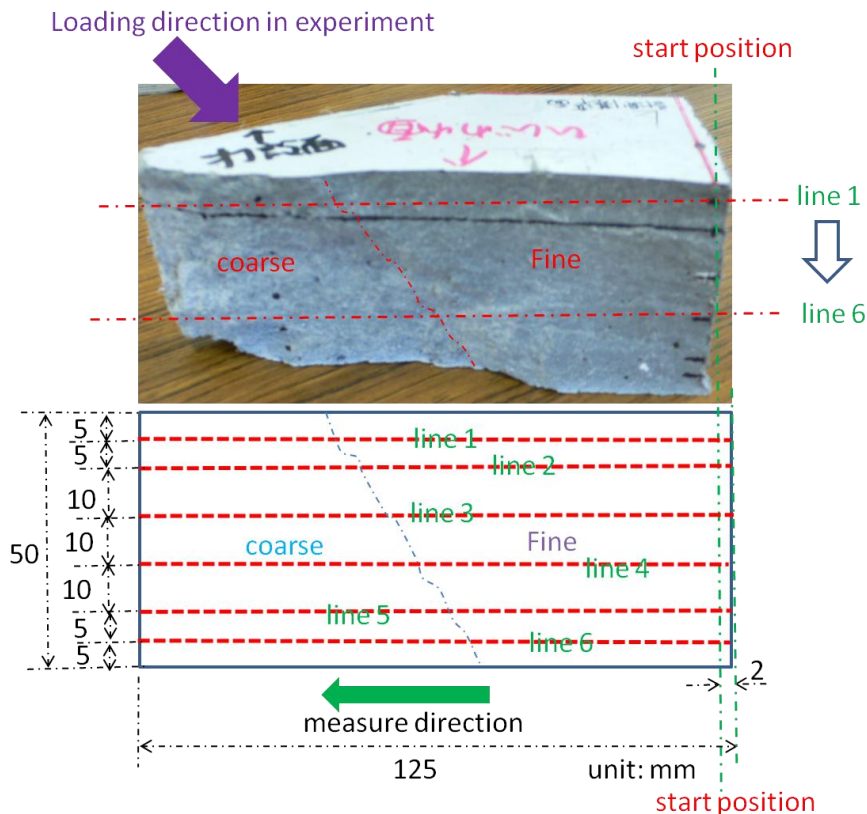


Figure 3.11 Fracture surface of UHP-SHCC beam in shear failure

3.4.3 Result of investigation on fracture surface of UHP-SHCC beam

As mentioned before, the crack surface can be expressed by the asperity height and angle. Using the laser displacement meter, the roughness of crack surface can be obtained. This roughness is the height of fracture surface along the measured line due to peak and down in fracture surface. Based on the measured roughness, the asperity height and angle can be obtained. Then the crack surface can be described physically. As shown in Figure 3.14, there is an assumed crack surface for UHP-SHCC, with the asperity height of 1.2mm and angle of 15°.

Figure 3.12 shows the test data for the roughness for the six series along the positions of 6 selected dotted lines (shown in Figure 3.11) in longitudinal direction. The

longitudinal length in Figure 3.12 means the 125mm as marked in Figure 3.11, and position of longitudinal length of 0mm is corresponding to the position of start point as marked in Figure 3.11.

Based on these test results, the roughness of fracture surface can be seen. It can be easily illustrated that the roughness change of every series along the measured length is serrated, with many peak-down phenomena, and the roughness in coarse area is obviously larger than that in fine area.

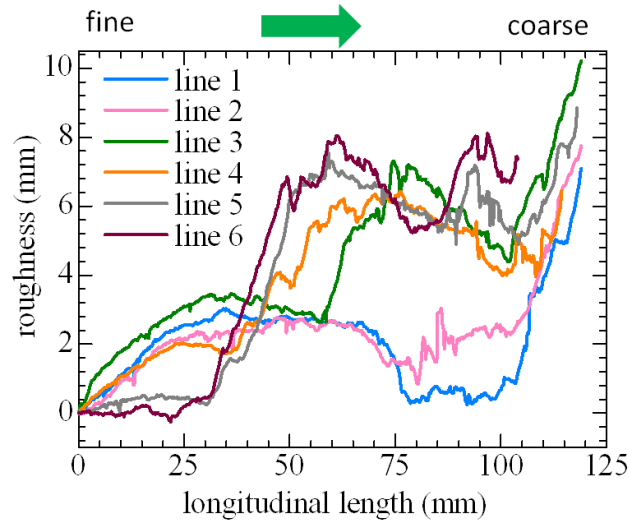


Figure 3.12 Roughness of fracture surface

However, the roughness change of fine area and coarse area of the surface can't be recognized from Figure 3.12. Therefore, Figure 3.13 shows the revised test data of the roughness for the six measured series. These revised data comes from one simple assumption, which assumes the start position in fine area and the end position in coarse area have the same roughness change of 0mm.

Figure 3.13 illustrates the roughness change for coarse area is much steeper than that in fine area. As mentioned before, using the asperity height and angle of the crack surface, the crack surface can be expressed physically. There are some investigations on crack surfaces for other concrete materials. Normal concrete is considered as half of aggregate size for asperity height and angle of 50° (Tanabe, 2004), high strength concrete is considered as asperity height of 2.5mm and angle of 35° (Kongkeo, 2005). However, the crack surface of UHP-SHCC is very smooth, which is not easy to decide the asperity height and angle. Therefore, the idea of average asperity height and angle for the peak and down area is considered. Based on this concept, the angle and asperity height are measured, and then the angle and asperity height are considered as 15° and 1.2mm. Figure 3.14 shows series 2 and 3 for fracture surface, with the same scale of

roughness in vertical direction and longitudinal length in longitudinal direction, which can show the real shape of crack surface, not like different scales in Figure 3.12 and 3.13. Moreover, the assumed crack surface with angle of 15° and asperity height of 1.2mm is used to fit for series 2 and 3, it can be seen that this assumed crack surface has a good fitting with the real fracture surface of UHP-SHCC.

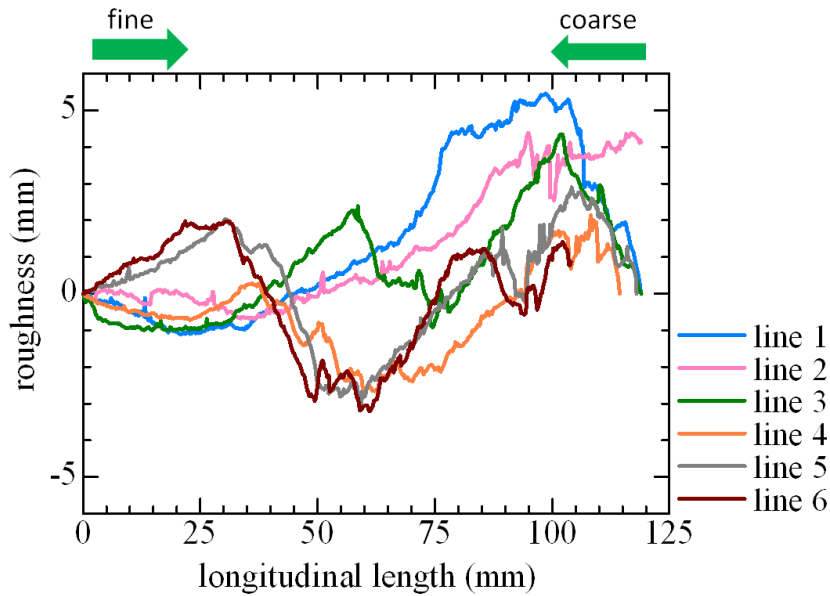
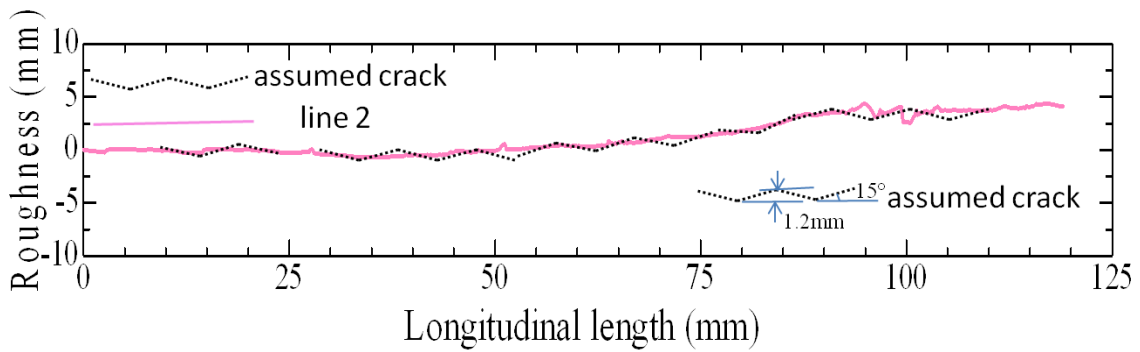
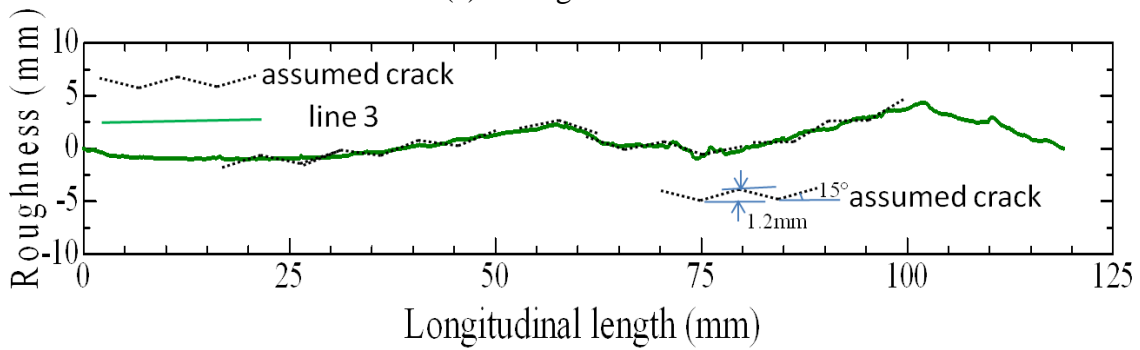


Figure3.13 Revised roughness of fracture surface



(a) Fitting for line 2



(a) Fitting for line 3

Figure3.14 Assumed crack used to fit for crack shape of UHP-SHCC material

3.5. Summary and conclusions

UHP-SHCC beams with $a/d=2$ and $a/d=3$ are tested in order to clarify the shear behavior of UHP-SHCC beams. UHP-SHCC has special feature compared with other construction materials.

(1) The tested UHP-SHCC beams are all failed in diagonal shear. Specimens with a/d of 2 have larger load carrying capacities than those of specimens with a/d of 3. However, specimens with a/d of 3 have larger displacements than those of specimens with a/d of 2. Loads drop suddenly after reaching the peak load capacity for specimens with a/d of 2, but loads decrease smoothly for specimens with a/d of 3.

(2) That is, all the tested specimens of UHP-SHCC shows similar crack propagation behavior. Flexural multi-fine cracks occur firstly. Then multiple fine cracks occur in the middle of shear span. The number of multiple fine cracks increases with the increasing of load level, and multiple fine cracks in shear direction play dominant role gradually. Thereafter, some multiple fine cracks localize until peak load, and then the specimen fractured in shear failure. Due to the ultra high performance of UHP-SHCC, the area near loading point is collapsed.

(3) The shear strength obtained from test is compared with shear strength evaluation equation for normal concrete and for ultra high performance fiber reinforced concrete (UHPC). The equation for normal concrete underestimate and the equation for UHPC overestimate the shear strength of UHP-SHCC. It is difficult to evaluate the shear strength by the evaluation equation proposed in the past.

(4) Using the laser displacement meter, the roughness of fracture surface can be obtained. The investigated fracture surface of UHP-SHCC in shear failure confirmed the smooth of fracture surface. Based on the idea of average asperity height and angle, the asperity height and angle of UHP-SHCC are decided as 1.2mm and 15° by measurement including the peak and down area. This decision is verified by the assumed crack surface (according to the decision) used for fitting the real fracture surface of UHP-SHCC material.

CHAPTER 4

ANALITICAL EVALUATION OF SHEAR FAILURE OF ULTRA HIGH PERFORMANCE OF STRAIN HARDENING CEMENTITIOUS COMPOSITE BEAMS

4.1. Introduction

As mentioned in previous chapter, it is necessary to accurately evaluate the shear capacity of the structures in design when UHP-SHCC is used as structural member, in which shape, structural detail and boundary condition become more complicated. In order to evaluate the mechanical behavior of the structures, finite element analysis is strongly useful for predicting not only the load carrying capacity but also the stiffness and post peak behavior. Therefore, the method to predict the shear behavior of UHP-SHCC beam is required.

Lately, some researchers have tried to develop constitutive model for fiber reinforced concrete such as SHCC. Yonezawa et al. has proposed the analytical method to simulate HPFRCC (High Performance Fiber Reinforced Cementitious Composite) beam by focusing the characteristics of tensile and shear behavior of the material (Yonezawa, 2009). They assumed that tensile stress-strain relationship obtained from uni-axial tensile test was introduced in constitutive model directly and there was no shear stress transfer on the crack surface. They could simulate the shear behavior of HPFRCC beam well by using their proposed model. Although the load-displacement relationship obtained from the analysis can show good agreement with that of the test, there is no consideration of the characteristics of cracking behavior of HPFRCC material such as multiple cracking behavior and fiber contribution. On the other hand, Suryanto et al. have proposed the constitutive model of R/ECC (Reinforced Engineered Cementitious Composite) and simulated the pure shear behavior of R/ECC panels (Suryanto, 2010). They also used tensile stress-strain relationship obtained from uni-axial tensile test directly. By considering the feature of crack surface of ECC, they proposed the shear stress transfer model of ECC. In this model, shear strength on the crack surface of ECC was 25% compared with normal concrete and fiber contribution was introduced in shear softening region. They could simulate the behavior of R/ECC panel not only shear stress-strain relationship but also the changing of principal direction during testing. Their model was suitable to simulate the shear behavior of R/ECC panel. Although the both model described above are reasonable for evaluate their own objectives, the applicability of their models for other SHCC materials is not clear because there is no physical meaning in the model, such as characteristics of crack surface with asperity and angle discussed in chapter 3, which can be used for expressing crack surface directly for

SHCC materials by measurement.

In this chapter, shear stress transfer model of UHP-SHCC is proposed considering roughness of crack surface, crack distribution behavior and fiber contributions for shear resistance. In the proposed model, the roughness of crack surface such as incline and irregularity of crack in micro-scope level is considered as parameters with asperity height and angle and introduced in numerical model. The crack distribution behavior, which is related with multiple cracks and localized crack, is introduced in the evaluation of crack width for the shear stress transfer. Besides, the effectiveness of bridging forces from fiber on shear resistance is also considered. Finally, shear failure behavior of UHP-SHCC beams is investigated numerically by using the proposed model and the influence of the each parameter on the behavior is discussed.

4.2. Analytical Method

4.2.1 Overview of Lattice Equivalent Continuum Model (LECOM)

In this study, Lattice Equivalent Continuum Model (LECOM) developed by Itoh et al. was used as constitutive model of concrete (Itoh et al., 2004). This model is one of the fixed smeared crack models and consists of combination of tension, compression and shear lattices which are modeling of force flows in concrete element, as shown in Figure 4.1.

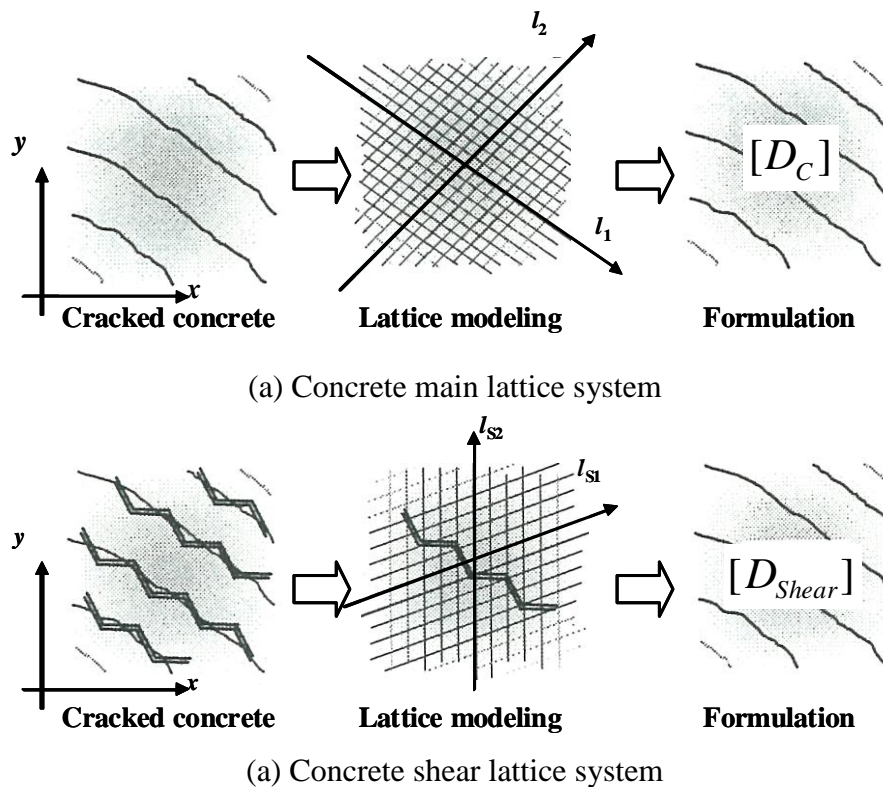


Figure 4.1 Diagram of lattice equivalent continuum model (Itoh et al., 2004)

When principal stress exceeds tensile strength of concrete, crack occurs in an element and concrete main lattice system is defined along the principal stress coordinate system. This lattice system is fixed unless principal stress in following loading stage exceeds tensile strength again. Here, concrete shear lattice system is defined depending of the concrete main lattice system as explained later. Stresses are calculated in each lattice systems, in which uni-axial stress-strain relationships are assumed considering the material properties.

4.2.2 Uni-axial stress-strain relationship under tension and compression

Stress- strain relationship of concrete under tension was modeled as tri-linear curve, as described in Chapter 2. Figure 4.2(a) shows the tensile stress-strain relationship of UHP-SHCC. Stress increases until cracking stress linearly. After cracking, strain hardening behavior was modeled as similar with test result until peak stress. After peak stress, stress decreases linearly indicating the ultimate strain, which was defined by the fracture energy in order to avoid element size dependency. On the other hand, stress-strain relationship under compression was modeled as shown in Figure 4.2(b). Saenz equation was used up to the compressive strength and a linear softening branch was assumed. The slope of linear softening branch was defined by considering the compression fracture energy (G_{fc}) in order to avoid problem element size dependency as well as tensile behavior (Nakamura and Higai, 2001).

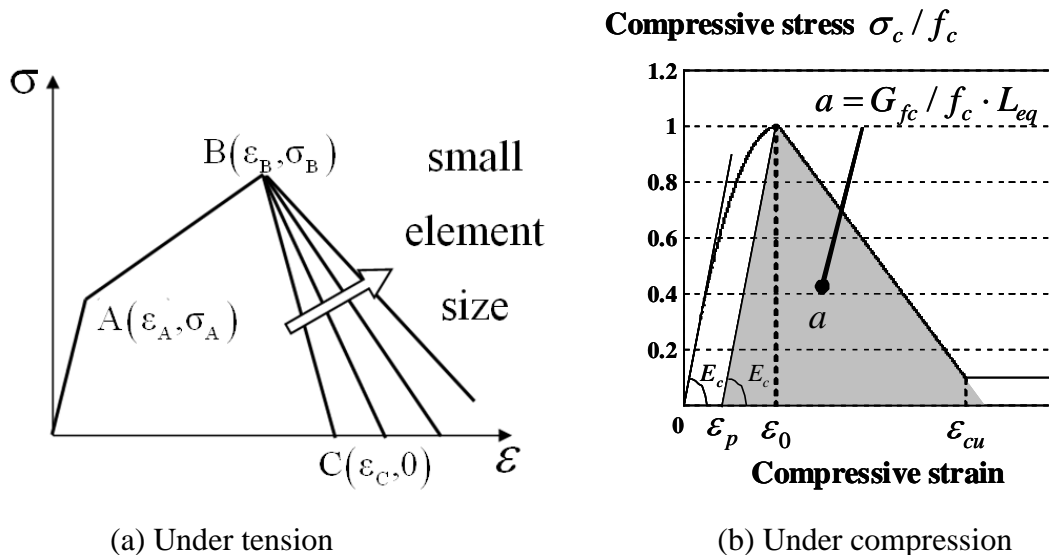


Figure 4.2 Schematics of uni-axial stress-strain relationship

4.2.3 Shear stress transfer model of normal and high strength concrete

Shear stress transfer mechanism along cracked surface is influenced by roughness of cracked surface, crack width and shear deformation. Taking into account of these degree of incidences is important in the analysis of RC structures, because each factor has a complicated influence to each other. Itoh et al. proposed a shear stress transfer model for normal concrete by mechanism from view point of cracked surface, shear deformation and aggregate interlocking action depending on crack width along cracked surface, which is assumed boldly as shown in Figure 4.3 (Itoh et. al., 2004). The major characteristic of the shear stress transfer model is the use of parameters, which express the shape of assuming cracked surface by the angle (θ) and the asperity height (H) of cracked surface directly. From the point of shape of crack surface, recommendation values for θ and H are 50° and $0.5G_{\max}$ (G_{\max} is size of coarse aggregate), respectively.

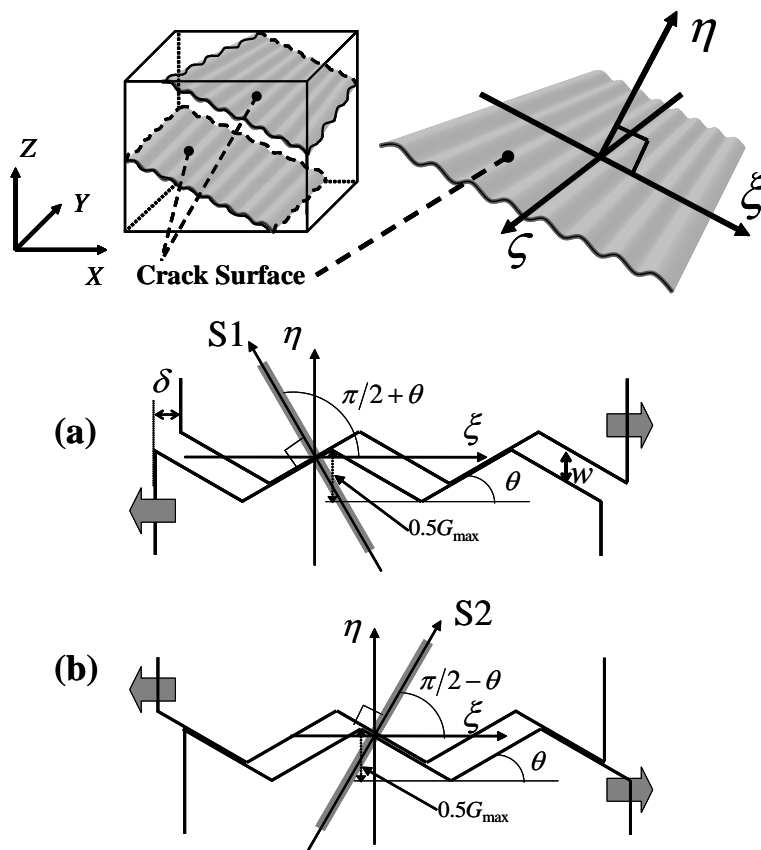


Figure 4.3 Modeling of cracked surface (Itoh et al., 2004)

On the other hand, for high strength concrete, it is well known that crack surfaces

become smoother, because the strength of cement matrix is higher than that of coarse aggregate and crack propagates straightly. Based on this investigation, Kongkeo et al. revised the shear stress transfer model in order to apply to high strength concrete (Kongkeo et al., 2005). Based on result of shear stress-shear slip displacement curves, they found shear slip displacement in high strength concrete is larger than the normal one, and the degradation of shear stiffness in high strength concrete is also observed compared with normal concrete. However, increasing of shear slip displacement can be evaluated by decreasing the angle. Furthermore, the degradation of shear stiffness can be evaluated by decreasing of the asperity height. Therefore, based on the calculation, they proposed that θ is 35° and H is 2.5mm for high strength concrete, as shown in Figure 4.4. They could predict reasonably the shear capacity of high strength concrete beams failed in diagonal shear failure by using the proposed model.

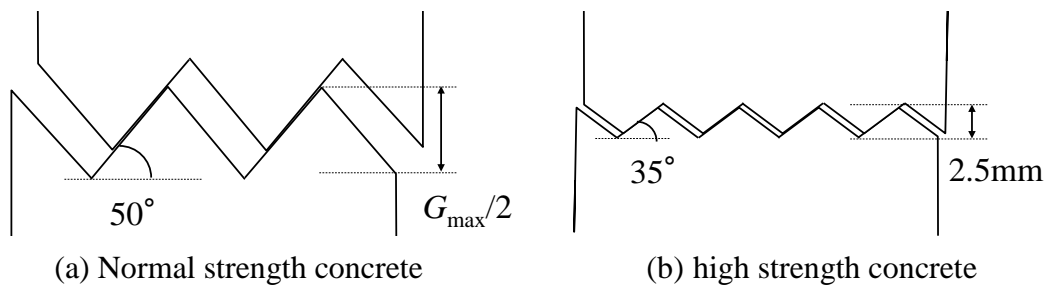


Figure 4.4 Parameter of crack in constitutive model

The shear stress in shear lattice direction occurred by the contact of cracked surface and calculated by uni-axis stress-strain relationship. Contact stress-strain relationship was defined by shear strut stiffness E_{sh} and yield stress f_s as shown in Figure 4.5. Initial value of E_{sh} is assumed as the same with the elastic modulus of concrete.

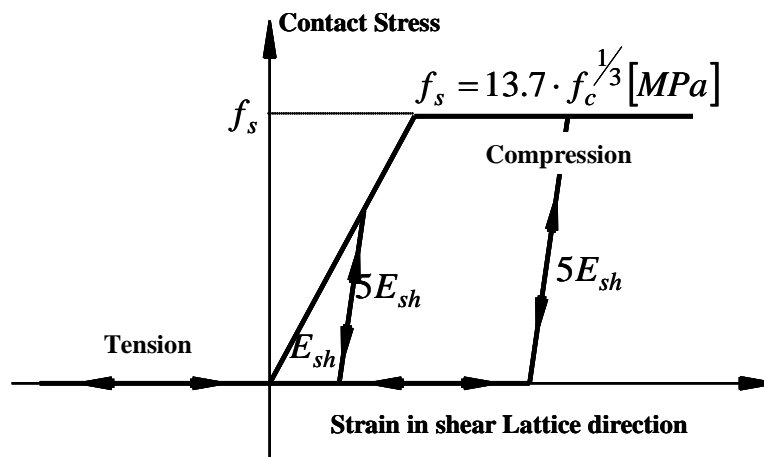


Figure 4.5 Uni-axial stress-strain relationship in shear lattice (Itoh et al., 2004)

As shown in Figure 4.6, crack width has effect on the contact area. In this shear stress transfer model, two influences due to crack opening are considered, decreasing of contact area and shear strut stiffness. Contact area was decreased linearly with an increasing of crack width and when crack width exceeded the asperity height (H) contact area became zero, that is, no shear stress transfer. On the other hand, shear strut stiffness was decreased according to a relationship as shown in Figure 4.7. These relationships were obtained from parametric analyses for pure shear test of normal and high strength concrete (Kongkeo et al., 2005).

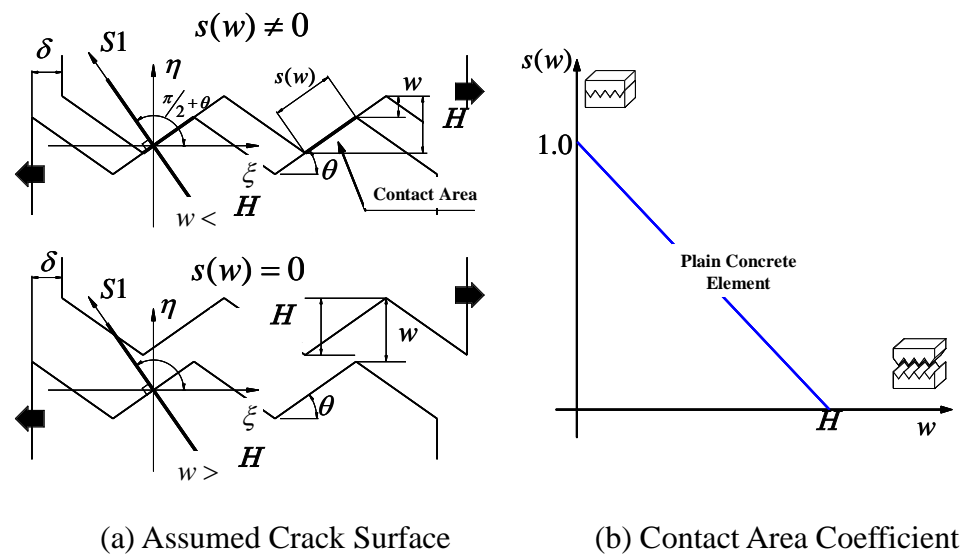


Figure 4.6 Assumption of the contact area (Kongkeo et al., 2005)

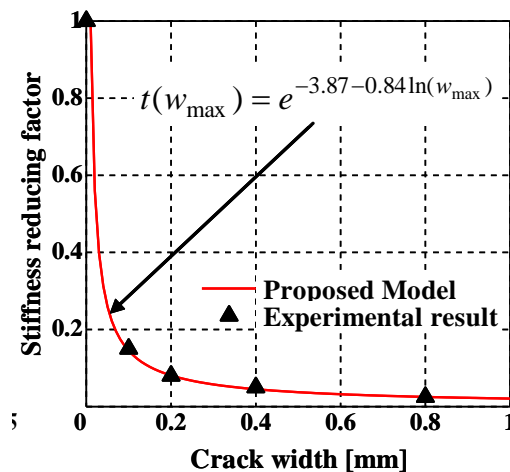


Figure 4.7 Stiffness Reducing Factor relating with crack width (Kongkeo et al., 2005)

4.2.4 Modeling of rebar and bond properties

Rebars were modeled discretely by truss elements. Stress-strain relationship assumed in truss element was a bi-linear curve with strain hardening, as shown in Figure 4.8. When the stress in rebar reaches the yield strength f_y the initial modulus of elasticity E_s is reduced and the modulus of elasticity on the hardening branch, E_{sh} , was set to $0.01E_s$.

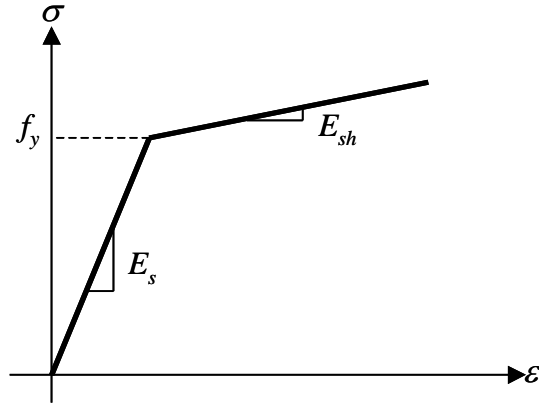


Figure 4.8 Stress-strain relationship of rebar

Bond property between rebar and concrete was modeled by link element connecting rebar and concrete elements. Bond stress-slip relationship introduced in link element is represented by Eq.(4-1), in which the relationship proposed by Suga et. al. was assumed until peak stress (Suga et. al., 2001) and linear softening behavior was assumed after peak stress, as shown in Figure 4.9. This bond property between rebar and concrete was applied to RC members in chapter 6 and 7, without using this chapter.

$$\tau = \begin{cases} 0.4 \times 0.9 \times (f'_c)^{2/3} (1 - \exp(-40(s/D)^{0.5})) & 0 \leq s \leq s_1 \\ \tau_{\max} - (\tau_{\max} - 0.1\tau_{\max}) \frac{(s - s_1)}{(s_2 - s_1)} & s_1 \leq s \leq s_2 \\ 0.1\tau_{\max} & s_2 \leq s \end{cases} \quad (4-1)$$

Where, τ and s are bond stress and slip, respectively. τ_{\max} is bond strength which corresponds to bond stress at 0.2 mm slip. D is diameter of rebar (unit: mm).

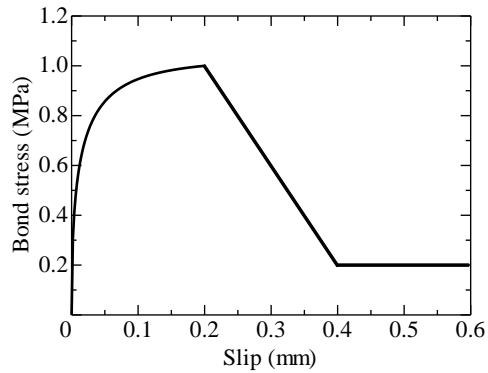
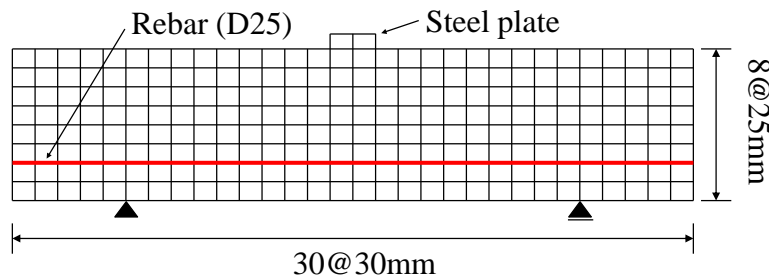


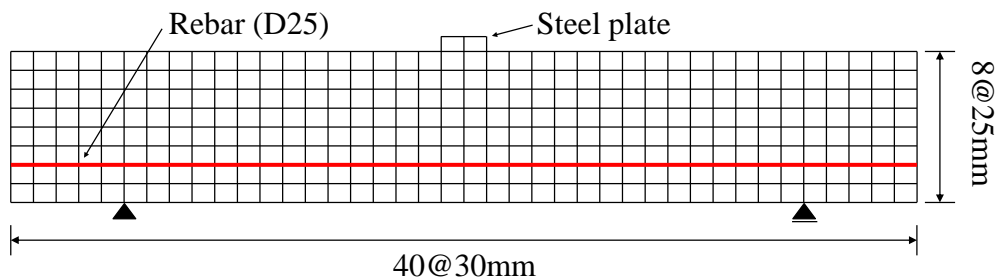
Figure 4.9 Bond stress-slip relationship

4.3 Analytical model

Figure 4.10 shows the numerical models for the UHP-SHCC beams with 50 mm width, 3.37 % of longitudinal reinforcement ratio, and $a/d = 2$ and 3 described in previous chapter. The mesh size of the model was 30mm in longitudinal direction and 25mm in vertical direction. Rebar was model as consist of truss elements. Since bond property between rebar and UHP-SHCC was significantly strong based on experimental investigation, due to silica fume was adopted in mix proportion, perfect bond was assumed in this analysis. Boundary condition was set as simple beam and incremental displacement was applied at the center of loading plate.



(a) Numerical model of specimen for $a/d = 2$



(b) Numerical model of specimen for $a/d = 3$

Figure 4.10 Numerical model

Material property of the UHP-SHCC is summarized in Table 4-1. Initial cracking stress and tensile of ultimate strength are set to 4.15 and 5.33 N/mm², respectively, based on uniaxial stress-strain curves shown in Figure 3.2. Strain at lower limit of ultimate tensile strength is 0.85% and fracture energy 1.80N/mm, obtained from experiment is considered in softening region. Compressive strength and strain corresponding to it are set to 91.0N/mm² and -0.004, respectively. Compressive fracture energy is assumed 83.9 N/mm.

Table 4.1 Material property of UHP-SHCC

Material	Unit	Value
Young's Modules	GPa	29.0
Initial cracking stress	N/mm ²	4.15
lower limit of ultimate strength	N/mm ²	5.33
Strain at peak stress	-	0.85%
Fracture Energy	N/mm	1.80
Compressive strength	N/mm ²	91.0
Strain at compressive strength	-	-0.004
Compressive Fracture Energy	N/mm	83.9

Moreover, the strain at higher ultimate strength (6.4 N/mm²) is 1.85% and fracture energy 3.0N/mm, obtained from experiment is also considered in softening region, in order to evaluate the influence from ultimate tensile strength.

4.4 Analytical simulation of Shear failure behavior of UHP-SHCC beam by shear stress transfer model for high strength concrete

Figure 4.11 shows the load-displacement relationship of analytical results for $a/d = 2$ and 3 cases. In the analysis, shear stress transfer model for UHP-SHCC is adopted, that is θ was 15° and H was 1.2mm (obtained from measurement). Moreover, shear stress transfer model for high strength concrete is adopted, that is θ was 35° and H was 2.5mm (proposed by Kongkeo et al.). In the figures, black line with marks shows experimental result and red line shows analytical result. Moreover, theoretical flexural stiffness for elastic beams is also drawn by dotted line.

The initial stiffness of analytical results are slightly higher than the experimental ones, however they are the same with the theoretical flexural stiffness. It is clearly shown that shear capacities obtained from analyses were underestimated for both lower and higher ultimate strength cases with $\theta = 15^\circ$ and $H = 1.2\text{mm}$ (crack surface corresponding to UHP-SHCC). For $\theta = 35^\circ$ and $H = 2.5\text{mm}$ cases (crack surface corresponding to high strength concrete), the shear capacities for higher tensile strength is not so much different from experimental ones. However, the assumed crack surface is rougher than

UHP-SHCC. Especially, brittle failure behavior occurs after peak load for all the cases, which is different from experiment. Therefore, the former shear stress transfer model is not applicable to simulate the shear failure behavior of UHP-SHCC beam and it is necessary to develop a shear stress transfer model for simulating the behavior of UHP-SHCC beam.

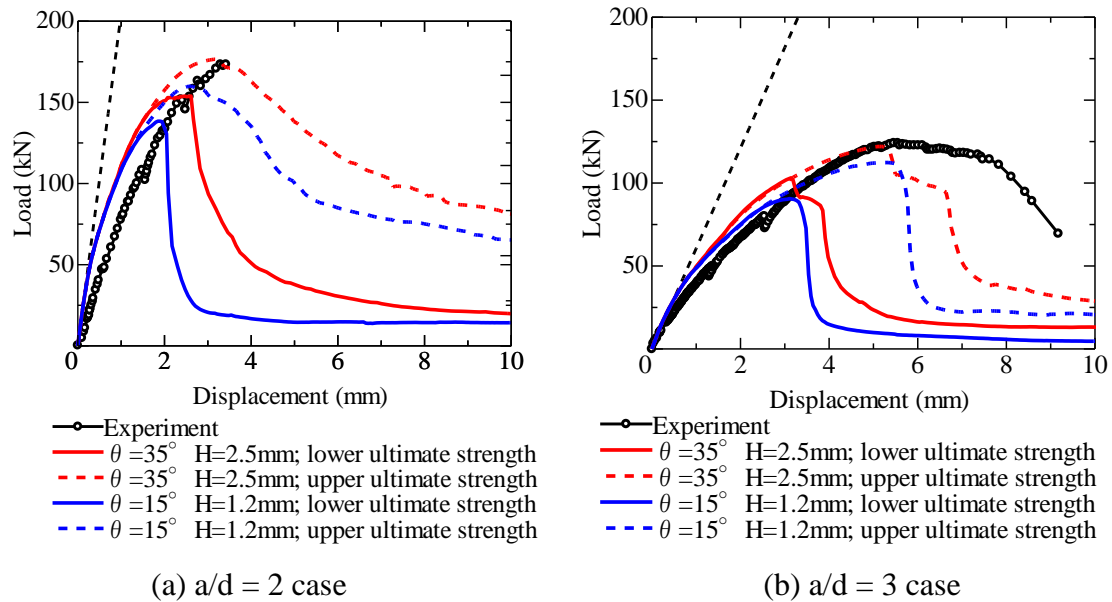


Figure 4.11 Load-displacement curves

4.5 Development of shear stress transfer model of UHP-SHCC

In order to develop the shear stress transfer model of UHP-SHCC, following 3 phenomena are considered in this study. One is shape of crack surface, second is cracking behavior of multiple fine cracks and third is contribution of fiber for shear stress transfer.

4.5.1 Consideration of roughness of crack surface of UHP-SHCC

Firstly, the influence of shape of crack surface is investigated. From the investigation in previous chapter, the shape of the crack surface of UHP-SHCC are obviously different from that of supposed in the shear stress transfer model for high strength concrete because UHP-SHCC is not concrete but one of mortars and constituent material in UHP-SHCC is quite different from concrete, that is there is no coarse aggregate and only quartz is included as an aggregate. The parameters for crack surface were measured by laser displacement meter, with 15° and 1.2mm for θ and H respectively.

Figure 4.11 shows the analytical result in which θ is 15° and H is 1.2mm. As shown

in figures, the shear capacity decreased and post peak behavior also changed to be more brittle. It is because the shear stress transfer becomes small when θ decreased and contact area becomes zero soon for small H . This result also indicated that shear capacity of UHP-SHCC can't be predicted by the same manner with concrete and other considerations are required.

4.5.2 Consideration of crack distribution behavior

As described before, crack width is one of the important parameter for shear stress transfer. In LECOM, 1 crack is assumed in 1 element in the estimation of crack width. However, Cracking in UHP-SHCC under tension is explained as follows: multiple cracking until peak stress and localization of one of the multiple cracks after peak stress. Therefore, this cracking behavior is modeled in the estimation of crack width in the constitutive model. In the model, number of crack is assumed to be saturated and constant from the first cracking even though multiple cracks actually occur in sequence. Thus, crack width of UHP-SHCC, w_c , was modeled by Eq. (4-1), as shown in Figure 4.12.

$$w_c = \begin{cases} 0 & \varepsilon < \varepsilon_A \\ (\varepsilon - \varepsilon_A) \cdot l_c & \varepsilon_A \leq \varepsilon \leq \varepsilon_B \\ (\varepsilon_B - \varepsilon_A) \cdot l_c + (\varepsilon - \varepsilon_B) \cdot L_{elem} & \varepsilon > \varepsilon_B \end{cases} \quad (4-2)$$

Where, ε is strain and ε_A and ε_B are corresponding to the strain drawn in Figure 4.12. l_c is crack spacing. In the Eq. (4-2), the crack width in the range of $\varepsilon_A < \varepsilon < \varepsilon_B$, is defined by the width of a crack of multiple cracks, and in the range of $\varepsilon > \varepsilon_B$, the crack width is for a localized crack developed from one of multiple cracks. In this study, crack spacing, l_c , of UHP-SHCC used in experiment was assumed as 3 mm based on the crack pattern obtained by uni-axial tensile test.

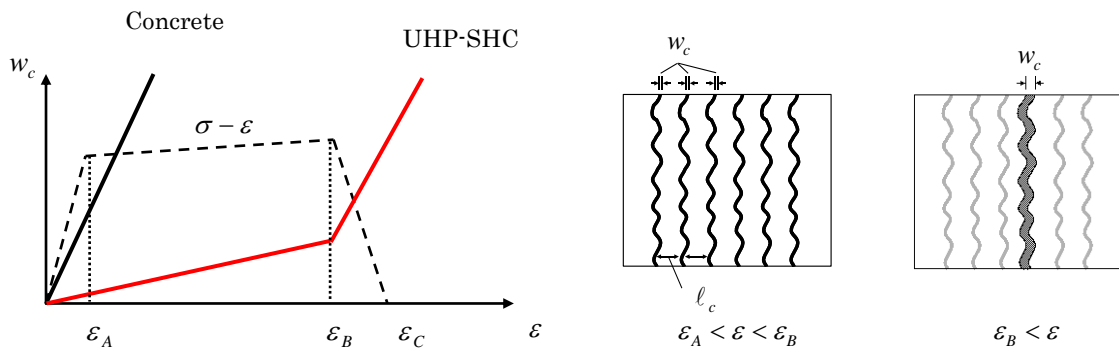


Figure 4.12 Relationship between crack width and strain

Figure 4.13 shows the load-displacement relationships which are considered multiple cracking in the estimation of crack width. Although the multiple cracks were modeled in the analysis, mechanical behavior did not change from without considering multiple cracking and shear capacity was still underestimated. Figure 4.14 shows crack patterns for lower limit of ultimate strength cases, which are at pre peak, peak and post peak region, obtained from the analysis considering multiple cracking. In the figure, red and blue color show multiple cracks and localized cracks, respectively. As shown in figure, diagonal cracks localized at the peak load, that is, the ability of shear stress transfer decreased at instant. It is confirmed that the localization of crack is the reason of shear failure. From these analyses, it is not enough to simulate the shear behavior of UHP-SHCC beam by considering the shape of crack surface and multiple cracking in the shear stress transfer model.

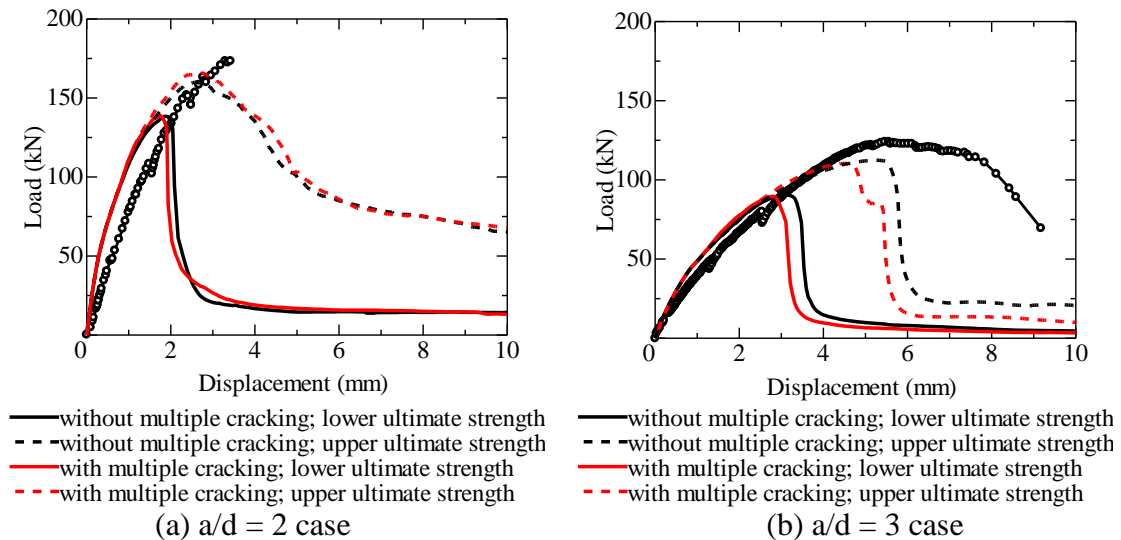


Figure 4.13 Effect of crack width by considering multiple cracking

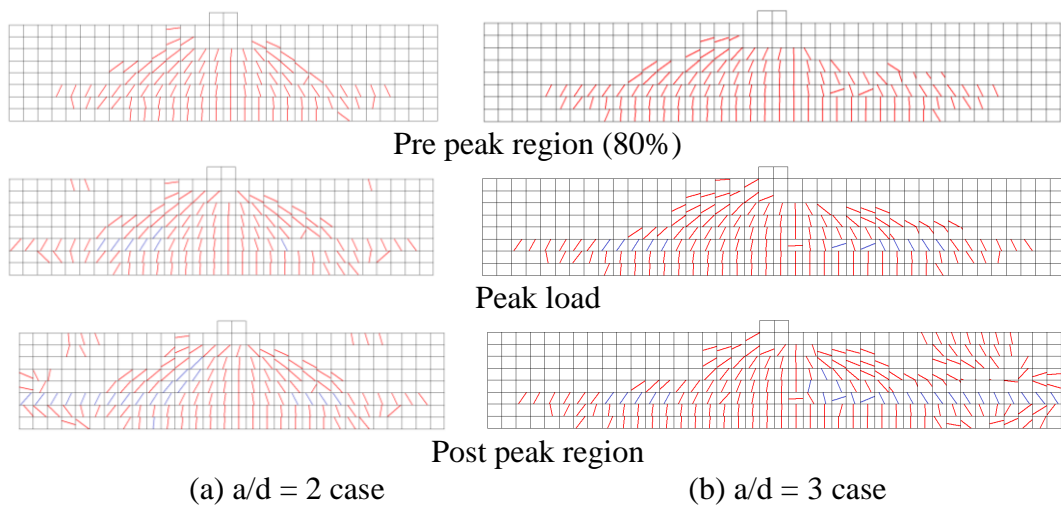


Figure 4.14 Crack pattern (Red: multiple cracks, Blue: Localized cracks)

4.5.3 Consideration of fiber contribution for shear stress transfer

When shear deformation occurs along the crack surface of UHP-SHCC, bridging forces of the fiber in the material are expected to have an ability of resistance. Fiber contribution against the shear stress transfer is considered in the shear transfer model. Figure 4.15 shows the outline of the fiber effects on the crack surface. In Figure 4.15, the contact stress in compression area (σ_{s1}) is already adopted in former shear stress transfer model, which can be seen from modeling of cracked surface in Figure 4.3. In proposed model, tensile stress along the perpendicular direction of the inclined plane of crack surface due to fibers, fiber bridging stress (σ_{s2}), is considered as well as contact stress in concrete shear lattice system. The contact stresses are shown in Eq. (4-3).

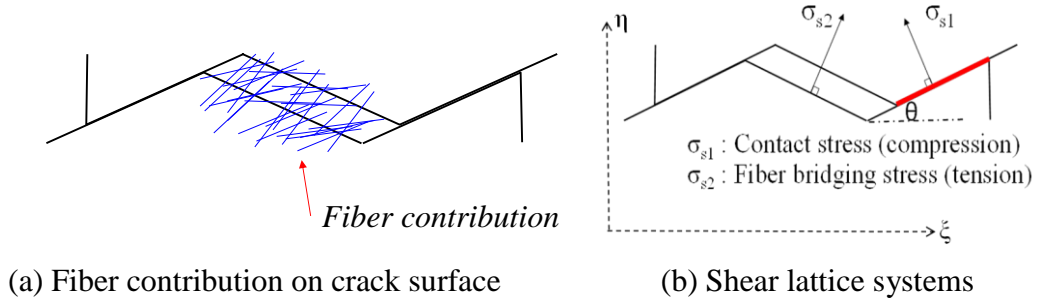


Figure 4.15 Outline of the fiber contribution on the crack surface

$$\Delta \begin{Bmatrix} \sigma_{s1} \\ \sigma_{s2} \end{Bmatrix} = \begin{bmatrix} E_{s1} & 0 \\ 0 & E_{s2} \end{bmatrix} [T_{\varepsilon, s1, s2}] \Delta \{ \varepsilon_{lcr} \} \quad (4-3)$$

Where, $\Delta \{ \varepsilon_{lcr} \}$ is strain field in local coordinate system(ξ, η), $[T_{\varepsilon, s1, s2}]$ is strain rotation matrix which is used to rotate the incremental local strain into direction of contact stress (σ_{s1} and σ_{s2}), E_{si} is gradient of equivalent uni-axial stress-strain relationship that is denoted by $\partial \sigma_{si} / \partial \varepsilon_{si}$.

Here, stress-strain relationships in tension region of shear lattice are assumed as shown in Figure 4.16 in order to evaluate the influence on shear capacity of UHP-SHCC beams. Elastic modulus of fiber contribution, E^* (E_{s2} in equation (4-3)), in stress-strain relationship is assumed as Eq. (4-4).

$$E^* = (V_f)^{\frac{2}{3}} \cdot E_f \quad (4-4)$$

Where V_f is fiber contents of UHP-SHCC and E_f is elastic modulus of fiber itself, in this study, PE fiber with 88000 N/mm² was used. Since tensile failure of UHP-SHCC is depending on the pullout of the fiber at the localized crack, maximum fiber bridging stress in shear lattice, defined as fiber bridging strength in this study, was depending on

the bond strength of fiber and UHP-SHCC. In order to investigate the influence of the fiber bridging strength on the mechanical behavior of UHP-SHCC beams, 3 different fiber bridging strength, f_{fiber} were assumed and set to 1.0, 3.0 and 6.0 N/mm², respectively.

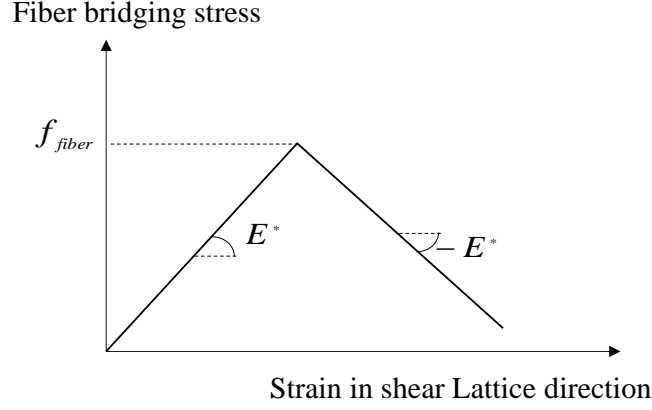


Figure 4.16 Fiber bridging stress-strain relationship

The contact stresses (σ_{s1} and σ_{s2}) can be rotated to local stress field by stress rotation matrix $[T_{\sigma,s1,s2}]^{-1}$. Therefore, the incremental local stress can be calculated by Eq. (4-5).

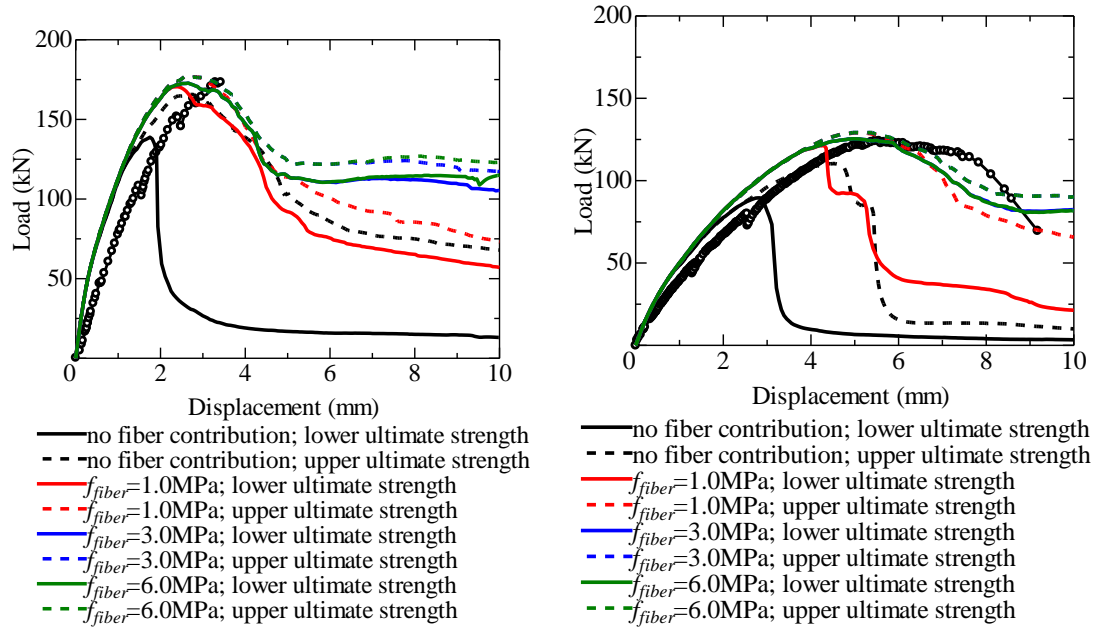
$$\Delta\{\sigma_l\} = \Delta\begin{Bmatrix} 0 \\ \sigma_n \\ \gamma_{\xi\eta} \end{Bmatrix} = [\Omega][T_{\sigma,s1,s2}]^{-1} \Delta\begin{Bmatrix} \sigma_{s1} \\ \sigma_{s2} \end{Bmatrix} \quad (4-5)$$

Where, $[\Omega]$ is controlling matrix to neglect the influence of tensile stress in direction of ξ .

Finally, incremental local stress $\Delta\{\sigma_l\}$ obtained from Eq. (4-5) is rotated again to the structural coordinate system(X, Y).

Figure 4.17 shows load-displacement relationships of each fiber bridging strength cases and no fiber contribution case. As shown in figures, shear capacities are increased with fiber contribution and come close to experimental results. When the fiber bridging strength increases, the shear capacities also increase and post peak behavior becomes more ductile. Besides, the shear capacities are almost the same with $f_{fiber} = 3.0$ N/mm² and $f_{fiber} = 6.0$ N/mm² for lower and higher ultimate strength cases. Especially, for the case of $f_{fiber} = 1.0$ N/mm², brittle failure occurred and it is similar with no fiber contribution case. For the cases of $f_{fiber} = 3.0$ and 6.0 N/mm², softening branches are more gently comparing with the case of $f_{fiber} = 1.0$ N/mm². Moreover, for the cases of $f_{fiber} = 3.0$ and 6.0 N/mm², no significant difference appears in each other even if the ultimate tensile strengths are different, such as lower and higher ultimate strength cases. These results indicate that the failure mode of the case of $f_{fiber} = 1.0$ N/mm² and

$f_{fiber}=3.0$ and 6.0 N/mm² were different, and fiber bridging contribution has much effect for shear stress transfer behavior, which should be considered.



(a) $a/d = 2$ case

(b) $a/d = 3$ case

Figure 4.17 Effect of fiber contribution for shear stress transfer

Figure 4.18 and 4.19 show the crack patterns in both pre and post peak region and deformations in post peak regions for lower limit of ultimate strength cases. In the figures, red and blue color lines represent multiple crack and localized crack, respectively. From the crack pattern, it is shown that for each case, localized cracks start to occur in pre peak region. In post peak region, localized cracks propagated in the web of shear span. However, for the cases of $f_{fiber} = 1.0$ N/mm², diagonal cracks opened along the rebar and these deformations are different from other cases, in which shear deformations of an element near loading plate is dominant. These results indicate that if the fiber contribution is small, failure mode tends to become diagonal shear failure. On the other hand, if the fiber contribution is strong, failure mode tends to become shear compression failure. However, the differences of shear capacities between 2 failure mode are not so large for both $a/d = 2$ and 3 cases. Note that, as the investigated in previous chapter, both specimens failed in diagonal shear failure.

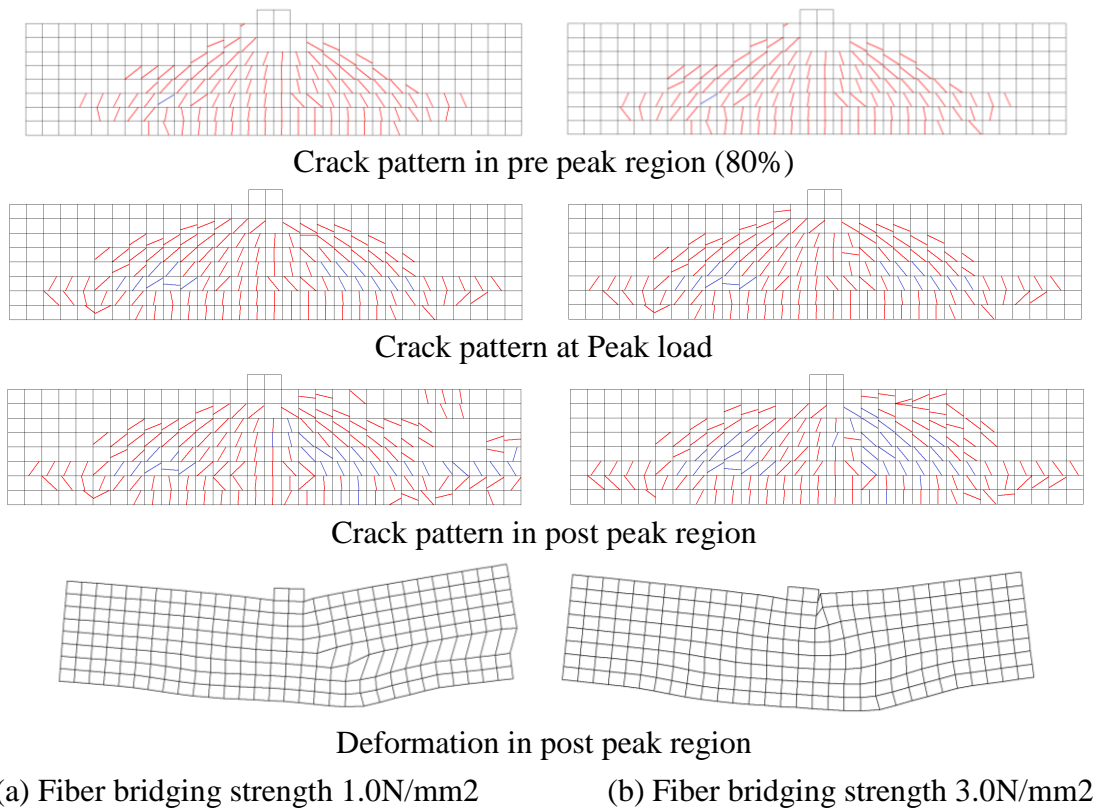


Figure 4.18 Crack pattern and deformation (a/d= 2.0 case)
 (Red: multiple cracks, Blue: Localized cracks)

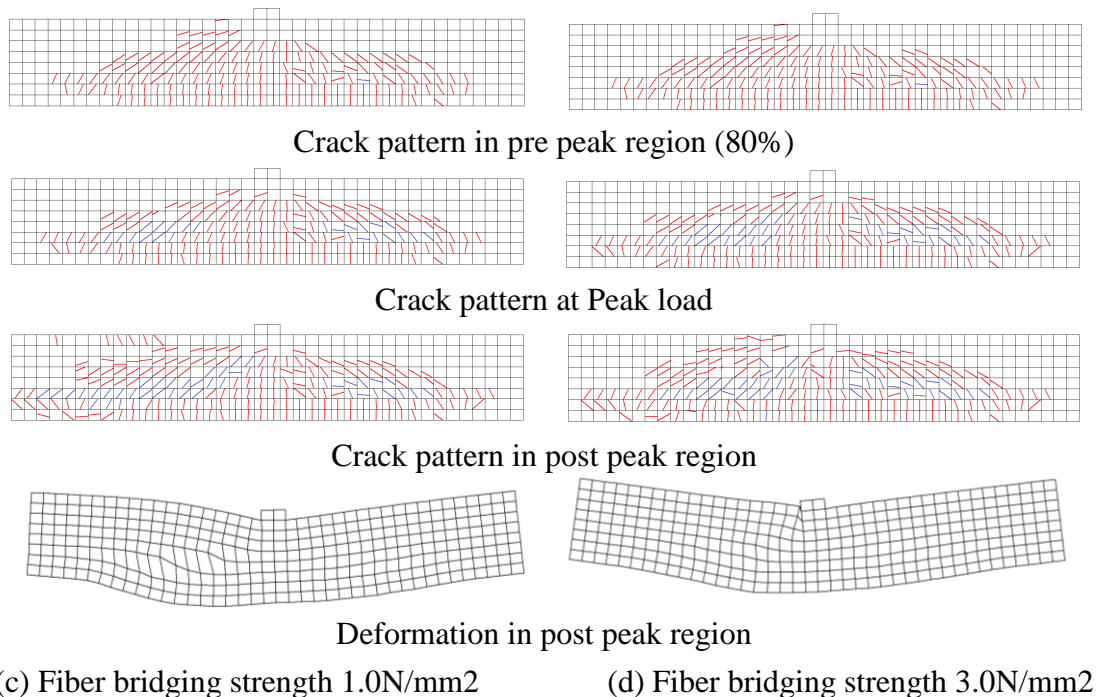


Figure 4.19 Crack pattern and deformation (a/d= 3.0 case)
 (Red: multiple cracks, Blue: Localized cracks)

Figure 4.20 shows the analytical results for the specimens $a/d = 2$ and 3 cases with 100mm width and 1.69% of longitudinal reinforcement ratio. In the figure, theoretical flexural stiffness for elastic beams is also drawn by dotted line. The initial stiffness of the analyses is higher than that of the experiment. However, the initial stiffness of the analyses is the same with that of theoretical calculation. Therefore, it is thought that the experimental results were affected by some reasons. Concerning the shear capacities, analytical results obtained from proposed model with any fiber bridging contribution (f_{fiber}) could evaluate the shear capacities for both cases. However post peak behavior of the case of $f_{fiber} = 1.0\text{ N/mm}^2$ for both $a/d = 2$ and 3 show brittle failure comparing with the case of $f_{fiber} = 3.0$ and 6.0 N/mm^2 . It is also indicated that the failure mode is depended on fiber bridging contribution (f_{fiber}). In the experiment, sudden failure occurred in both $a/d = 2$ and 3 for the width 100mm case. Therefore, it was suggested that fiber bridging contribution (f_{fiber}), was not so large in shear failure of UHP-SHCC beams. Based on the experimental investigation on pullout behavior of single fiber in UHP-SHCC material, it is supposed that when the direction of pullout of fiber changes from the perpendicular to parallel to the crack surface, fiber bridging stress decreased. However, in the proposed model, it is assumed that fiber bridging contribution (f_{fiber}), keeps constant value during analysis even if the shear deformation becomes large. Therefore, in order to evaluate the shear behavior more accurately, it is required that the influence of the decreasing of fiber bridging strength on the shear stress transfer is introduced into proposed model. From the above discussion, the strength of fiber bridging effect is necessary to investigate more in detail. However, it is shown that proposed shear stress transfer model is applicable to the UHP-SHCC beam failed in shear.

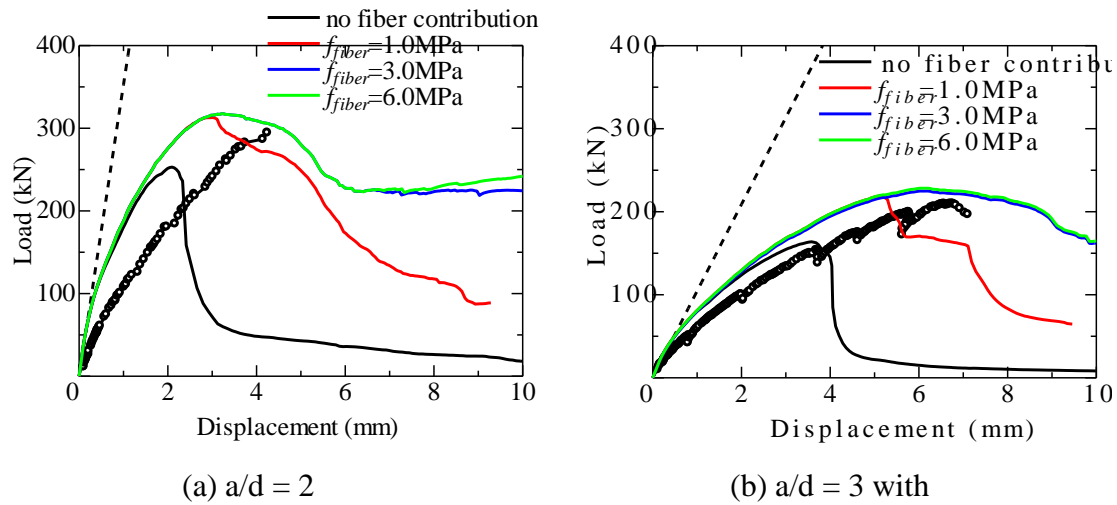


Figure 4.20 Validation of proposed model for other specimens with 100mm width and 1.69 % of longitudinal reinforcement ratio

4.6 Conclusion

In this chapter, shear stress transfer model of UHP-SHCC are developed based on the geometry of cracks and failure mechanism and the applicability of proposed model was discussed. The following conclusions were obtained.

- (1) Shear stress transfer model was an important factor in order to simulate the shear failure behavior of UHP-SHCC beam by finite element analysis and the shear stress transfer model of high strength concrete was inadequate.
- (2) Shear stress transfer model of UHP-SHCC was developed by considering 3 phenomena, that is, the roughness of crack surface, crack distribution behavior and fiber contribution for shear resistance. Among the 3 phenomenon, fiber contributions had much effect on predicting the shear failure behavior of UHP-SHCC.
- (3) Fiber bridging strength defined as the maximum fiber bridging stress in concrete shear lattice systems is one of the most important parameter for simulating the shear failure behavior such as shear capacity and failure mode. In this study, the failure mode changed from diagonal shear failure to shear compression failure by increasing the fiber bridging strength. Since fiber bridging strength might be decreased depending on the pullout direction, it is required that the influence of this effect is considered in proposed shear stress transfer model in order to evaluate the shear behavior of UHP-SHCC beams failed in diagonal shear.

CHAPTER 5

EXPERIMENTAL INVESTIGATION ON FLEXURAL BEHAVIOR OF RC BEAM STRENGTHENED BY UHP-SHCC

5.1. Introduction

It is well-known that the advantage of high ductility of UHP-SHCC obtained by uniaxial tensile test is reduced by the effect of an existing crack within the substrate in repair or strengthening application (Kamal et al., 2008; Kamal, 2008). This is the reason that the crack distribution within UHP-SHCC is limited near the existing crack in RC structure as shown in Figure 5.1. Zero-span tensile test to assess crack opening performance of UHP-SHCC is recommended to evaluate this behavior (Kunieda, 2006; Kamal et al., 2008; Kamal, 2008), which is model the condition near the crack in substrate with zero span between steel plate.

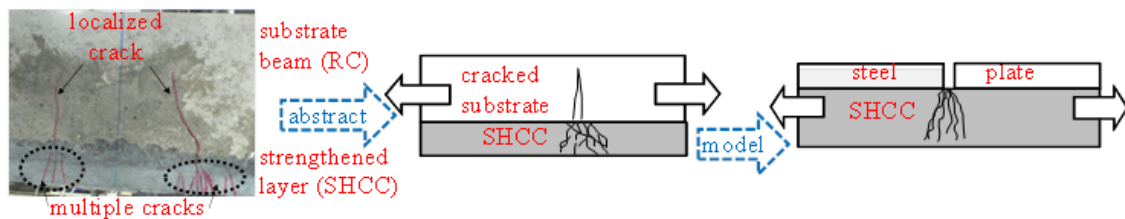


Figure 5.1 Concept of the zero-span tensile test

Kamal tested RC beam strengthened by UHP-SHCC layer at tensile part with the thickness of 30mm, 50mm and 70mm (Kamal, 2008). Based on his experiment, Kamal discussed the strengthening effect of RC beam with UHP-SHCC on the load carrying capacity and initial stiffness of the strengthened beam, which are increased with the increasing of thickness of UHP-SHCC. Moreover, the equivalent strengthening effect between RC substrate beam strengthened by UHP-SHCC layer with different thickness and RC layer with different reinforcement ratio is discussed. Also, the distributed fine cracks in UHP-SHCC were observed.

In this chapter, RC substrate beam strengthened by UHP-SHCC material with the thickness of 10mm, 30mm and 50mm is carried out. This experiment is focus on the flexural behavior of strengthened RC beam by UHP-SHCC layer with different thicknesses, especially concerning the crack propagation behavior of multiple fine cracks in UHP-SHCC layer. Based on this experiment, the crack propagation behavior of multiple fine cracks in UHP-SHCC is investigated.

5.2 Experimental Procedure

5.2.1 Geometry of RC beams strengthened by UHP-SHCC material

Figure 5.2 shows the geometry of the specimens used for the experiment of RC

beams (substrate beams) strengthened by UHP-SHCC layer. Four RC beams with length of 1200mm and cross section of 100 x 150mm are prepared. Two deformed bars with diameter of 10mm are arranged as longitudinal bar and stirrups with diameter of 6mm are arranged in the shear span to prevent shear failure. One of these RC beams is used as control beam, and the left three beams are strengthened by UHP-SHCC layer with the thickness of 10mm, 30mm, and 50mm are named as U-10, U-30 and U-50 respectively. Retarder is brushed at the bottom of frame before cast RC beams. RC beams are demoulded 2 days later after casting, and the bottom surface of the beams, which is the interface between the strengthening layer and the substrate, is washed out using a retarder to obtain a rough surface. After that, strengthening layers are casted at the bottom side of the substrate beams.

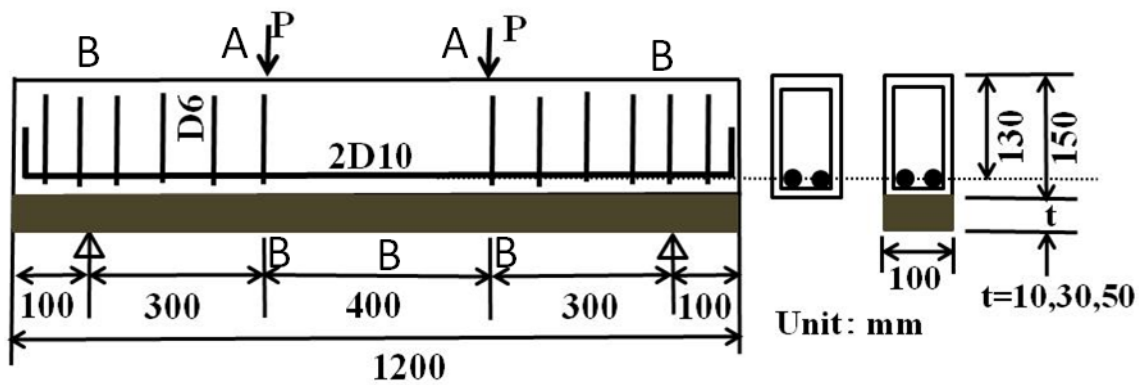


Figure 5.2 Geometry of specimens (unit: mm)

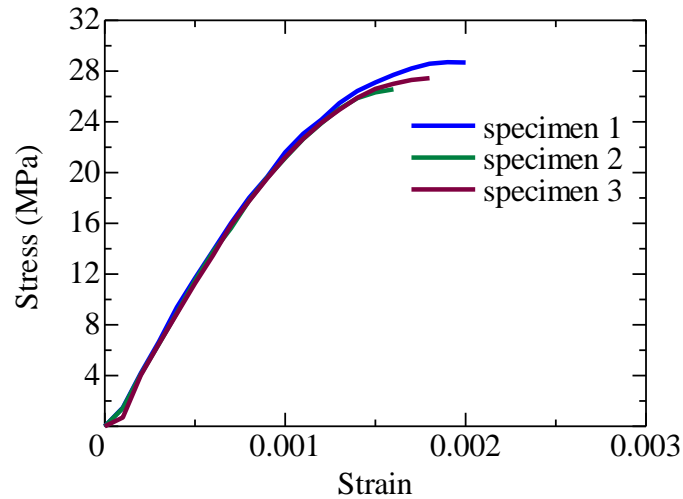
5.2.2 Materials

5.2.2.1 Ordinary concrete for substrate beams

The mixture proportion of ordinary concrete is shown in Table 5.1, and the water to cement ratio of ordinary concrete is 0.5. By conducting compressive test on 3 cylindrical specimens with the diameter of 100mm and height of 200mm, the compressive stress-strain curves of ordinary concrete are obtained, as shown in Figure 5.3. Based on this compressive stress-strain relationship, the average compressive strength and Young's modulus of this ordinary concrete are obtained as 27N/mm² and 23.5GPa respectively.

Table 5.1 Mixture proportion of concrete

W/C (%)	Unit content (kg/m ³)				
	Water	Cement	Sand	Aggregate	AE (liter/m ³)
50.0	166	332	765	973	1.328

**Figure 5.3** Stress versus strain from compression test

5.2.2.2 UHP-SHCC for strengthened material

UHP-SHCC is used as strengthening material in the series of strengthened RC beams with flexural failure, Table 5.2 shows the mixture proportion of UHP-SHCC used for specimens in this study. Water to binder ratio (W/B) is 0.22. Low heat Portland cement (density: 3.14g/cm³) is used, and 15% of the cement content is substituted for a silica fume (density: 2.2g/cm³). The quartz sand (less than 0.5mm in diameter, density: 2.68g/cm³) is used as the fine aggregate. High strength polyethylene (PE) fiber is chosen for UHP-SHCC and the fiber volume in the mix is 1.5%. The diameter and length of the PE fibers are 0.012mm and 6mm, respectively. Superplasticizer is used to enhance the workability of the matrixes.

Table 5.2 Mixture proportion of UHP-SHCC

W/B (%)	Unit content (kg/m ³)							
	Water	Cement	Silica fume	Fine sand	Expansion agent	PE fiber	Super-plasticizer	Air reducing agent
22	338.5	1267.9	230.8	153.9	40.0	14.6	15.4	0.06

Note: binder includes cement and silica fume

Figure 5.4 shows the stress-strain curves obtained from uniaxial tensile tests of dumbbell-shaped specimens, with the tested cross section of 13x30mm. All specimens exhibited significant strain hardening behavior but scattering result is shown, the strain is defined as elongation rate in measurement length of 100 mm. Crack occur when their stress reach initial tension strength with the value of 4.2N/mm² at point A in stress-strain curve, then strain hardening behavior occurred with propagation of multiple fine cracks until the ultimate tension strength at point B. The lower limit and upper limit of ultimate tensile strength at point B are 7N/mm² and 8N/mm², corresponding to the hardening strain with 1.5% and 2.2%. Thereafter, the stress decrease due to the localization of one of the multi-fine cracks.

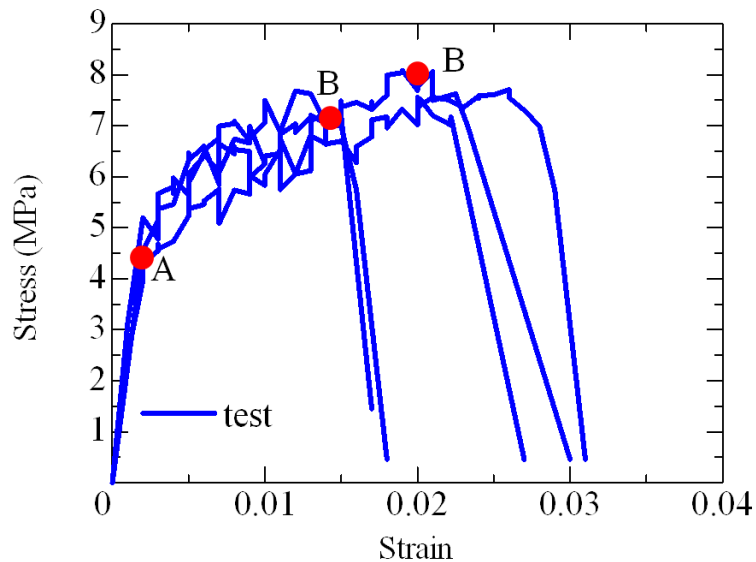


Figure 5.4 Results obtained from uniaxial tensile tests

By conducting compressive test on 3 cylindrical specimens with the diameter of 50mm and height of 100mm at the age of 28days, the stress-strain curves of UHP-SHCC material are obtained, as shown in Figure 5.5. Based on these stress-strain curves obtained from compressive test, the average compressive strength and Young's modulus of UHP-SHCC are 72N/mm² and 25GPa.

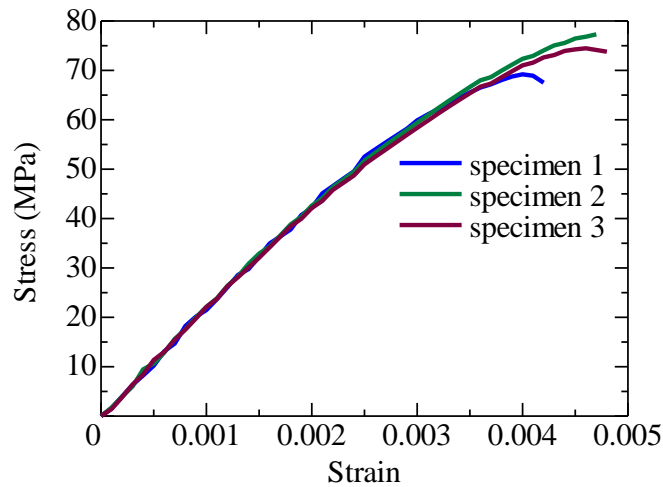


Figure 5.5 Stress versus strain from compression test

5.2.2.3 Reinforcements and stirrups

Deformed bar with diameter of 10mm are adopted as longitudinal bar, and the Young's modulus and yield strength are 200GPa and 345N/mm². Deformed bar with diameter of 6mm are adopted as stirrups, and the Young's modulus and yield strength are 200GPa and 295N/mm².

5.2.3 Setup and measurement method for the experiment

The tested specimens are loaded under four-point bending setup, as shown in Figure 5.6. In the experiment, displacements at loading points, support point and mid point are measured by displacement transducers, load is measured by load-cell, which are marked as Point B and A in Figure 5.2 respectively. The range of load cell is about 300kN, and the sensitivity of the load-cell is 0.1kN. The range of displacement transducers is 25mm with the sensitivity of 0.002mm. Under the condition of displacement larger than that value, the displacement transducers need to be adjusted during experiment.



Figure 5.6 Test setup of strengthened RC beam

5.3. Experimental results of RC beams strengthened by UHP-SHCC

5.3.1 Load-displacement relationships

Figure 5.7 shows the load-displacement curves obtained from the experiments for control beam (RC beam) and strengthened RC beams. The names of case U-10, U-30 and U-50 shown in Figure 5.7 represent RC beams strengthened by UHP-SHCC layer with the thickness of 10mm, 30mm and 50mm respectively. It can be clearly seen the load carrying capacities increase with the increasing of thickness of UHP-SHCC layers. The load carrying capacity of control beam is 40.8kN. Those for case U-10, U-30 and U-50 are 48.9kN, 55kN and 65.7kN respectively, which increase 16.5%, 34.8%, and 61.0%, compared with that of control beam.

For case U-10, the initial stiffness of load-displacement is larger than that of control beam, and the stiffness of load-displacement changes due to the yielding of reinforcement, but the load continues due to the load carrying capacity comes from UHP-SHCC layer. Thereafter, the load drops due to the loss of load carrying capacity of UHP-SHCC layer by localization of multiple fine cracks (first drop in load-displacement curve). Then the failure gradually occurs in the part of RC substrate beam.

For case U-30, the initial stiffness of load-displacement is larger than that of control beam and case U-10, and the stiffness of load-displacement is also changed due to the yielding of reinforcement, correspondingly, UHP-SHCC begins to carry load capacity, and load drops later due to localization of multiple fine cracks in UHP-SHCC layer (first drop in load-displacement curve).

For case U-50, the initial stiffness of load-displacement is larger than all of other cases, and the stiffness of load-displacement is also changed due to the yielding of reinforcement, correspondingly, UHP-SHCC begins to carry load capacity, and load drops later due to localization of multiple fine cracks in UHP-SHCC layer (first drop in load-displacement curve), this process is similar with case U-10 and U-30. However, as discussed above, case U-50 has largest load carrying capacity and the largest displacement at peak load.

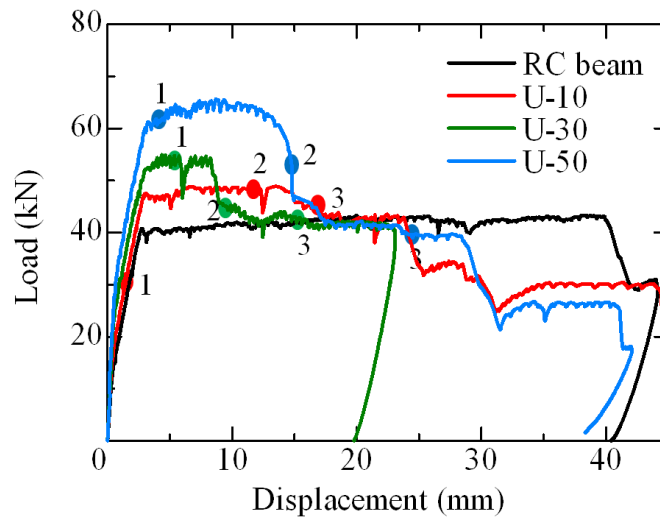


Figure 5.7 Load-displacement curves obtained from test

5.3.2 Crack propagation of the strengthened RC substrate beam

Figure 5.8 shows the crack patterns of control beam after failure. It can be clearly seen the control beam are failed in flexural failure.



Figure 5.8 Crack pattern of control beam at the end of experiment

Figure 5.9 shows the crack patterns of case U-10 at the position marked in load-displacement curve.

At point 1, there are two localized cracks in RC substrate beam part without multiple fine cracks in UHP-SHCC layer, which means stress of UHP-SHCC material in the strengthened layer has not reach the initial strength while cracks in RC substrate beam part is localized.

At point 2, zero-span behavior is dominant in this specimen, with many multiple fine cracks in UHP-SHCC layer adjacent to the every localized crack in RC substrate beam. Multiple fine cracks occur due to the occurrence of damage in UHP-SHCC layer caused by stress concentration from localized crack in RC control beam

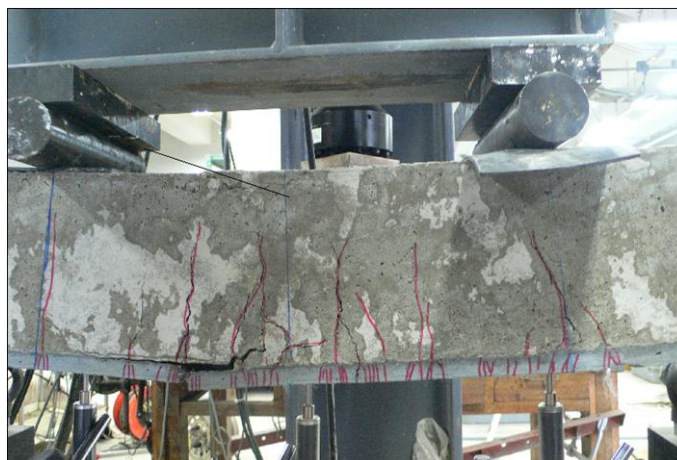
At point 3, some multiple fine cracks localize in UHP-SHCC layer, and UHP-SHCC layer loses load carrying capacity gradually. Thereafter, the debonding behavior occurs between UHP-SHCC layer and RC part.



(a) Point 1



(b) Point 2



(c) Point 3

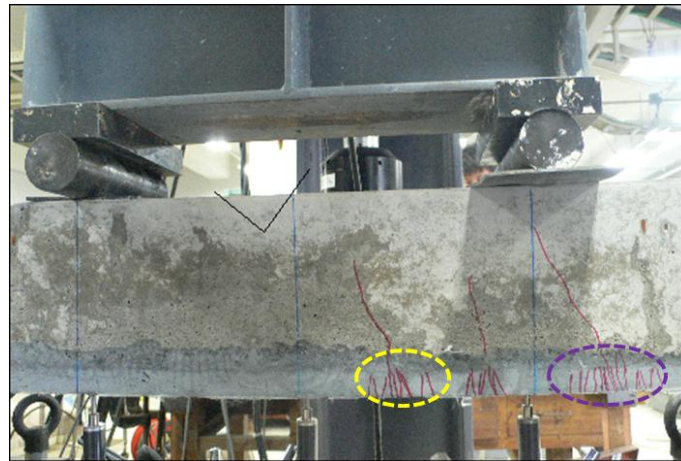
Figure 5.9 Crack pattern for case U-10

Figure 5.10 shows the crack patterns of case U-30 at the position marked in load-displacement curve.

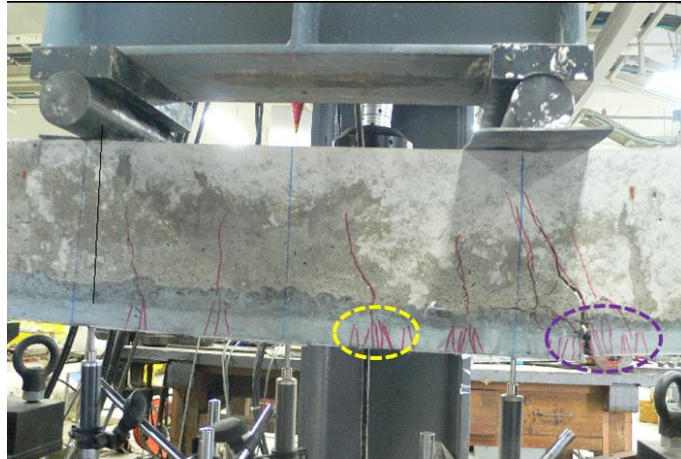
At point 1, there are two types of multiple fine cracks distributing in UHP-SHCC layer. One type comes from zero-span tensile behavior, with many multiple fine cracks around the localized crack in RC control beam (marked as dotted yellow circle), these multiple fine cracks occur due to damage in UHP-SHCC layer caused by stress concentration from localized crack in RC substrate beam, and multiple fine cracks spread from top of the UHP-SHCC layer to the bottom. However, another type comes from uniaxial tensile behavior, with many multiple fine cracks spread from bottom of UHP-SHCC layer to top (marked as dotted purple circle), these multiple fine cracks occur due to bending effect of the test.

At point 2, the load carrying capacity is in dropping, due to some multiple fine cracks are in localizing, these localizing multiple fine cracks come from uniaxial tensile behavior by bending effect of the test. UHP-SHCC layer loses the ability to constrain the localized crack in RC substrate beam to open gradually.

At point 3, the strengthened layer of UHP-SHCC material has lost its load carrying capacity due to the completion of localization of those multiple fine cracks, and UHP-SHCC layer can't constrain localized crack in RC substrate beam to open, and debonding behavior occurs at last.



(a) Point 1



(b) Point 2



(c) Point 3

Figure 5.10 Crack pattern for case U-30

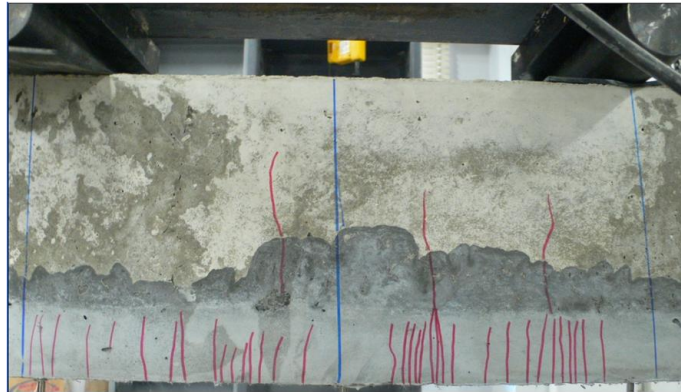
Figure 5.11 shows the crack patterns of case U-50 at the position marked in load-displacement curve.

At point 1, multiple fine cracks in UHP-SHCC layer are almost distributed evenly, which come from uniaxial tensile behavior, due to bending effect of test.

At point 2, the number of multiple fine cracks increases too many, quite different from case U-10 and U-50. This may implies that uniaxial tensile behavior comes from bending effect of the test play dominant role in this crack propagation pattern. Also, this illustrated the bending effect influences the crack propagation of multiple fine cracks, and these multiple fine cracks spread from bottom of the UHP-SHCC layer spread to the top of UHP-SHCC layer.

At point 3, the strengthened layer of UHP-SHCC material has lost its load carrying capacity due to the completion of localization of those multiple fine cracks, and

UHP-SHCC layer can't constrain the localized crack in RC substrate beam to open due to the localization at UHP-SHCC layer.



(a) Point 1



(b) Point 2



(c) Point 3

Figure 5.11 Crack pattern for case U-50

Therefore, for case U-10, the zero-span tensile behavior play important role in the crack propagation of multiple fine cracks in UHP-SHCC layer, the occurrence of multiple fine cracks in UHP-SHCC layer is due to the damage of UHP-SHCC layer caused by stress concentration from localized crack in RC substrate beam. These multiple fine cracks spread from the top of UHP-SHCC layer to bottom, and adjacent to the localized crack in RC substrate beam. For case U-30, the zero-span tensile behavior and uniaxial tensile behavior both influence the crack propagation of multiple fine cracks in UHP-SHCC layer. The uniaxial tensile behavior comes from the bending effect of the test. Multiple fine cracks coming from zero-span tensile behavior spread multiple fine cracks from top of UHP-SHCC layer to bottom. However, multiple fine cracks coming from uniaixal tensile behavior spread multiple fine cracks from bottom of UHP-SHCC layer to top. For case U-50, the uniaxial tensile behavior play important role in crack propagation of multiple fine cracks, due to the bending effect of test, and the multiple fine cracks distribution in UHP-SHCC layer are almost evenly.

5.4 Conclusion

Experiment of RC beam strengthened by UHP-SHCC layer with different thickness of 10mm, 30mm and 50mm is carried out in this chapter, and the result form experiment is investigated.

(1) After the yielding of reinforcement, the stiffness of load-displacement changes, and UHP-SHCC layer takes the load carrying capacity, and the load carrying capacity continues to increase. However, the load carrying capacity drops while the localization of multiple fine cracks occurs in UHP-SHCC layer, which means UHP-SHCC loses the load carrying capacity gradually.

(2) In the series of experiment, for case U-10, multiple fine cracks come from zero-span tensile behavior and spread from the top of UHP-SHCC layer (adjacent to the existing crack in RC substrate beam) to bottom of UHP-SHCC layer. For case U-30, some multiple fine cracks come from uniaxial tensile behavior and propagate from top of UHP-SHCC layer to bottom, but some multiple fine cracks come from uniaxial tensile behavior and spread from bottom of UHP-SHCC layer to top. For case U-50, multiple fine cracks come from uniaxial tensile behavior and distribute evenly, and spread from bottom of UHP-SHCC layer to top. The number of multiple fine cracks dramatically increases, which is quite different from case U-10 and U-50.

(3) The structural behavior can influence the crack propagation of multiple fine cracks in UHP-SHCC layer. For case U-10 with the thickness of 10mm for UHP-SHCC layer, the multiple fine cracks come from zero-span tensile behavior due to damage in

UHP-SHCC layer caused by stress concentration from localized crack in RC substrate beam. With the thickness of UHP-SHCC layer of 30mm for case U-30, zero-span tensile behavior and uniaxial tensile behavior both influence the crack propagation of multiple fine cracks in UHP-SHCC layer. However, for case U-50, with the thickness of 50mm, the uniaxial tensile behavior from bending effect of test dominantly influence the crack propagation of multiple fine cracks, and these multiple fine cracks spread from bottom of the UHP-SHCC layer spread to the top of UHP-SHCC layer.

CHAPTER 6

NUMERICAL EVALUATION ON FLEXURAL BEHAVIOR OF RC BEAMS STRENGTHENED BY UHP-SHCC

6.1 Introduction

UHP-SHCC has obvious advantages on repairing or retrofitting damaged concrete structures, due to its hardening strain as well as high tensile and compressive strength, and it will have a bright future. However, the elongation of multiple fine cracks of UHP-SHCC used as a repair or strengthening material is limited in a range adjacent to the existing crack in RC concrete members, which reduces the advantage of high ductility of UHP-SHCC material obtained from uniaxial tensile behavior, as analyzed numerically based on zero-span tensile test (Kamal et al., 2008) in chapter 2.

As investigated in chapter 5 experimentally, the crack propagation behaviors of UHP-SHCC used as a repair or retrofitting material for concrete members vary with the different thickness of UHP-SHCC layer. Therefore, accurate evaluation method is required to disclose the fracture mechanism of UHP-SHCC used as a repair or retrofitting material for concrete members.

In this chapter, a new type of zero-span tensile model is proposed with a pair of fictitious elastic material has the same Young's modulus with concrete, instead of the steel plate in the former zero-span tension test. This pair of fictitious elastic material is used to form an artificial crack assuming as always elastic without cracking, which is identical to the localized crack in RC substrate beam. This new proposed type of zero-span tensile model also can obtain the average behavior of UHP-SHCC used as a repair and strengthening material for the substrate with crack. Based on this new proposed zero-span tensile model, numerical evaluation on flexural behavior of RC substrate beams strengthened by UHP-SHCC material with thickness of 10mm, 30mm and 50mm is conducted. The numerical results are similar with those observed from experiment shown in chapter 5. Based on this numerical result, the cracking mechanism of multiple fine cracks in UHP-SHCC with different thickness is investigated.

6.2. Numerical simulation of tested beams strengthened by UHP-SHCC using uniaxial tensile model

RC beams strengthened by UHP-SHCC layer with thickness of 10mm case (case U-10), 30mm case (U-30) and 50mm case (case U-50) are simulated using FE method with uniaxial tensile behavior of tri-linear curve model considering fracture energy in this section. This uniaxial tensile behavior of tri-linear curve model considering fracture energy has been discussed in chapter 2. The stress-strain relationship obtained from

uniaxial tensile test and the abstracted tri-linear curve for lower limit of ultimate tensile strength are shown in Figure 6.1. Due to the material is always damaged from the weak area. The discussion on numerical evaluation is based on the stress-strain relationship of lower limit of ultimate tensile strength. Table 6.1 shows the parameters in tri-linear curve model considering fracture energy, abstracted from uniaxial tensile test, which is stress-strain relationship for numerical analysis with mesh size of 12.5mm and 25mm.

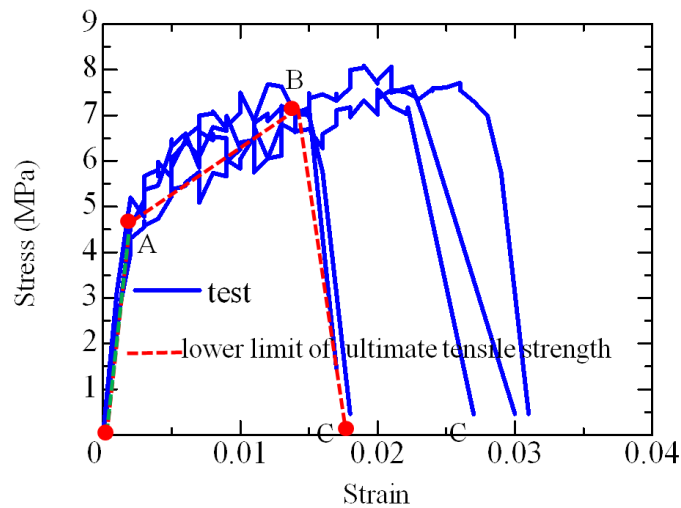


Figure 6.1 Stress versus strain for UHP-SHCC from test and numerical model

Table 6.1 Stress and strain values of tri-linear curve model

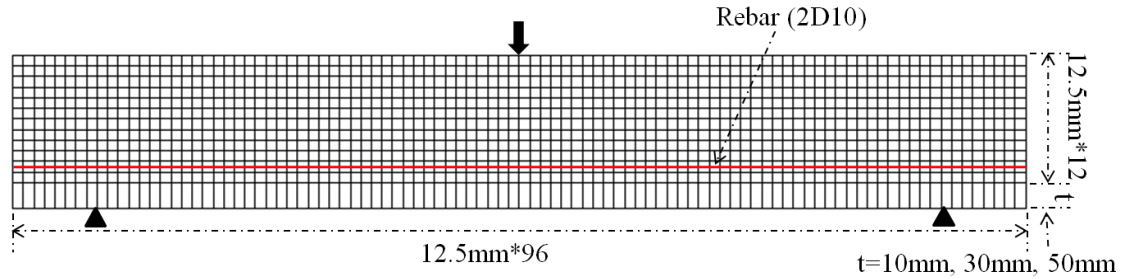
Mesh size	Point A		Point B		Point C	
	σ	ϵ	σ	ϵ	σ	ϵ
12.5mm	4.4	0.00018	7.0	0.015	0	0.062
25mm	4.4	0.00018	7.0	0.015	0	0.038

Note: the units of σ is N/mm^2

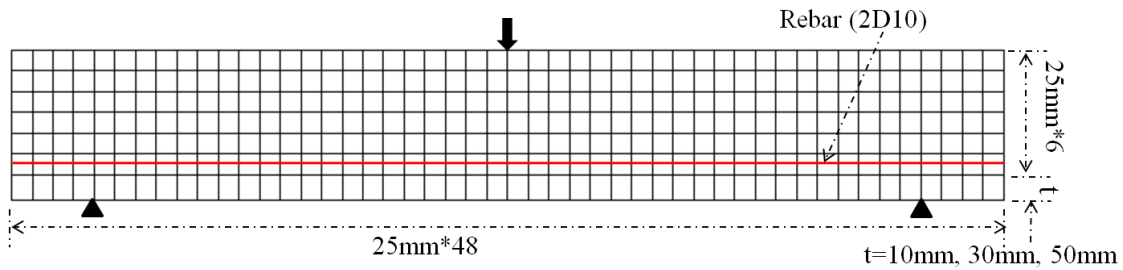
Figure 6.2 shows the mesh size for the numerical analysis. Two mesh sizes of 12.5mm*12.5mm, 25mm*25mm for RC control beam are adopted for numerical simulation. For case U-10, U-30 and U-50, the RC substrate beam part has the same mesh sizes with RC control beam, and the mesh sizes of 12.5mm*t, 25mm*t (t=10mm, 30mm and 50mm for U-10, U-30 and U-50 respectively) are adopted for UHP-SHCC layer. The longitudinal reinforcements are modeled by truss elements, and the bond stress-slip relationship between concrete and rebar is introduced in connection element, and crack distribution can be simulated with accuracy due to the bond effect (Sawabe et

al., 2006). Boundary condition is set at the bottom of the specimen and incremental displacement is applied at the center of the specimen.

In this numerical simulation, the constitutive model of Lattice Equivalent Continuum Model (LECOM) is adopted. The outline has described in chapter 4.



(a) Mesh size of 12.5mm



(b) Mesh size of 25mm

Figure 6.2 Mesh size for numerical analysis

Figure 6.3 shows the comparison of load-displacement curves between test and numerical analysis for mesh size of 12.5mm and 25mm, for RC control beam, case U-10, U-30 and U-50 respectively. The numerical results of load-displacement curves for RC control beam coincide with test one. However, for case U-10, the load-displacement curve for mesh size of 12.5mm is different from that for mesh size of 25mm.

For case U-30, the load-displacement curve for mesh size of 12.5mm coincides with that for mesh size of 25mm, but all load carrying capacities are overestimated, compared with test one.

For case U-50, the load-displacement curve for mesh size of 12.5mm also coincides with that for mesh size of 25mm, but all load carrying capacities are also overestimated, compared with test one. This behavior is similar with that of case U-30.

For case U-30 and U-50, the load carrying capacities drop suddenly, and the displacements corresponding to peak load are the same.

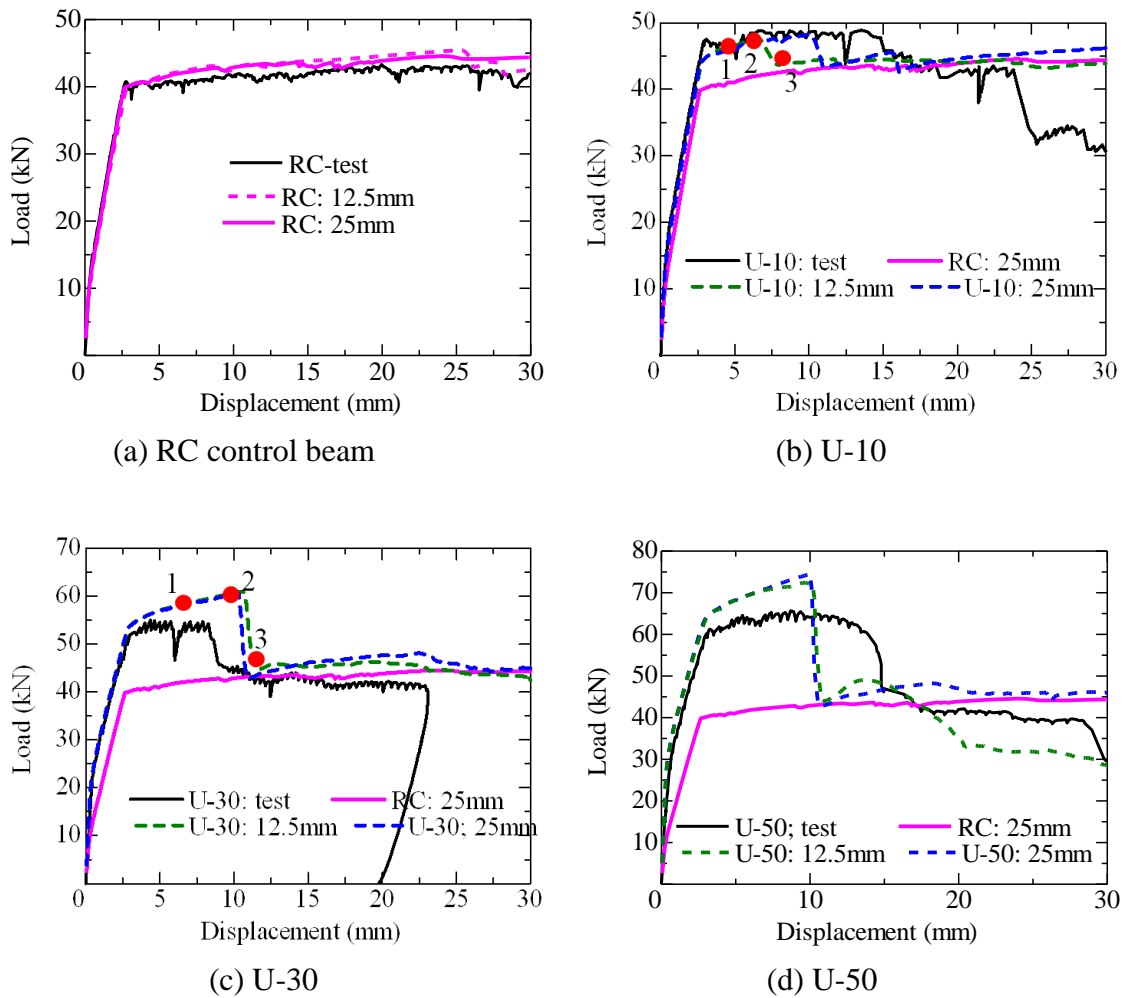


Figure 6.3 Comparison of load-displacement between test and numerical analysis

Figure 6.4 shows longitudinal strain distribution and deformation for case U-10 with mesh size of 12.5mm at point 1 to 3 marked in Figure 6.3(b). The strains at point 1 shows the localized cracks occur in RC substrate beam firstly, with some multiple fine cracks adjacent to them. At point 2, strain distribution in UHP-SHCC layer localized, and UHP-SHCC layer can continue to constrain the crack open in RC substrate beam (deformation at point 2). At point 3, the UHP-SHCC layer has lost load carrying capacity, and localized cracks open, which can be seen from deformation at point 3.

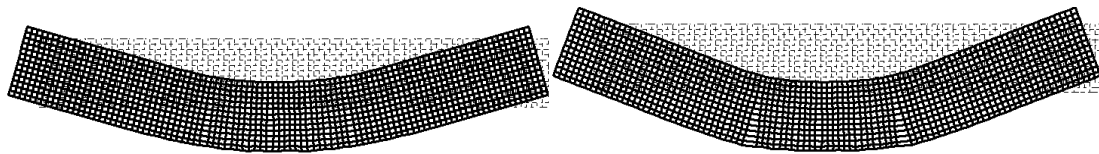
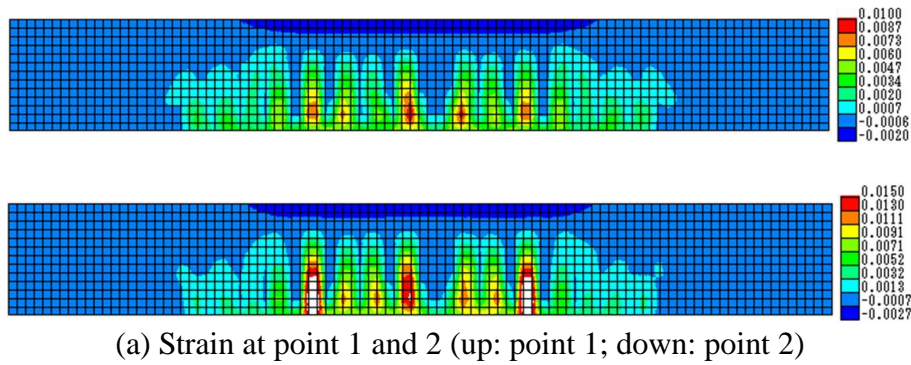


Figure 6.4 Longitudinal strain and deformation for U-10

Figure 6.5 shows longitudinal strain distribution and deformation for case U-30 with mesh size of 12.5mm at point 1 to 3 marked in Figure 6.3(c). The strain at point 1 and 2 show the uniform strain distribution in the UHP-SHCC layer, and the zero-span tensile behavior will not occur. This behavior is quite different from the behavior observed from experiment. Therefore, the load carrying capacity is overestimated in analysis. U-50 shows similar behavior with U-30.

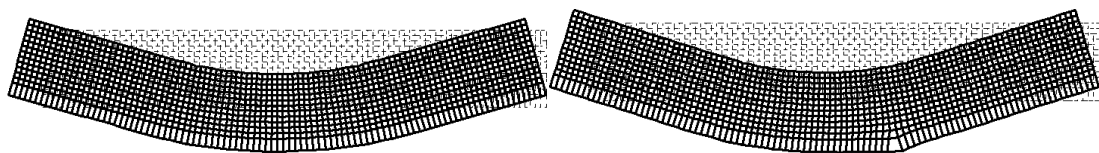
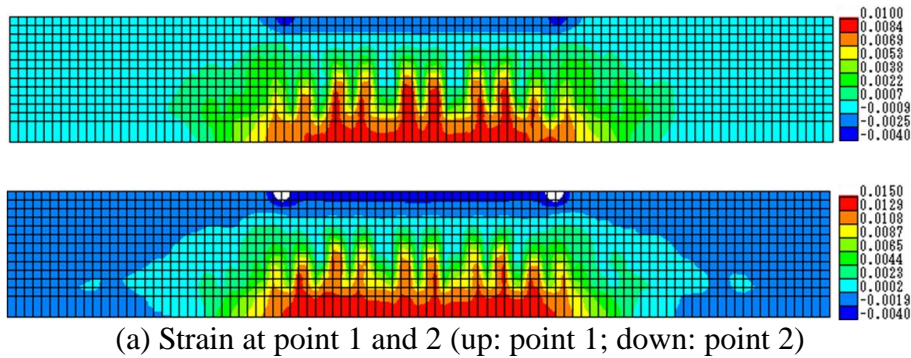


Figure 6.5 Longitudinal strain and deformation for U-30

6.3. Propose of zero-span tensile model

It was shown that the uniaxial tensile model considering fracture energy can't apply to numerical analysis of RC substrate beam strengthened by UHP-SHCC layer directly.

In order to appropriately conduct numerical analysis of RC beam strengthened by UHP-SHCC layer, a type of zero-span tensile model is proposed in this section, which can consider the average behavior of multiple fine cracks limited in a ranged area in one element.

6.3.1 Zero-span tensile model for UHP-SHCC used as a repair material for substrate with crack

In this section, a new type of zero-span tensile model was proposed for UHP-SHCC material, which was used as a repair material for the substrate with existing crack. In this proposed zero-span tensile model shown in Figure 6.6, a pair of fictitious material, which has the same Young's modulus with concrete, is adopted to replace the steel plates used in the former zero-span tension test, and artificial crack can be also formed by this pair of fictitious material. Because the numerical strain distributions of zero-span tensile test using steel plates always spread from top of UHP-SHCC layer (adjacent to artificial crack) to bottom regardless of the thicknesses of UHP-SHCC layer, which are different from the crack propagation processes observed from experiment. This pair of fictitious elastic material is assumed as always elastic without cracking, which is similar with the area around localized crack in RC substrate beam. Based on numerical result, the depth of this fictitious elastic material does not influence the zero-span tensile behavior. Therefore, the depth of this fictitious elastic material is also adopted as 3mm shown in Figure 6.6. This proposed zero-span tensile model also can obtain the average behavior of multiple fine cracks (in UHP-SHCC layer) limited in a ranged area adjacent to localized crack (in RC substrate beam), which is the average behavior of UHP-SHCC used as a repair material for the substrate with crack.

There are some assumptions for boundary condition in the proposed zero-span tensile model, which are conformed to the area of RC substrate beam and UHP-SHCC layer, around localized crack in RC substrate beam. Top surface is fixed in vertical direction. One of the lateral surfaces is fixed in longitudinal direction, and the other lateral surface is added with displacement increment for loading, as shown in Figure 6.6.

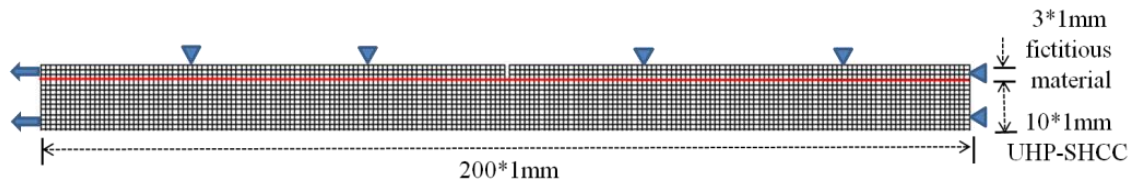
Figure 6.6 shows three geometries of zero-span tensile model for UHP-SHCC layers with thicknesses of 10mm, 30mm and 50mm (case Z-U-10, Z-U-30 and Z-U-50), which correspond to the three specimens of RC beam strengthened by UHP-SHCC in experiment. Small mesh size of 1mm is adopted to simulate multiple fine cracks in UHP-SHCC layer, which is smaller than the crack spacing (larger than 3mm) obtained

from experiment for strengthened RC beams. Similarly, tri-linear curve model with the case of lower limit of ultimate tensile strength is used. Table 6.2 shows the parameters in tri-linear curve model considering fracture energy, with mesh size of 1mm.

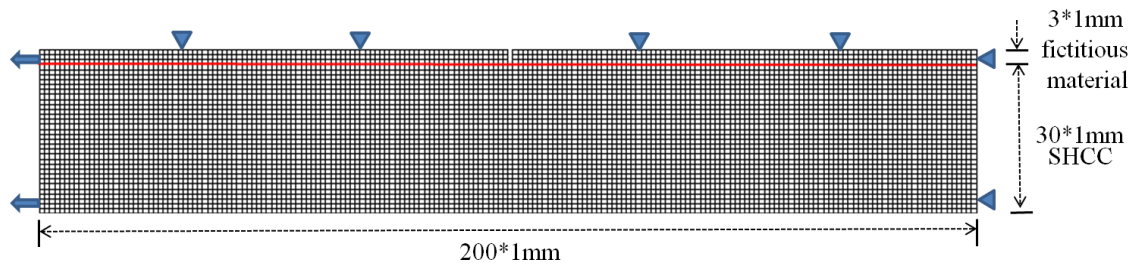
Table 6.2 Stress and strain values of tri-linear curve model

Point A		Point B		Point C	
σ	ϵ	σ	ϵ	σ	ϵ
4.4	0.00018	7.0	0.015	0	0.59

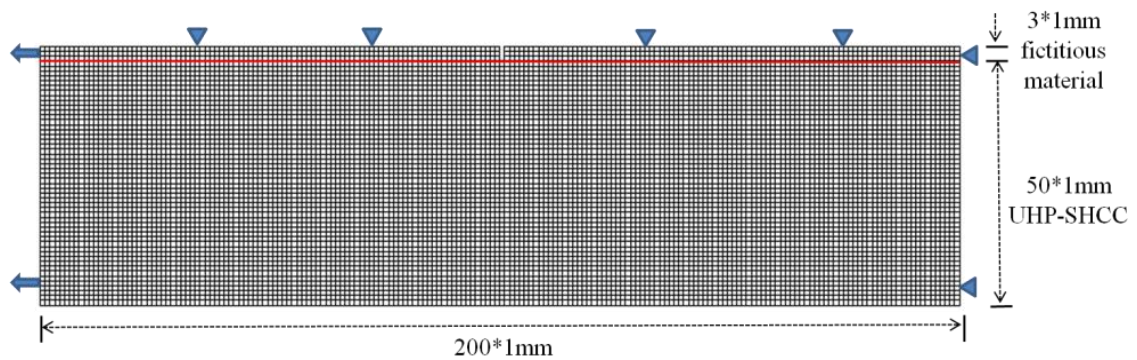
Note: the units of σ is N/mm^2



(a) Geometry of fictitious zero-span tension model for case Z--U-10



(b) Geometry of fictitious zero-span tension model for case Z-U-30



(c) Geometry of fictitious zero-span tension model for case Z-U-50

Figure 6.6 Geometry of fictitious zero-span tension model

Figure 6.7 shows the result of stress-displacement curves obtained from zero-span

tensile model. It can be seen that the tension strength and elongation obtained from zero-span tension model are obviously smaller than that from uniaxial tension model with lower limit of ultimate tensile strength. Moreover, the peak stress and softening curve depend on thickness of UHP-SHCC layer.

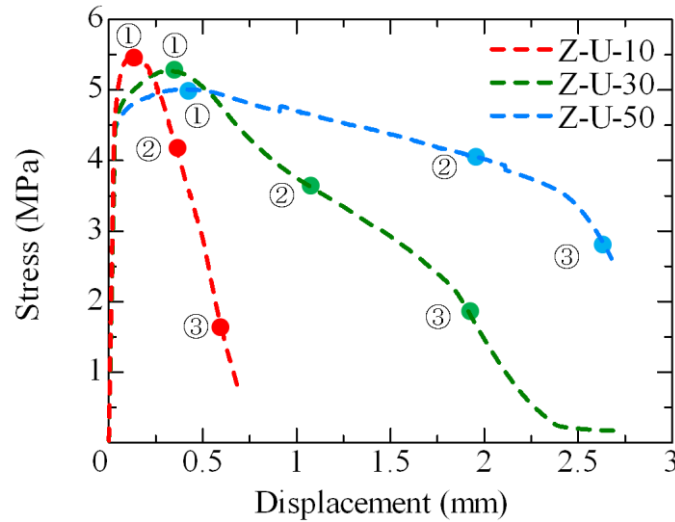


Figure 6.7 Stress-displacement curves from zero-span tensile model

Figure 6.8 to 6.10 show longitudinal strain distributions (0.015 is the strain corresponding to ultimate tensile strength) at point 1 to 3 (marked in Figure 6.7) for case Z-U-10, Z-U-30 and Z-U-50 with thicknesses of 10mm, 30mm and 50mm for UHP-SHCC layer for zero-span tensile behavior. The strain corresponding to initial crack is about 0.00018 for all cases, which is the same with uniaxial tensile behavior.

In case Z-U-10, strain propagates from top of UHP-SHCC layer (adjacent to artificial crack) to bottom, but is ranged in a area adjacent to artificial crack due to zero-span tensile behavior caused by stress concentration from artificial crack, and the localized area has no change after peak stress (point 2 and 3), the same with concentrated strain area at peak stress (point 1) with the value of 19mm, as marked in Figure 6.8(a). In this section, the localized area was defined by strain equal to 0.015 (red area) or larger than 0.015 (white area), and 0.015 was the value for strain corresponding to ultimate tensile strength.

In case Z-U-30, strain propagates from top of UHP-SHCC layer (adjacent to artificial crack) and bottom of UHP-SHCC layer simultaneously. Strains spread from top to bottom is ranged in an area, due to zero-span tensile behavior caused by stress concentration from artificial crack, but strain spread from bottom to top due to uniaxial tensile behavior caused by bending effect from the specimen. The localized area has no change after peak stress (point 2 and 3), the same with concentrated strain area at peak

stress (point 1) with the value of 30mm, as marked in Figure 6.9(a).

In case Z-U-50, strain also propagates from top of UHP-SHCC layer (adjacent to artificial crack) and bottom of UHP-SHCC layer simultaneously, but this propagation from bottom of UHP-SHCC is more obviously than that of Z-U-30. Strain spread from bottom to top due to uniaxial tensile behavior caused by bending effect of the test. The localized area has no change after peak stress (point 2 and 3), the same with concentrated strain area at peak stress (point 1) with the value of 34mm, as marked in Figure 6.10(a).

These behaviors are similar with crack propagation behavior of RC beam strengthened by UHP-SHCC from experiment. It may imply this zero-span tensile model of UHP-SHCC can be used to evaluate the fracture behavior of RC beams strengthened by UHP-SHCC with different thicknesses.

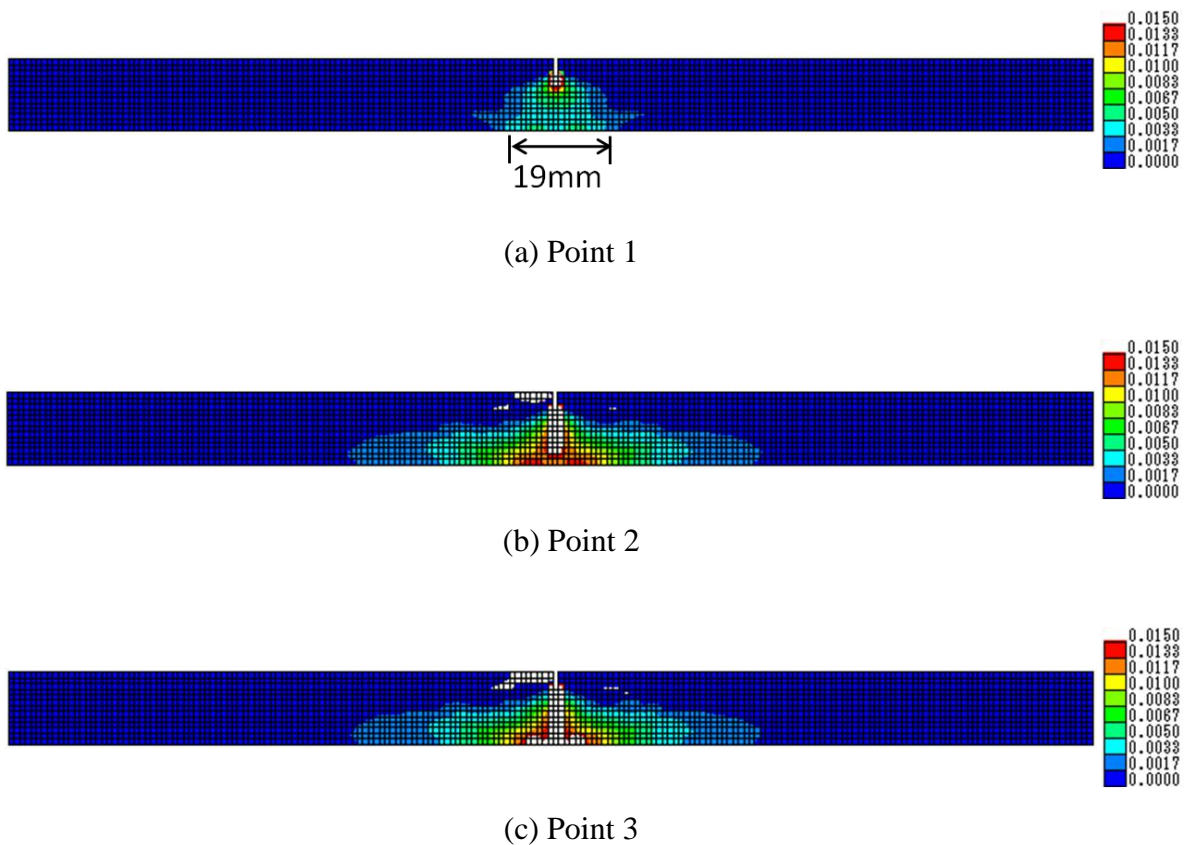
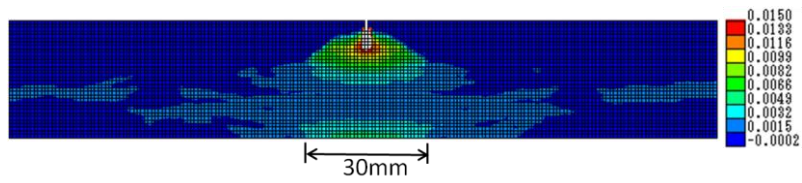
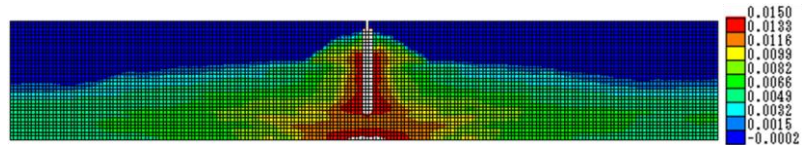


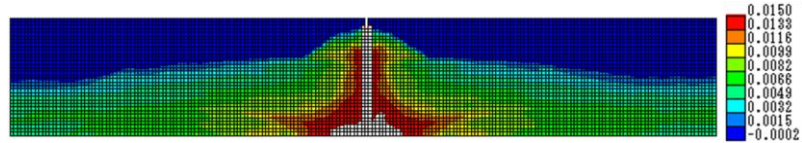
Figure 6.8 Longitudinal strain distribution of Z-U-10



(a) Point 1

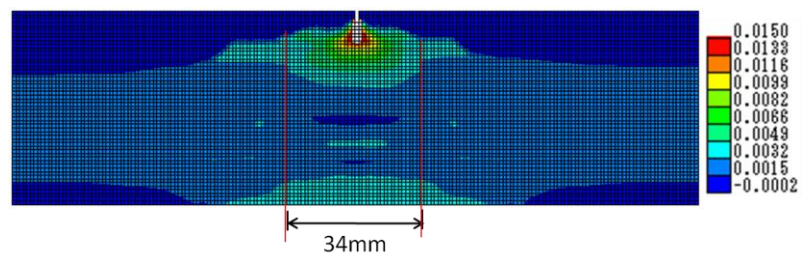


(b) Point 2

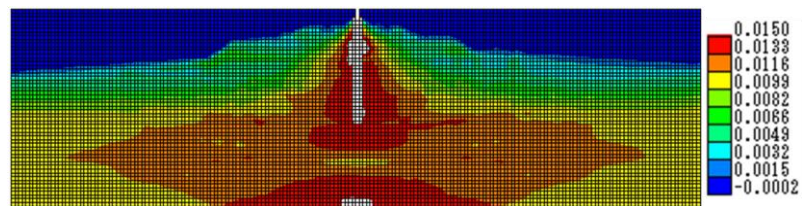


(c) Point 3

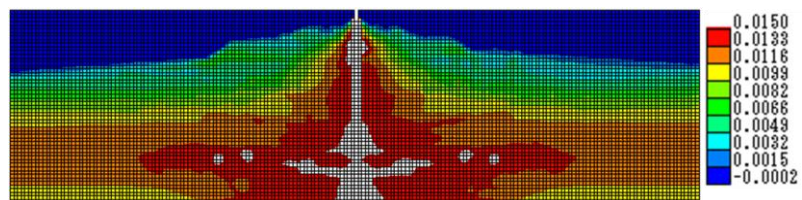
Figure 6.9 Longitudinal strain distribution of Z-U-30



(a) Point 1



(b) Point 2



(c) Point 3

Figure 6.10 Longitudinal strain distribution of Z-U-50

6.3.2 Stress-strain relationship obtained from zero-span tension model

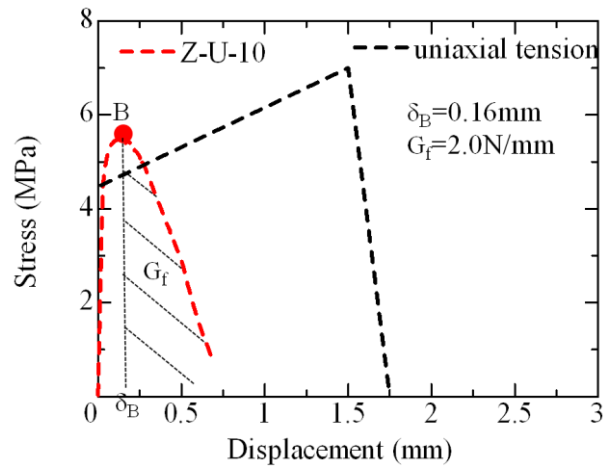
As described in Figure 6.8 to 6.10, the strain concentrated and localized areas are identical for zero-span tensile model for case Z-U-10, Z-U-30 and Z-U-50. Therefore, the average behavior of UHP-SHCC used as repaired material for RC substrate member with crack should be modeled by considering the strain localized area length L_{loc} . Then, it can be assumed that the strain in the area except the strain localized area is negligibly small, and the total displacement obtained from the zero-span tensile model is nearly equal to the displacement of the strain localized area.

Figure 6.11 shows the longitudinal stress versus displacement of zero-span tensile model for Z-U-10, Z-U-30 and Z-U-50, compared with that from uniaxial tensile behavior. It can be obviously seen that the tensile strength and elongation of zero-span tension model are smaller than those of uniaxial tensile behavior. From these longitudinal stress-displacement curves, the stress-strain relationships of the average material property of UHP-SHCC applied for strengthened beams can be obtained, which were also assumed as tri-linear curve model considering fracture energy, as described in chapter 2. Point A, B and C for tri-linear curve model are the positions corresponding to stress with initial crack, peak stress and minimum stress about 0, based on zero-span tension model, parameters of stress and strain for point A, B and C are listed in Table 6.3. The stress and strain of point A are the same with those of material model under uniaxial tensile behavior, due to stress just generates initial crack. The stress of point B is defined by the maximum stress obtained from zero-span tensile behavior, and the strain is defined by the displacement (δ_B) corresponding to the maximum stress dividing localized area length (L_{loc}), as shown in Figure 6.8(a), 6.9(a), 6.10(a) and Table 6.3, which is defined as the length of localized strain area. The strain at point C is defined by the fracture energy G_f after peak, which equals to the area of stress-displacement relationship after peak. That is,

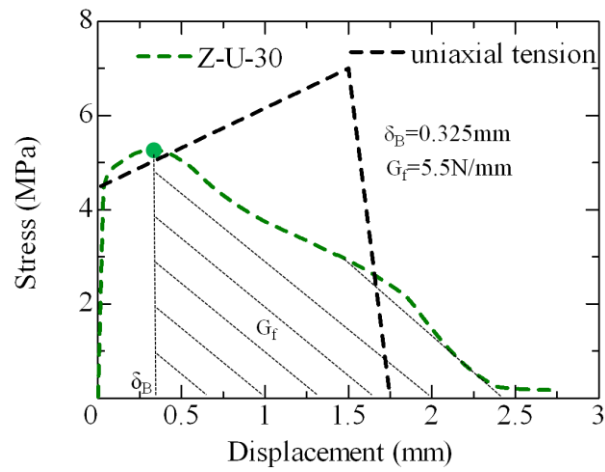
$$\varepsilon_B = \frac{\delta_B}{L_{loc}} \quad (6.1)$$

$$\varepsilon_C = \varepsilon_B + \frac{2G_f}{\sigma_B \cdot L_{elm}} \quad (6.2)$$

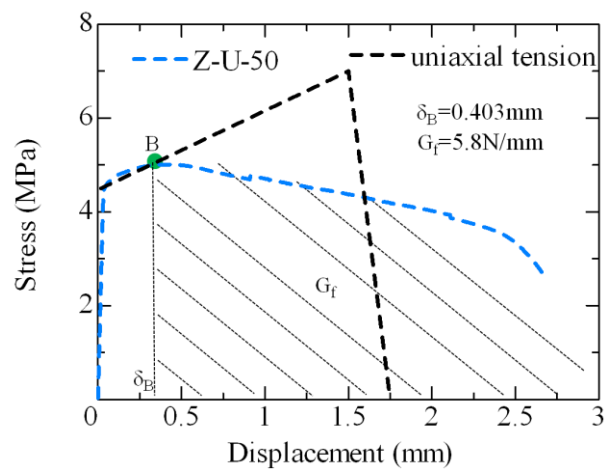
where ε_B : Strain at point B σ_B : Stress at point B
 δ_B : displacement at point B (mm) L_{loc} : localized area length
 L_{elm} : Element size (mm) ε_C : Strain at point C
 G_f : The absorbed energy after peak (N/mm).



(a) Z-U-10



(b) Z-U-30



(c) Z-U-50

Figure 6.11 Longitudinal stresses versus displacement of zero-span tension model

Table 6.3 Stress and strain values of tri-linear curve model

	Point A		Point B		Point C			L_{loc} (mm)
	σ	ε	σ	ε	σ	ε_1	ε_2	
U-10	4.4	0.00018	5.5	0.0084	0	0.067	0.037	19
U-30	4.4	0.00018	5.3	0.011	0	0.177	0.094	30
U-50	4.4	0.00018	5.0	0.0119	0	0.198	0.105	34

Note: the units of σ is N/mm^2

ε_1 and ε_2 corresponding to element length 12.5mm and 25mm respectively

6.4. Numerical evaluation on flexural behavior of RC beam strengthened by UHP-SHCC using the proposed zero-span tensile model

6.4.1 Brief introduction of numerical modeling

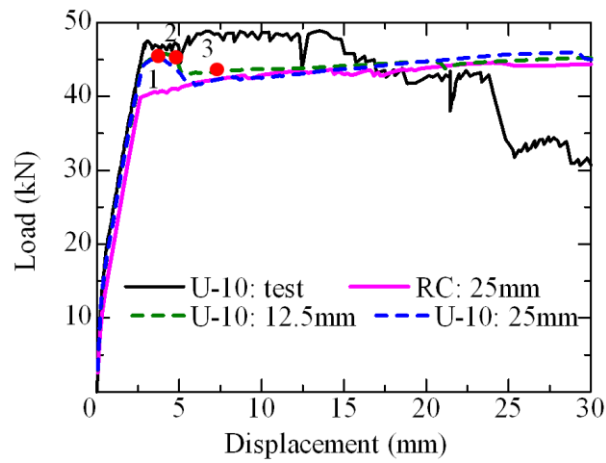
Based on the stress-strain relationship obtained from zero-span tensile model, the numerical evaluation on flexural behavior of RC beam strengthened by UHP-SHCC layer can be implemented. The mesh size for the numerical analysis is the same with the cases using uniaxial tensile model as shown in Figure 6.2. Moreover, the modeling of longitudinal reinforcements was also the same with the cases using uniaxial tensile model, as mentioned before.

6.4.2 Numerical result of RC beams strengthened by UHP-SHCC using zero-span tension model

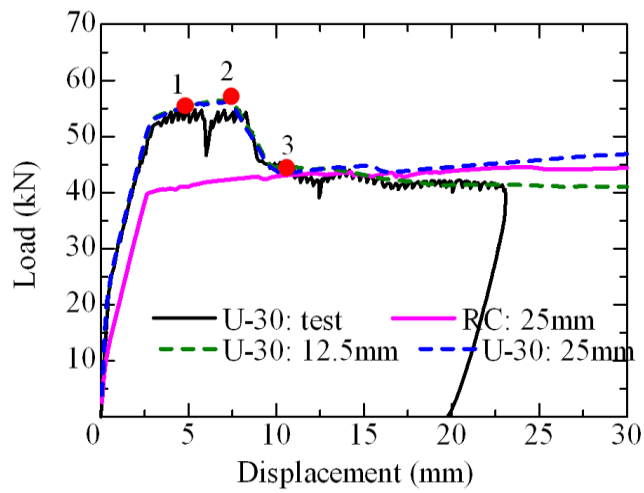
6.4.2.1 Load-displacement relationship

Figure 6.12 shows the Comparison of load versus displacement between experimental result and numerical result with mesh size of 12.5mm and 25m. It demonstrated that the experimental and numerical results had the same tendency, and the load carrying capacities of numerical evaluation are estimated appropriately. Besides, there is no problem of result depending on mesh size of element, which has occurred in numerical analysis with uniaxial tensile model. Because this numerical evaluation bases on the proposed new type of zero-span tensile model, which has considered the average behavior of UHP-SHCC used as a repair or retrofitting material with existing localized crack in RC concrete members.

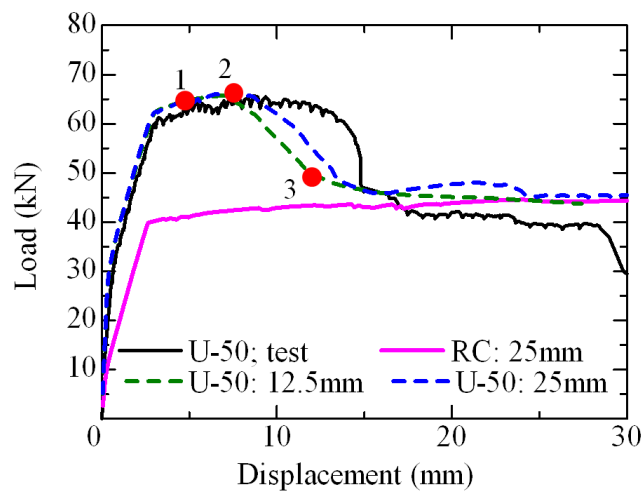
It also can be seen both of load carrying capacities and displacements corresponding to peak load increased with the increasing of thicknesses of UHP-SHCC, because of different crack propagation patterns, which will be discussed in the next section. For the case U-50, the softening part is a little different with the test result.



(a) U-10



(b) U-30



(c) U-50

Figure 6.12 Comparison of load-displacement curves for U-10, U-30 and U-50

6.4.2.2 Longitudinal strain distribution and deformation

Figure 6.13 to 6.15 show longitudinal strain distributions at point 1, 2 and deformations at point 2, 3 (marked in Figure 6.12) for case U-10, U-30 and U-50 respectively.

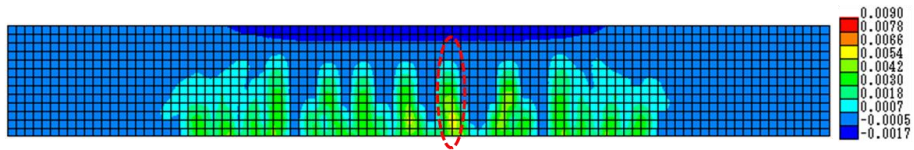
For case U-10, the localized strain occurs in RC substrate beam firstly as shown at point 1, and then multiple fine cracks occur in UHP-SHCC layer as shown at point 2, due to stress concentration from the tip of localized crack in RC substrate beam part, which is illustrated as dotted red circle in Figure 6.13.

For case U-30, the localized strain also occurs in RC substrate beam firstly at point 1, and then multiple fine cracks occur in UHP-SHCC layer at point 2. The strain distribution is quite different with the case using uniaxial tensile model as shown in Figure 6.5. In Figure 6.5, strain in the UHP-SHCC layer distributed and zero-span tensile behavior was not observed. On the other hand, the result in Figure 6.14 shows localized strain distribution from crack in RC substrate beam, which is similar with test results.

For case U-50, the crack propagation pattern of multiple fine cracks is obviously different from that of case U-10. In case U-50, multiple fine cracks occur from bottom of UHP-SHCC layer firstly, illustrated as longitudinal strain distribution at point 1 (marked as dotted red circle), and then spread from bottom of UHP-SHCC layer to top of UHP-SHCC layer, as shown in Figure 6.15, this behavior is also observed from experiment. Moreover, this behavior is also observed from the numerical simulation of proposed zero-span tensile model.

UHP-SHCC layer has load carrying capacities for all the cases, and constrain the localized crack in RC substrate beam to open, as shown at the deformation for point 2 for all the case. However, UHP-SHCC layer loses load carrying capacities and can't continue to constrain the localized crack in RC substrate beam to open, due to localization of multiple fine cracks in UHP-SHCC layer, as shown at point 3 for all the cases.

These behaviors are similar with those observed from experiment shown in chapter 5, also similar with the numerical simulation result from proposed zero-span tensile model. Therefore, it can be confirmed that the proposed zero-span tensile model is reasonable for numerical evaluation of UHP-SHCC material used as a repair or retrofitting material for damaged concrete structures.

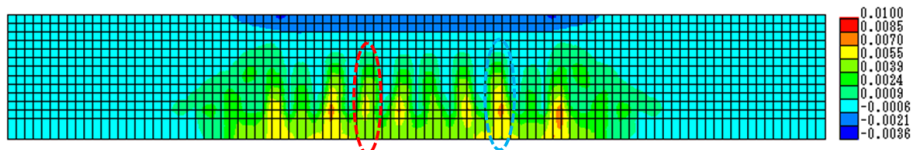


(a) Strain at point 1 and 2 (up: point 1; down: point 2)

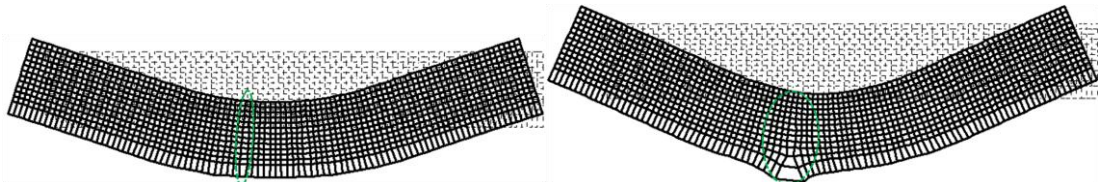


(b) Deformation at point 2 and 3 (left: point 2; right: point 3)

Figure 6.13 Longitudinal strain and deformation for U-10

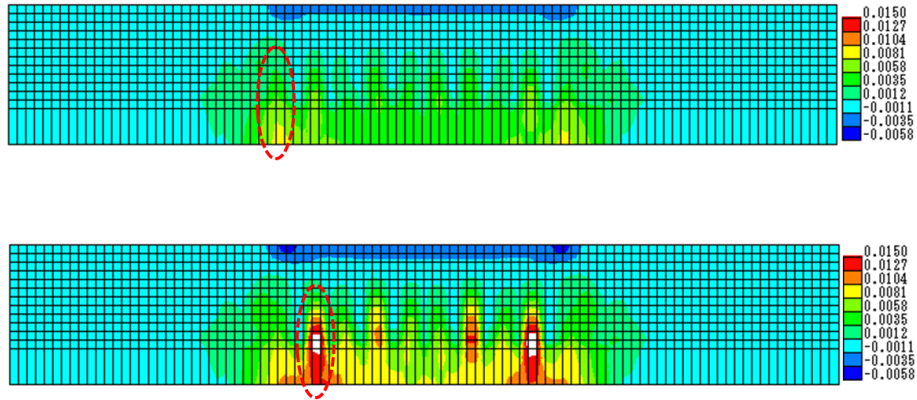


(a) Strain at point 1 and 2 (up: point 1; down: point 2)

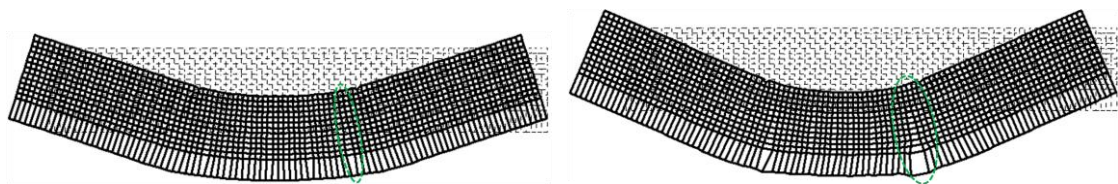


(b) Deformation at point 2 and 3 (left: point 2; right: point 3)

Figure 6.14 Longitudinal strain and deformation for U-30



(a) Strain at point 1 and 2 (up: point 1; down: point 2)



(b) Deformation at point 2 and 3 (left: point 2; right: point 3)

Figure 6.15 Longitudinal strain and deformation for U-50

6.5. Conclusion

In this chapter, RC beam strengthened by UHP-SHCC layer are evaluated numerically, and a type of zero-span tension model for UHP-SHCC used as a repair material for substrate with crack is proposed for the numerical evaluation of RC beam strengthened by UHP-SHCC, which can be applied to structural level with large mesh size.

(1) The numerical analysis of the strengthened RC beams using uniaxial tensile model can't be directly adopted for numerical analysis of strengthened RC beams with UHP-SHCC layer. For case U-30 and U-50, the analytical results overestimate the load carrying capacity, and have the same displacement, due to the uniform strain distribution, which are different from experimental observation. However, for case U-10, the load carrying capacities are different with different mesh size.

(2) The zero-span tensile model with fictitious elastic material is proposed. The fictitious material has the same Young's modulus with concrete and elastic stress-strain relationship without cracking. This zero-span tensile model considers the average behavior of multiple-fine cracks adjacent to existing crack in RC substrate beam.

(3) Numerical evaluation of RC beam strengthened by UHP-SHCC layer is conducted, considering the proposed zero-span tensile model, and the effectiveness of this proposed zero-span model is confirmed by the Comparison between experimental

and numerical results. The propagation of strain distribution is similar with the propagation of multiple fine cracks observed from experiment. The analytical load carrying capacities and displacement is similar with those obtained from experiment. For case U-50, the analytical result on softening part is a little different from experiment.

(4) Crack propagation processes of multiple fine cracks in UHP-SHCC layer are investigated by numerical analysis. Numerical results show crack propagation processes of multiple fine cracks in UHP-SHCC layer different with the increasing of thickness of UHP-SHCC layer. When the thickness of UHP-SHCC strengthened layer is 10mm, the multiple fine cracks propagate from the upside of UHP-SHCC layer near tips of localized crack in RC substrate beam to the bottom of UHP-SHCC layer. When the thickness of UHP-SHCC strengthened layer is 30mm, the multiple fine cracks propagates from upside to bottom and from bottom to upside of UHP-SHCC layer both. However, when the thickness of UHP-SHCC is 50mm, the multiple fine cracks propagate from the bottom to upside of UHP-SHCC layer. These behaviors are similar with those observed from experiment.

CHAPTER 7

NUMERICAL EVALUATION ON STRENGTHENING EFFECT OF RC COLUMN WITH UHP-SHCC MATERIAL SUBJECTED TO CYCLIC LOAD

7.1 Introduction

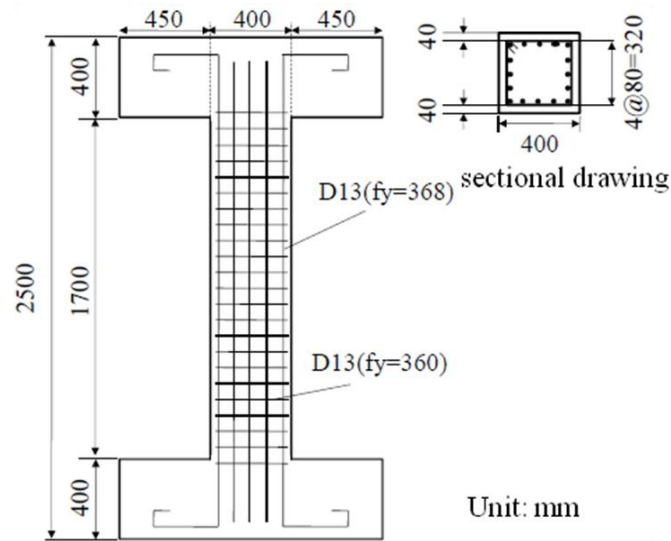
The constitutive model of UHP-SHCC for shear stress was proposed and the applicability was confirmed in chapter 4. The model to simulate the UHP-SHCC layer as repairing and strengthening material of concrete structure was proposed and the applicability was confirmed in chapter 6. One of practical application for strengthening with UHP-SHCC is seismic retrofit of RC members. The appropriate repair or strengthening method by UHP-SHCC material has been developed (Kunieda et al., 2012). However, seismic retrofit is usually applied by RC jacket, steel jacket and FRP jacket method. In this chapter, the strengthening effect of RC column strengthened by UHP-SHCC is evaluated numerically, based on the previous model, including tri-linear curve model, zero-span tensile model, and shear model.

7.2 Geometry for RC column strengthened by other materials

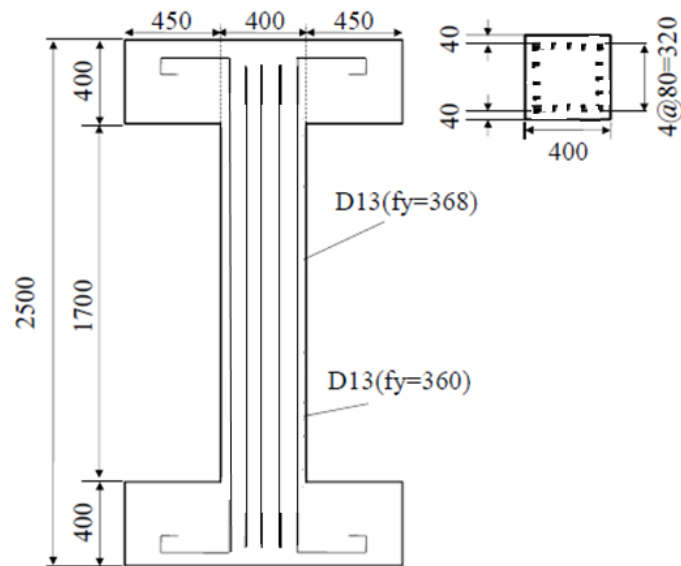
7.2.1 Geometry of RC column with and without web reinforcements

Figure 7.1 shows geometry of simulated RC column with web reinforcements (case CNTR-WEB) and RC column without web reinforcements (case CNTR). The section size is 600*600mm, and the length is 1700mm. The longitudinal reinforcement is D13 with the yield strength of 368N/mm², and 16 longitudinal reinforcements are arranged in one section with the reinforcement ratio of 0.44%. The web reinforcement is D13 with the yield strength of 360N/mm². The compressive strength of concrete is 29.3N/mm²

The UHP-SHCC jacket is assumed for the columns. The jacket thickness are 30mm and 50mm. Jacket part does not anchored to stubs and the space between jacket and stub is assumed 40mm. Moreover, the case of steel jacket with 6mm thickness is also assumed to compare with the columns with UHP-SHCC jacket.



(a) With web reinforcements



(b) Without web reinforcements

Figure 7.1 Geometry of RC column

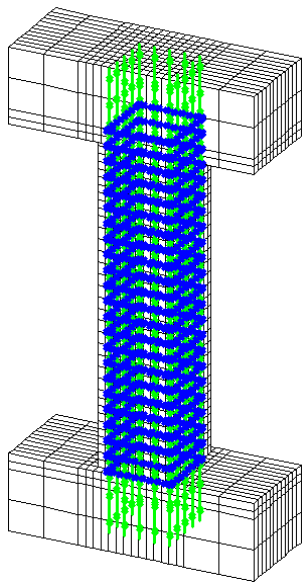
7.2.2 Numerical model

7.2.2.1 Analytical model of column

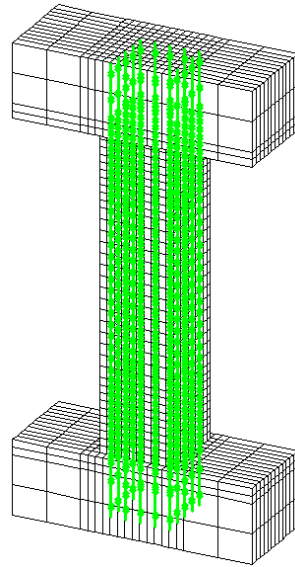
Figure 7.2 shows the analytical model for numerical analysis. The mesh size of column is 40*40*40mm, and mesh sizes for upside and down side stubs is 40*40*60mm for RC column. One layer of strengthening materials are added to the RC column, with the mesh size of 6*40*40mm for steel plate, 30*40*40mm and 50*40*40mm for UHP-SHCC material with the thickness of 30mm and 50mm

respectively, Then, perfect bond is assumed between RC column and the jacket. Discrete model is adopted for reinforcement, as used in chapter 6.

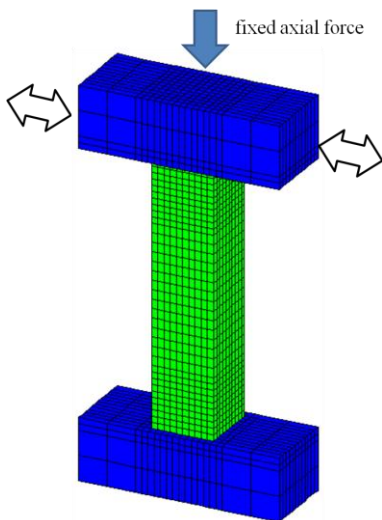
As shown in Figure 7.2(c) and (d), fixed force is applied to the top surface of upside stub in axial direction, and cyclic load is applied on the side surface of the upside stub by controlling displacement in horizontal direction. The bottom surface of downside stub is fixed without any displacement. The displacement is subjected to several cycles such as $+\delta y, -\delta y, +4\delta y, -4\delta y, +8\delta y, -8\delta y, +12\delta y, -12\delta y$.



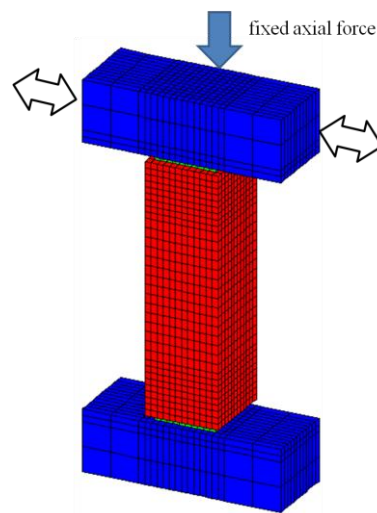
(a) With web reinforcement



(b) Without web reinforcement



(c) Mesh for RC column



(d) Mesh for strengthened RC column

Figure 7.2 Geometry of arrangement of reinforcements and mesh size

7.2.2.2 stress-strain relationship of concrete under cyclic load

Figure 7.3 shows the stress-strain relationship of concrete under cyclic load. As shown in Figure 7.3, unloading from tension branch is linearly decreasing with the slope equal to the initial slope (initial modulus) until concrete stress reaches zero, and then continue to the previous recursion point in compression zone. Unloading from compression branch is also linearly decreasing with the initial slope until concrete stress reaches zero, and continue with the zero stress until unloading point reaches the origin (assuming that concrete possess no tensile stress in compression zone). Reloading from compression zone is heading to the previous recursion point in tension zone. Unloading from some extend in tension softening branch (dotted line), stress is decreasing until it reaches zero with slope of initial slope and heads to a point with zero stress (assuming that concrete possess no compressive stress).

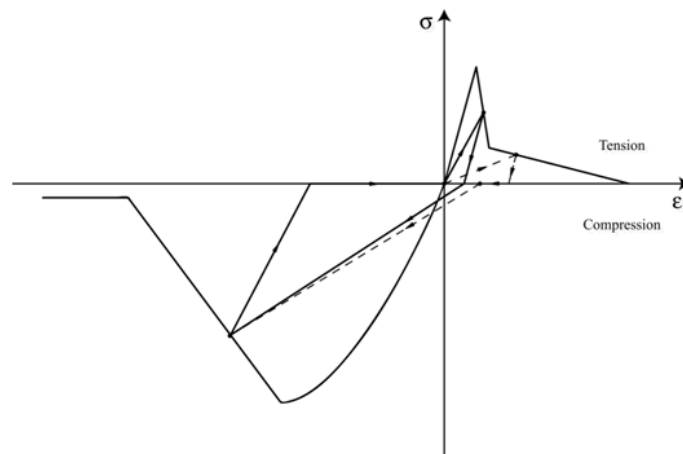


Figure 7.3 Stress-strain relationship for concrete under cyclic load

7.2.2.3 Stress-strain relationship of UHP-SHCC under cyclic load

As discussed in chapter 5 and 6 by experiment and numerical analysis, the zero-span tensile behavior occurs when UHP-SHCC used for strengthening the concrete structure. Therefore, the stress-strain relationship for zero-span tensile behavior should be adopted for UHP-SHCC material used for strengthening RC column. The zero-span tensile behavior of UHP-SHCC used for strengthening RC column with thickness of 30mm and 50mm can be obtained by the same procedures as discussed in chapter 6. Table 7.1 shows Point A, B and C of tri-linear curve model for the stress-strain relationship of UHP-SHCC used for strengthening RC column with thickness of 30mm and 50mm.

Table 7.1 Tri-linear curve model from zero-span tensile behavior

thickness		Point A	Point B	Point C
30mm	σ	5.0	5.83	0.0
	ε	0.000156	0.0078	0.0524
50mm	σ	5.0	5.89	0.0
	ε	0.000156	0.009	0.060

Note: the units of σ is N/mm^2

Figure 7.4 shows the stress-strain relationship for UHP-SHCC material with thickness of 30mm under cyclic load. Figure 7.4(a) shows the stress-strain relationship in compression. Figure 7.4(b) shows the stress-strain relationship in tension. Green arrow, black arrow and blue arrow belong to the first, second and third loop respectively. Simple similar hysteresis rule with concrete is assumed in tension and compression. Under the condition of reloading, the Young's modulus for tension and compression decreases with the increasing of loop. Under the condition of unloading, the Young's modulus for compression does not change between different loop, but the stress for tension suddenly drops.

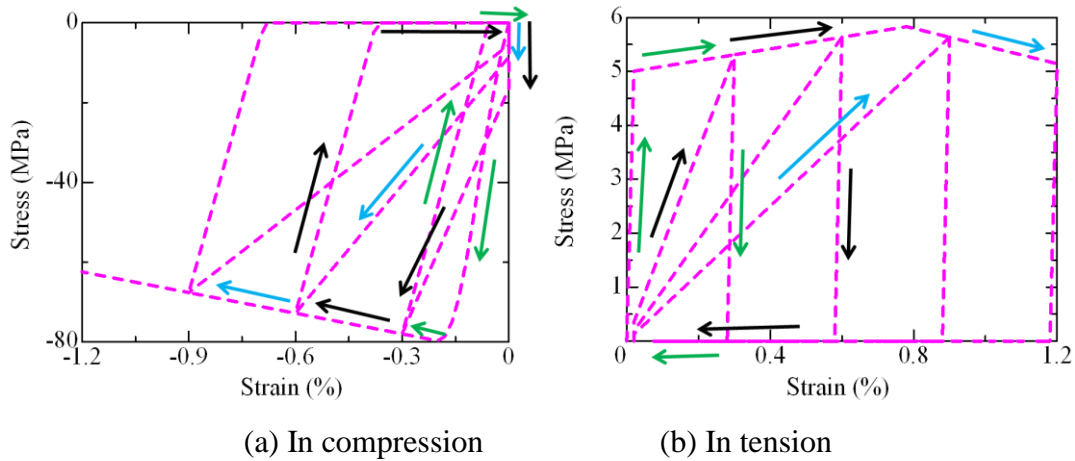


Figure 7.4 Stress-strain relationship of UHP-SHCC under cyclic load

Moreover, the shear stress transfer model discussed in chapter 4 is also adopted in this study.

7.2.2.4 Stress-strain relationship of steel

Figure 7.5 shows the stress-strain relationship for steel plate under cyclic load. The yield strength of this steel plate is assumed as $300\text{N}/\text{mm}^2$. Similar bi-linear relationship

is assumed for reinforcement.

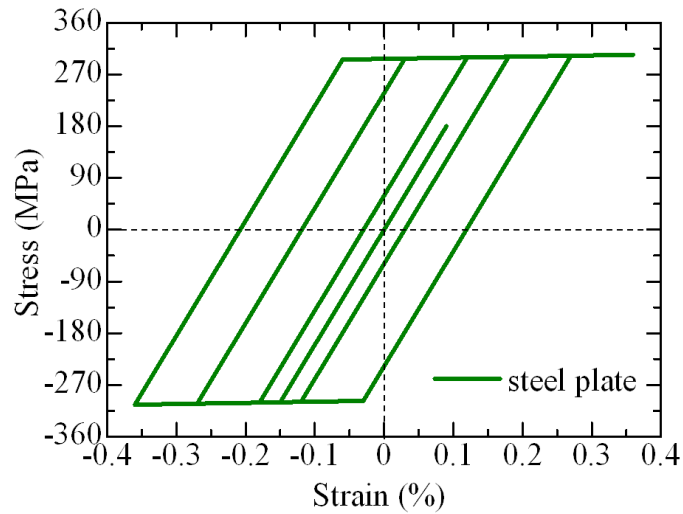


Figure 7.5 Stress-strain relationship of steel plate under cyclic load

7.2.3 Numerical result of RC column with and without web reinforcement

Figure 7.6 shows the load-displacement relationship for RC column without web reinforcement (case CNTR) and RC column with web reinforcement (case CNTR-WEB). For the case of CNTR as shown by solid line, load decreases with increasing displacement and the hysteresis loop shows thin behavior without energy absorption. On the other hand, for the case of CNTR-WEB, load carrying capacity does not decrease, and it shows a spindle shape with high energy absorption.

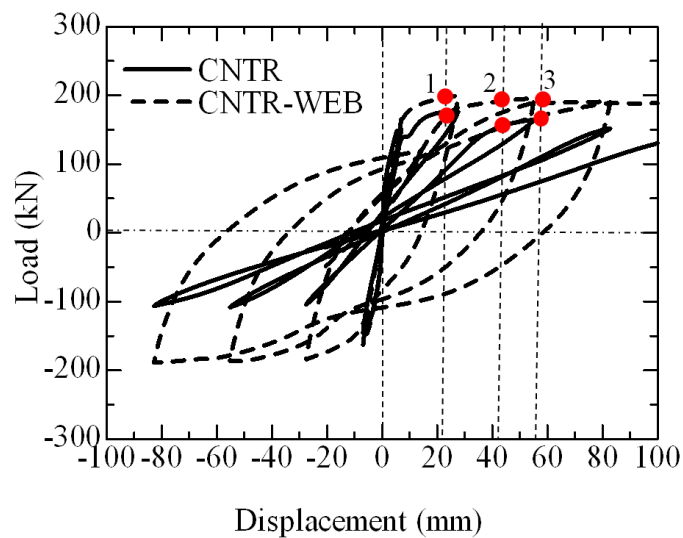
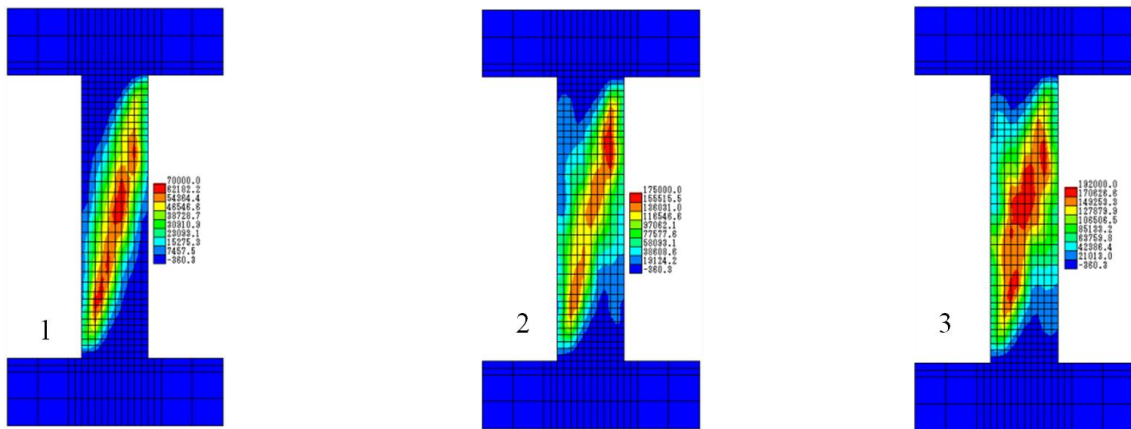


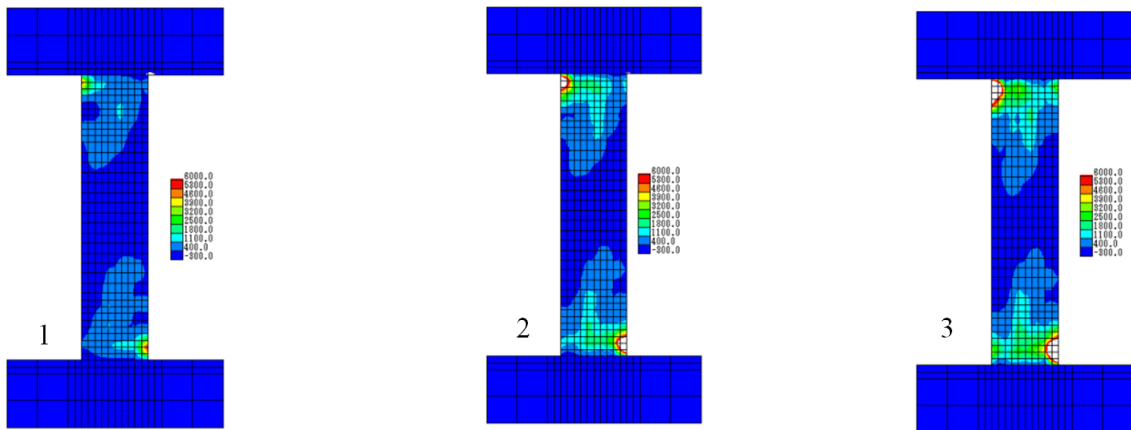
Figure 7.6 Load-displacement for case CNTR and CNTR-WEB

Figure 7.7 shows the strain distribution of case CNTR and CNTR-WEB at point 1, 2 and 3 as marked in Figure 7.6. The strain distribution for case CNTR spreads along the shear direction in a very large area, and the area of maximum strain distribution increases with the increasing of displacement. However, the strain distribution for case CNTR-HP spreads from the joint of stub and column at upside and downside, and the area of strain distribution increases, but the area is also not large.

Based on the results, it is obviously understood that, CNTR shows shear failure behavior and CNTR-WEB shows flexural failure behavior. Therefore, the effect of strengthening of CNTR is investigated in next section.



(a) Strain distribution of case CNTR at point 1, 2 and 3



(b) Strain distribution of case CNTR-WEB at point 1, 2 and 3

Figure 7.7 Strain distribution for case CNTR and CNTR-WEB

7.2.4 Evaluation on strengthening effect of RC column

The RC column without web reinforcements, CNTR, is strengthened by UHP-SHCC

material with the thickness of 30mm and 50mm named as case UHP-30 and UHP-50. The RC column is also strengthened by steel plate with the thickness of 6mm named as case ST-6.

Figure 7.8 shows the load-displacement relationship for case CNTR, ST-6, UHP-30 and UHP-50. It can be clearly seen the load–displacement are much similar between case ST-6, UHP-30 and UHP-50, and also can keep the peak load with the increasing of displacement. The relationship is similar with the RC column with web reinforcement, CNTR-WEB. It means the load carrying capacity of RC column without web reinforcements can be increased and kept, by means of UHP-SHCC material or steel plates.

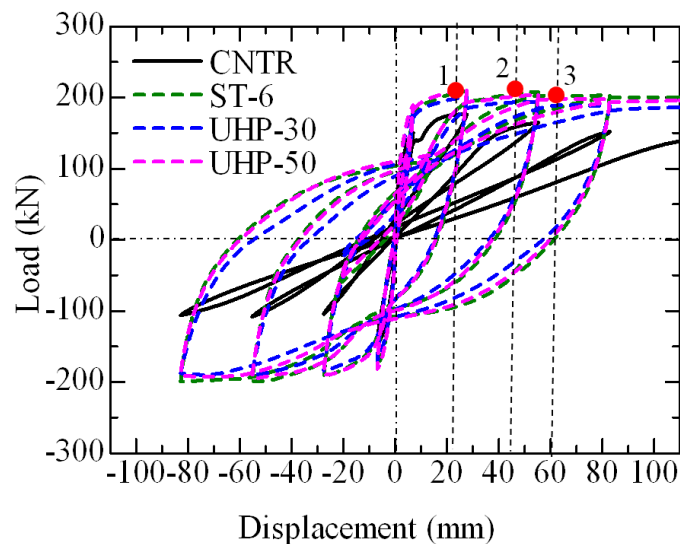
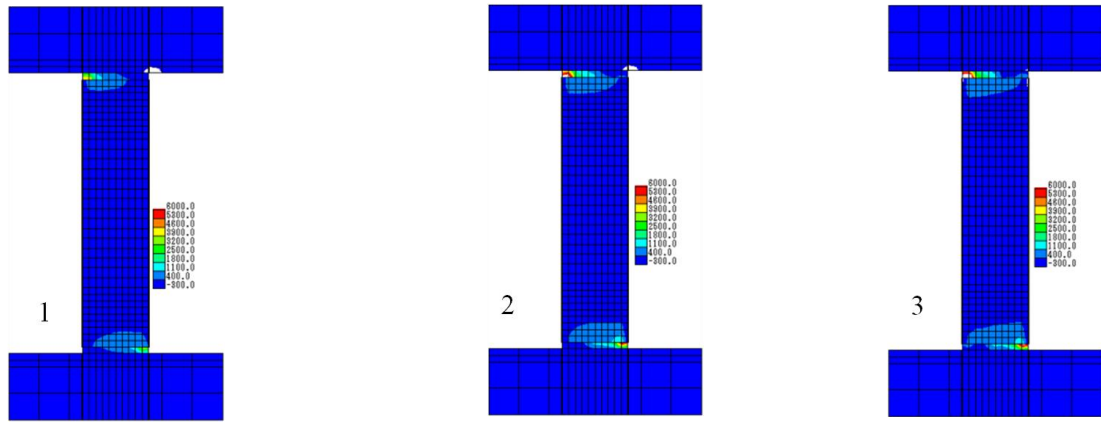


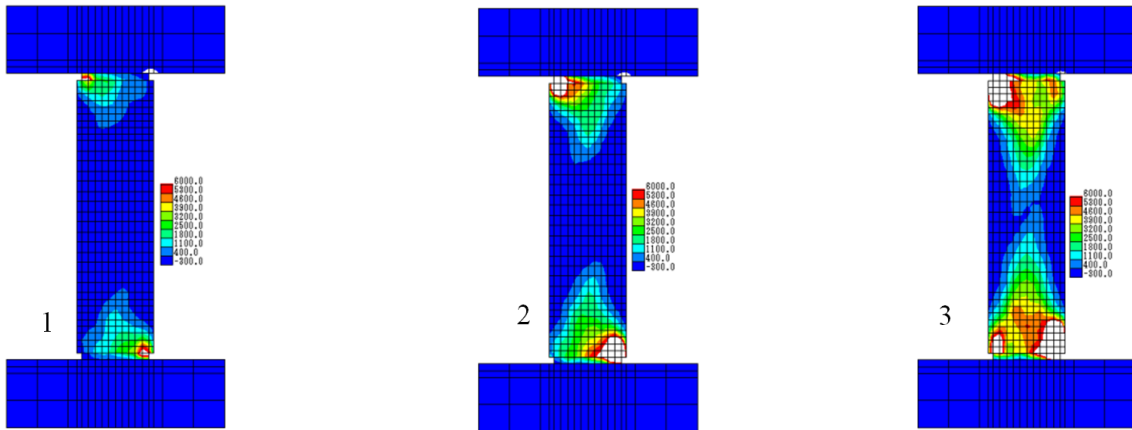
Figure 7.8 Load-disp. of strengthened RC column without web reinforcement

Figure 7.9 shows the strain distribution for case ST-6, UHP-30 and UHP-50 at point 1, 2 and 3 as marked in Figure 7.8. The strain distribution of case ST-6 is ranged in a very small area, near the joint between stub and column at upside and downside, and does not spread to other area with the increasing of displacement. The strain distribution is similar with RC column with web reinforcement as shown in Figure 7.7(b), which is typical flexural behavior. The strain distribution of case UHP-30 spreads from the joint of stub and column at upside and downside with the increasing of displacement. The strain distribution of case UHP-50 is similar with that of case ST-6, just the distributed area of case UHP-50 is a little larger than that of case ST-6, but still very small. Shear behavior is not observed for all strengthening method. Especially, the increasing of strain distribution of case UHP-50 and ST-6 are very small after the second loop, it may

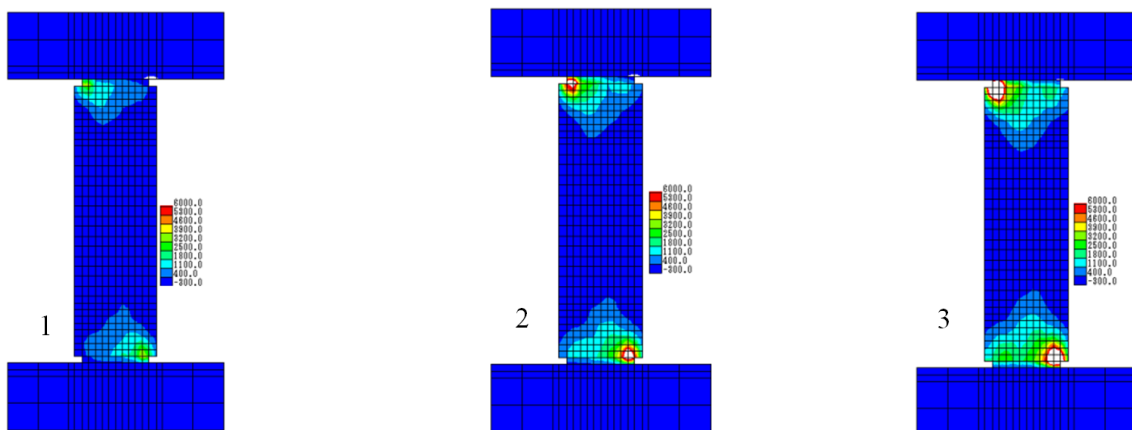
implies UHP-50 give similar strengthening effect with steel jacket case.



(a) Strain distribution of case ST-6 at point 1, 2 and 3



(b) Strain distribution of case UHP-30 at point 1, 2 and 3



(c) Strain distribution of case UHP-50 at point 1, 2 and 3

Figure 7.9 Strain distribution for case ST-6, UHP-30 and UHP-50

7.3 Application for repairing damaged RC column with UHP-SHCC

Umeda et al. carried out the experiment for the specimen having the same dimensions and structural details with CNTR-WEB, as shown in Figure 7.1(a), and they investigated the retrofitting effect of UHP-SHCC on the damaged RC column after loading (Umeda et al., 2010). Figure 7.10 show that the comparisons of load-displacement relationship between the experimental result and analytical result, which has already shown in Figure 7.6. Note that displacement was normalized by yield displacement of the experiment ($\delta_y = 6.7\text{mm}$) in this figure. In the experiment, load started to decrease after $8\delta_y$ because of buckling of longitudinal reinforcement. On the other hand, in the analysis, load kept until $-12\delta_y$ because buckling was not modeled.

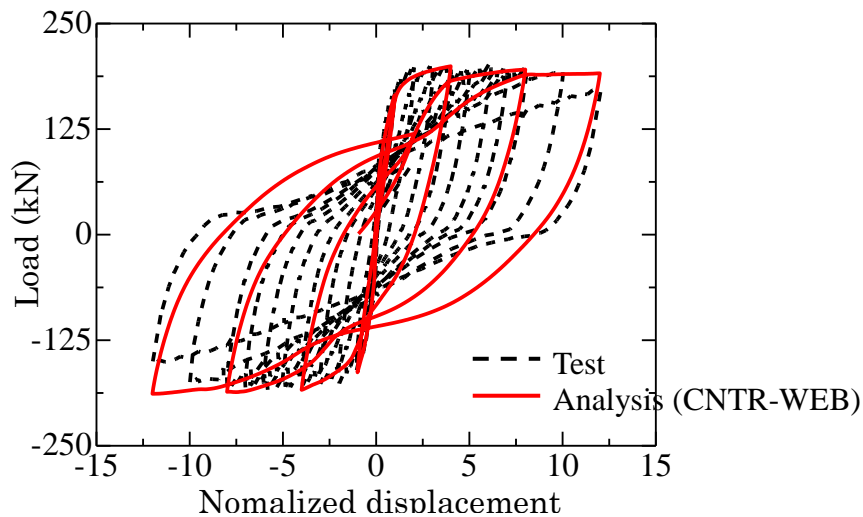


Figure 7.10 Comparisons of load-displacement relationship

In the experiment, repairing by UHP-SHCC was conducted after loading of $-12\delta_y$ and loading again after 28 days of curing. In the analysis, this process was modeled by following procedures:

- step 1 : Evaluation of damaged regions by maximum averaged strain and bond deteriorated region.
- step 2 : Decision of repairing part by considering step 1 and modeling of repairing.
- step 3 : Loading after repairing.

In step 1, after loading of $-12\delta_y$, damaged region was evaluated by damage evaluation method proposed by Kawai et al. (Kawai et. al., 2007), in which strains were averaged independent on element size and the maximum compressive averaged strain was the index of defining damage regions. Figure 7.11 shows the distributions of maximum

compressive averaged strain. In Figure 7.11, only the region with strain below -0.002 was colored and the damage pattern obtained from experiment was also shown. Comparing the strain distribution of analysis with damage pattern in the experiment, the regions with strain below -0.002 were coincided with the area where spall of concrete occurred. Moreover, bond stress deteriorated regions marked as yellow area shown in Figure 7.12, where slip of rebar exceeded 0.2mm, were also assumed as damaged region. In the figure, yellow colored region were almost corresponding with the area where concrete debonded.

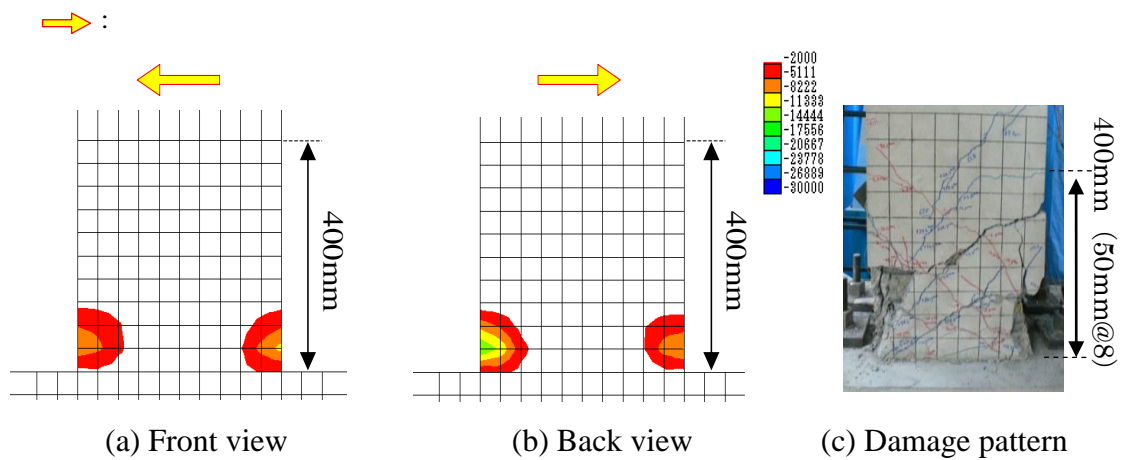


Figure 7.11 Evaluation of damaged region by the distributions of maximum compressive averaged strain (at $-12\delta_y$)

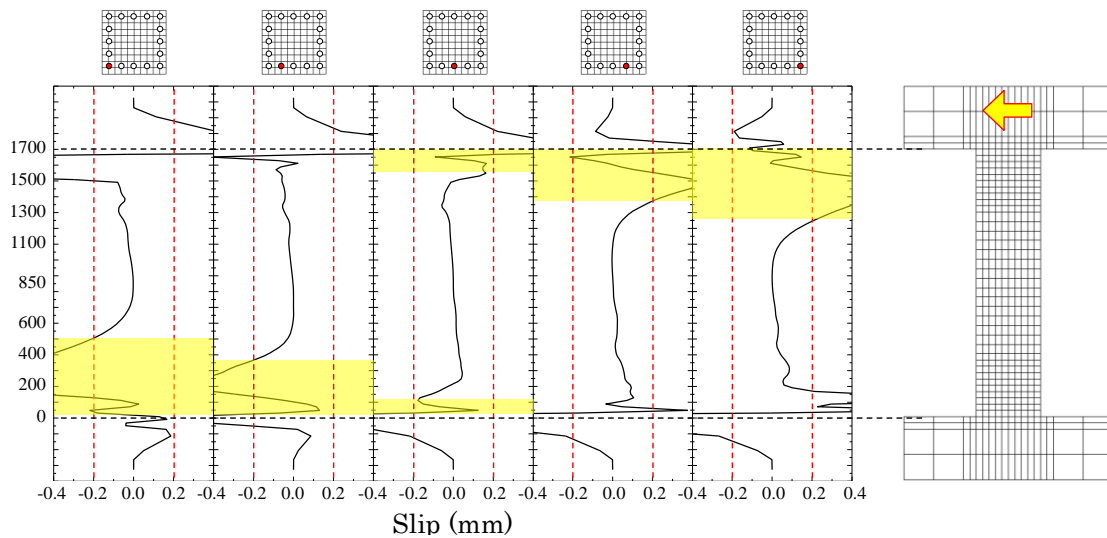


Figure 7.12 Evaluation of damaged region by bond stress deteriorated area (at $-12\delta_y$)

In step 2, following the discussion in step 1, repairing part was decided as the regions where circumference elements colored by gray in both ends of column, as shown in Figure 7.13. In the repairing part, damaged concrete elements replaced by new UHP-SHCC element, in which stress and strain were initialized and no consideration of stress and strain histories, as a repairing. Here, the zero-span stress-strain relationships of UHP-SHCC for 30 and 50mm thicknesses described in previous section (7.2.2.3 and Table 7.1) were assumed in the repaired material, because the repairing width was 40mm. It was also assumed that the bond properties between existed concrete and UHP-SHCC were perfect, except boundaries of UHP-SHCC and base concrete.

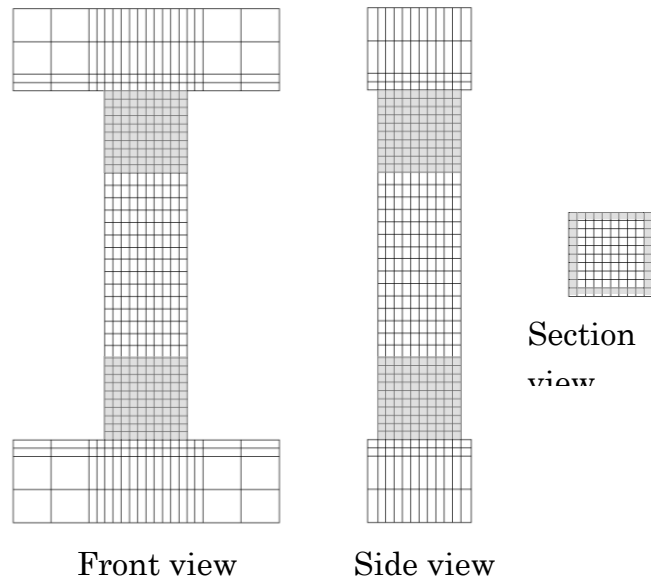


Figure 7.13 Assumption of repairing part

In step 3, monotonic loading was assumed after repairing, although cyclic loading was done in the experiment. Figure 7.14 shows load-displacement relationships of repaired column. In the Figure 7.14, experimental results are also drawn as envelope curve. As shown in figure, analytical results predict similar stiffness with experiment, however yielding load was higher than the experiment. Figure 7.15 shows the deformation after rebar yielding. As shown in Figure 7.15, deformation localized at not the end but the boundary with repairing part. This deformation did not occur in the experiment, due to the repaired areas in analysis are different from those in experiment, which is also the reason why the yielding load of the analysis was higher than that of the experiment.

As above discussion, it can be seen that the analytical method adopted in this study is

also applicable for repairing the damaged RC column under cyclic loading.

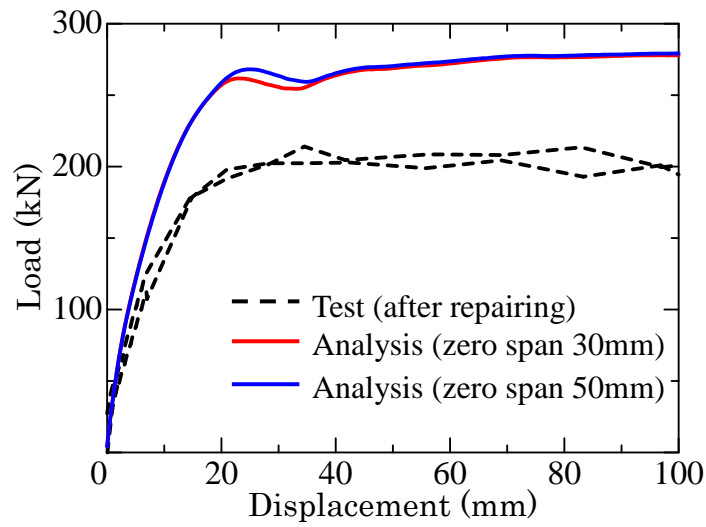


Figure 7.14 Load-displacement relationship of repaired column

○ :Yielding of rebar

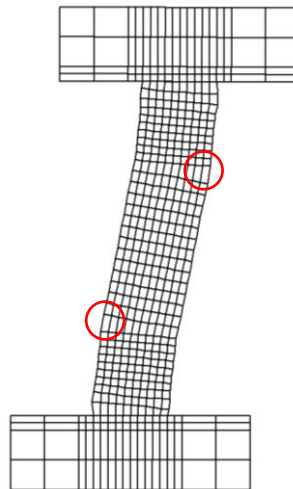


Figure 7.15 Deformation of repaired column after yielding

7.4. Conclusion

In this chapter, evaluation on RC column with and without web reinforcement strengthened by steel plate with thickness of 6mm and UHP-SHCC material with thickness of 30mm and 50mm is conducted.

(1) The numerical result of RC column without web reinforcements strengthened by steel plate with thickness of 6mm, and UHP-SHCC material with thickness of 30mm

and 50mm demonstrates that they were all in flexural failure behavior, without shear failure behavior. However, the strain distribution of RC column with thickness of 30mm spreads with the increasing of displacement, which is not so stable under cyclic load.

(2) The behavior of damaged RC column repaired with UHP-SHCC was evaluated by considering damage region evaluation. It was confirmed that the proposed method was also applicable for evaluation on the behavior of repaired RC structure.

CHAPTER 8

CONCLUSIONS

8.1 Summary and conclusions

This study presented about numerical evaluation of concrete members using UHP-SHCC material. The study was conducted by experiment and numerical evaluation. Three numerical models of UHP-SHCC in material level and structural level were proposed. The effectiveness of these proposed models were confirmed by comparing with experiment result. The following summary and conclusion were derived in this dissertation.

Chapter 2 presented the tri-linear curve model considering fracture energy in material level. The effective of this proposed model was verified by the analytical result which is identical well with the uniaxial tensile test without element dependency.

The zero-span tensile behavior was simulated using this tri-linear curve model with small mesh size, which was smaller than crack space. The zero-span tensile behavior from the investigation of numerical analysis was similar with zero-span tensile behavior from experiment by using stress-strain relationship for uniaxial tensile behavior. Moreover, in zero-span tensile behavior, multiple fine cracks propagated from the artificial crack part due to stress concentration and strains distribute through the depth of cross section. The zero-span tensile behavior may be occupied by the weaker behavior of materials.

In chapter 3, the experimental result of UHP-SHCC beam failed in diagonal shear was investigated. Four specimens of UHP-SHCC were tested which have different a/d and longitudinal reinforcement ratio. The crack propagation observed was that flexural multi-fine cracks occurred firstly. Then multiple fine cracks occurred in the middle of shear span. The number of multiple fine cracks increased with the increasing of load level, and multiple fine cracks in shear direction played dominant role gradually later. Thereafter, some multiple fine cracks localized until peak load, and then the specimen fractured in shear failure, in which the area near loading point was collapsed.

It was confirmed that the shear strength was not evaluated appropriately by the shear strength evaluation equations proposed in the past.

The shape of fracture surface of UHP-SHCC beam was investigated by using the laser displacement meter, and the roughness of fracture surface could be obtained. The smooth of fracture surface of UHP-SHCC beams was confirmed by investigation. The physical expression of crack surface with asperity height and angle were decided as 1.2mm and 15° for UHP-SHCC, which was different from those of normal concrete and high strength concrete.

Chapter 4 simulated the shear failure of UHP-SHCC members. In order to simulate the behavior, the shear stress transfer model for UHP-SHCC members were proposed, considering roughness of crack surface depending on asperity height and shape of crack surface (θ), crack width depending on crack distribution, and fiber contribution. In the model, expression of crack surface was recommended as 15° of angle and 1.2mm of asperity height based on measurement, due to smoothness of fracture surface of UHP-SHCC. The multiple fine crack distribution was recommended as multiple fine cracks in strain hardening phase and single localized crack in softening area. Fiber bridging stress was considered by the tensile stress at the crack surface. The shear failure behavior of UHP-SHCC beams was verified by using the proposed model.

Chapter 5 investigated the load carrying capacity and crack propagation mechanism of RC beam strengthened by UHP-SHCC with different thicknesses. For strengthened RC beam with UHP-SHCC, the load carrying capacity increased with increase of thickness of UHP-SHCC layer. Thereafter, the load dropped due to localization of multiple fine cracks in UHP-SHCC layer.

In the strengthened RC beam, the crack propagation of multiple fine cracks in UHP-SHCC layer depended on zero-span tensile behavior. When the thickness of UHP-SHCC was small, the damage in UHP-SHCC layer caused by stress concentration from localized crack in substrate concrete, and multiple fine cracks spread from top of UHP-SHCC layer adjacent to localized existing crack to bottom of UHP-SHCC layer. On the other hand, when the thickness of UHP-SHCC layer was enough large, the crack propagation of multiple fine cracks in UHP-SHCC layer depended on uniaxial tensile behavior due to bending effect from structural behavior, and the multiple fine cracks in UHP-SHCC layer spread from bottom of UHP-SHCC layer to top. Moreover, when the uniaxial tensile behavior in UHP-SHCC layer was dominant, the displacement at peak load increased as well as increase of load carrying capacity.

Chapter 6 presented numerical evaluation method on concrete member strengthened by UHP-SHCC layer in structural level. A new type of zero-span tensile model was proposed for UHP-SHCC used as a repair material for concrete substrate member with existing crack. This zero-span tensile model adopted a fictitious material of the same Young's modulus with concrete, and elastic stress-strain relationship without cracking was adopted to form artificial crack. The numerical behavior of RC member strengthened by UHP-SHCC using this zero-span tensile model, such as load-displacement relationship and crack propagation behavior, had a good agreement with experiment of RC beam strengthened by UHP-SHCC layer, due to the proposed model considering the average behavior of multiple-fine cracks adjacent to existing

crack in RC substrate beam.

Chapter 7 evaluated the strengthening effects of RC column strengthened by UHP-SHCC jackets under cyclic load by considering proposed models, such as shear stress transfer model and zero-span tensile behavior model. The numerical result of RC column without web reinforcements strengthened by UHP-SHCC material with thicknesses of 30mm and 50mm showed that failure modes of these strengthened specimens were flexural failures, which were similar with RC column with web reinforcements. It was confirmed that RC column strengthened with UHP-SHCC was effective under cyclic load, and numerical evaluation could be conducted reasonably by the proposed model. The behavior of damaged RC column repaired with UHP-SHCC was evaluated by considering damage region evaluation. It was also confirmed that the proposed method was applicable for evaluation on the behavior of repaired RC structure.

REFERENCE

Almusallam T.H., Salloum Y.A. (2001): ultimate strength prediction for RC beams externally strengthened by coposites materials, *Journal of Composites*, vol.32, pp.609-619

ASTM, C1609/C1609M-10: Standard test method for flexural performance of fiber-reinforced concrete (using beam with third-point loading)

Anthia, N. (1997): Fibre reinforced concrete: present and future, *Proc., Asia-pacific spec. conf. on fiber reinforced concrete*, CI-Premier Singapore, pp.1–10.

Bažant, Z.P. (2002): Concrete Fracture Models: Testing and practice, *Journal of Engineering Fracture Mechanics*, Vol. 69, No.1, pp.165-205

BOUSIAS S.N., FARDIS M.N., SPATHIS A. L., BISKINIS D. (2005): Seismic assessment and rehabilitation of existing buildings, *International closing workshop*, Istanbul

Barros, J. A. O., and Sena-Cruz, J. M. (2001): Strengthening a prestressed concrete slab by epoxy-bonded FRP composites and SFRC over-layer, *Proc., 7th Int. Conf. on Inspection, Appraisal, Repairs and Maintenance of Buildings and Structures*, Nottingham Trent, United Kingdom

Buyukozturk O., Gunes O., Karaca E.(2004): Progress on understanding debonding problems in reinforcedconcrete and steel members strengthened using FRP composites, Vol.18, No.1, pp.,9–19

Eugen B. (2008): Structural analysis of a composite bridge girder combining UHPFRC and reinforced concrete, *UHPC-2008: The Second International Symposium on Ultra High Performance Concrete*, Kassel, Germany

Fowler D.W. Fowler (1999). *Polymers in concrete: a vision for the 21st century*, *Cement & Concrete Composites*, Vol.21, No.5-6, pp. 449-452.

Horii H, Matsuoka S., Kabele P, Takeuchi S., Li V.C. and Kanda T. (1998): On the

Prediction Method for the Structural Performance of Repaired/Retrofitted Structures, Fracture Mechanics of Concrete Structures. Proceedings FRAMCOS-3, pp.1715-1726

Itoh, A., Kongkeo, P., Nakamura, H. and Tanabe, T. (2004): FEM analysis of RC members based on Lattice Equivalent Continuum Model, Journal of Materials, Concrete Structure and Pavements, JSCE, 767 (64), pp.115-129. (In Japanese)

J. A. O. Barros and J. M. S. Cruz: Strengthening a prestressed concrete slab by epoxy-bonded FRP composites and SFRC over-layer,
http://www.civil.uminho.pt/jsenacruz/Publications/CPI-002-2001_7IARMBS.pdf

JCI-DFRCC committee, (2003): DFRCC terminology and application concepts, Journal of advanced concrete technology, vol.1, No.3, pp.335-340

JSCE (2004): Recommendations for design and construction of ultra high performance fiber reinforced cement composites with multiple fine cracks (in Japanese)

Kamal A, Kunieda M, Ueda N, Nakamura H. (2007): Development of a zero-span tensile test for HPRCC used for structural repairing. Proceedings of FRAMCOS-6, CATANIA, Italy, pp.1509-1515

Kamal, A. (2008): Material development of UHP-SHCC for repair applications and its evaluation, dissertation submitted to Nagoya University, pp.175-181

Kamal, A., Kunieda, M., Ueda, N. and Nakamura, H. (2009): Evaluation of crack elongation performance of a repair material with strain hardening behavior, Journal of Cement & Concrete Composites, Vol. 30, No.10, pp.863-871

Kawai, M., Ueda, N., Nakamura, H. and Kunieda, M. (2007): Analytical study on mechanical behavior of repaired RC member after flexural damage", Proceedings of the Concrete Structure Scenarios, JSMS, Vol.7, pp.121-128.

Kongkeo, P., Nakamura, H., Kunieda, M. and Lee, S. (2005): Shear failure analysis of high strength concrete RC beams using LECOM, Proceedings of the Japan Concrete Institute, Vol.27, No.2, pp.715-720. (In Japanese)

Kunieda M., Hussein M., Ueda N. and Nakamura H. (2010): Enhancement of crack

distribution of UHP-SHCC under axial tension using steel reinforcement, *Journal of Advanced Concrete Technology*, Vol.8, No.1, pp. 49-57

Kunieda M., Hussein M., Ueda N. and Nakamura H. (2010): Fracture behavior of steel reinforced UHP-SHCC under axial tension, *Fracture Mechanics of Concrete Structures, Proceedings FRAMCOS-7*, pp.1557-1564.

Kunieda M., Ogura H., N. Ueda, H. Nakamura (2011): Tensile fracture process of strain hardening cementitious composites by means of three-dimensional meso-scale analysis outline of proposed model, *Cement & concrete composites*, vol.33,2011,956-965

Kunieda, M., Rokugo, K. (2006): Recent Progress of HPFRCC in Japan-Required Performance and Applications, *Journal of Advanced Concrete Technology*, Vol. 4, pp.19-33,

Kunieda M., Umeda Y., Ueda N., Nakamura H. (2012): Rapid jacketing technique by using UHP-SHCC for damaged RC column under seismic loading, *HPFRCC6*, pp.429-436

Lim Y.M. and Li V.C. (1997): Durable Repair of Aged Infrastructures Using Trapping Mechanism of Engineered Cementitious Composites, *Journal of Cement & Concrete Composites*, Vol.19, No. 4, pp.373-385

Li V.C. (1993). From micromechanics to structural engineering –the design of cementitious composites for civil engineering applications,” *Structural engineering/earthquake engineering, JSCE*, Vol.10, No.2,, pp. 37-48.

Li V.C. (1998). Engineered cementitious composites - tailored composites through micromechanical modeling, in *fiber reinforced concrete: present and the future* edited by N. Banthia, A. Bentur, A. and A. Mufti, Canadian society for civil engineering, Montreal, pp. 64-97.

Li, V.C. (1998): ECC for repair and retrofit in concrete structures. *Fracture Mechanics of Concrete Structures, Proceedings FRAMCOS-3*. Freiburg (Germany): Aedification Publishers, pp.1715-1726

Li. V.C. (2003): On engineered cementitious composites (ECC)-a review of the material

and its applications, *Journal of Advanced Concrete Technology*, Vol.1, No.3, pp.215-230

Li, V.C., Horii H, Kabele P, Kanda T. and Lim Y.M. (2000): Repair and Retrofit with engineered cementitious composites. *Journal of Engineering Fracture Mechanics*, Vol.65, No. 3, pp.317-334

Li V.C., Kanda T. (1998): Engineered cementitious composites for structural applications," *ASCE J. Materials in Civil Engineering*, Vol. 10, No. 2, pp. 66-69.

Li, V. C., Wang, Y., Backer, S. (1990) "Effect of Inclining Angle, Bundling, and Surface Treatment on Synthetic Fiber Pull-out from a Cement Matrix", *Composites*, Vol.21, No.2, pp.132-140.

Li V.C., Wu H.C. (1992). Conditions for pseudo strain hardening in fiber reinforced brittle matrix composites, *Applied Mechanics Review*, Vol.45, No.8, pp. 390-398.

Matsuda Y., Sugiyama T., N. Tougezaka, Y. Tsuji (2007): Interface resistance between polymer cement mortar and concrete substrate of repaired concrete, *Journal of the Society of Materials Science*, Vol.56, No.8, pp. 742-747.

Miller A., Rosenboom O., Rizkalla S. (2006): Fatigue behavior of in/mm²ct damaged prestressed concrete bridge girder repaired with CFRP sheets, 7th international conference on short and medium span bridges

Naaman A.E. (2003): Strain hardening and deflection hardening fiber reinforced cement composites," In A.E. Naaman and H.W. Reinhardt, Eds. High performance fiber reinforced cement composites (HPFRCC4), *Proceedings of the fourth international RILEM workshop*, pp. 95-113.

Nakamura, H. and Higai, T. (2001) Compressive fracture energy and fracture zone length of Concrete", In *Modeling of inelastic behavior of RC structures under seismic loads*, ASCE, pp.471-487.

Niwa, J. (1986): Evaluation of the equation for shear strength of reinforced concrete beams without web reinforcement, *Proceedings of JSCE*, No.372/V-5, pp. 167-176.

Ohama Y. (1991): Recent Progress in Concrete-Polymer Composites, Advanced Cement based Materials, Vol.5, pp. 31-40.

Paepegem W. V., Degrieck J. (2002): A new coupled approach of residual stiffness and strength for fatigue of fibre-reinforced composites, International Journal of Fatigue, vol.24, pp.747-762.

Sawabe, S., Ueda, N., Nakamura and H., Kunieda, M. (2006): Shear failure behavior analysis of RC beam with unbonded region and decreased bond strength stirrups, Doboku Gakkai Ronbunshuu E, Vol. 62, No. 2, pp.444-461

Suga, M., Nakamura, H., Higai, T. and Saito, S. (2001): Effect of bond properties on the mechanical behavior of RC beam, Proceedings of the Japan Concrete Institute, Vol.23, No.3, pp.295-300. (In Japanese)

Suryanto, B., Nagai, K. and Maekawa, K. (2010): Smeared-crack modeling of R/ECC membranes incorporating an explicit shear transfer model", Journal of Advanced Concrete Technology, Vol.8, No.3, pp.315-326.

Tanabe T. (2004): Nonlinear analysis method and programming of RC structure considering initial stress, technical report Press

Triantafillou T. C., Plevris N. (1992): Strengthening of RC beams with epoxy-bonded fibre-composite materials, Materials and Structures, Vol.25, No.14, pp.201-211

Umeda, Y., Kunieda, M., Nakamura, H., Tamakoshi, T. and Morii, N. (2010): Repairing Effect of RC Columns Repaired by UHP-SHCC, Proceedings of the Concrete Structure Scenarios, JSMS, Vol.10, pp.349-356.

United States Department of the Interior Bureau of Reclamation Technical Service Center (1996): Guide to concrete repair

University of Texas at Austin (2001): evaluation and performance monitoring of corrosion protection by fiber reinforced composite wrapping, Research Report No. 1774-1

Yamamoto T. (1992): FRP strengthening of RC columns for seismic retrofitting, International conference on earthquake engineering, Balkema, Rotterdam

Yonezawa, K., Hirata, T., Watanabe, S. and Okano, M. (2009): FEM analysis for nonlinear behavior of structural members using HPFRCC, Proceedings of the Japan Concrete Institute, Vol.31, No.2, pp.1255-1260. (In Japanese)